

CONTROL SURFACE HINGE MOMENT PREDICTION  
USING COMPUTATIONAL FLUID  
DYNAMICS

by

CHRISTOPHER DAVID SIMPSON

CHARLES R. O'NEILL, COMMITTEE CHAIR

GARY CHENG

SHAN ZHAO

A THESIS

Submitted in partial fulfillment of the requirements  
for the degree of Master of Science  
in the Department of Aerospace Engineering and Mechanics  
in the Graduate School of  
The University of Alabama

TUSCALOOSA, ALABAMA

2016

Copyright Christopher David Simpson 2016  
ALL RIGHTS RESERVED

## ABSTRACT

The following research determines the feasibility of predicting control surface hinge moments using various computational methods. A detailed analysis is conducted using a 2D GA(W)-1 airfoil with a 20% plain flap. Simple hinge moment prediction methods are tested, including empirical Datcom relations and XFOIL. Steady-state and time-accurate turbulent, viscous, Navier-Stokes solutions are computed using FUN3D. Hinge moment coefficients are computed. Mesh construction techniques are discussed. An adjoint-based mesh adaptation case is also evaluated. An NACA 0012 45-degree swept horizontal stabilizer with a 25% elevator is also evaluated using FUN3D. Results are compared with experimental wind-tunnel data obtained from references. Finally, the costs of various solution methods are estimated.

Results indicate that while a steady-state Navier-Stokes solution can accurately predict control surface hinge moments for small angles of attack and deflection angles, a time-accurate solution is necessary to accurately predict hinge moments in the presence of flow separation. The ability to capture the unsteady vortex shedding behavior present in moderate to large control surface deflections is found to be critical to hinge moment prediction accuracy. Adjoint-based mesh adaptation is shown to give hinge moment predictions similar to a globally-refined mesh for a steady-state 2D simulation.

## **DEDICATION**

This thesis is dedicated to all whom I love. Whether conscious of my love or not, you give purpose to my life in innumerable ways.

## LIST OF ABBREVIATIONS AND SYMBOLS

$A$	Point on a hinge axis about which moments are computed
$a$	Speed of sound
$b$	Wing span
$\hat{\mathbf{b}}$	Unit vector defining the hinge axis orientation
$c$	Airfoil section chord
$c_f$	Control surface reference chord
CFD	Computational Fluid Dynamics
$C_h$	Hinge moment coefficient $\frac{H}{q_\infty S_f c_f}$
$C_{h_0}$	Hinge moment coefficient at $\delta = 0$
$C_{h_{00}}$	Hinge moment coefficient at $\delta = 0$ and $\alpha = 0$
$C_{h_\alpha}$	Derivative of $C_h$ with respect to $\alpha$ , $\frac{\partial C_h}{\partial \alpha}$
$C_{h_\delta}$	Derivative of $C_h$ with respect to $\delta$ , $\frac{\partial C_h}{\partial \delta}$
$c_v$	Specific heat at constant volume
dS	Differential surface element
$e$	Specific internal energy
$\vec{\mathbf{F}}$	Total force vector acting on a surface
$\vec{\mathbf{g}}$	Body acceleration acting on a continuum

$H$	Hinge moment, positive TED
$k$	Thermal conductivity
$L$	Reference length
$M$	Mach number, $\frac{V}{a}$
$\vec{M}_A$	Total moment acting on a surface about point $A$
$\hat{n}$	Unit vector normal to a surface
$P$	Pressure
$q_\infty$	Freestream dynamic pressure, $\frac{1}{2}\rho_\infty V_\infty^2$
$\vec{r}$	Position vector which originates from a point $A$ on the hinge axis and terminates at a differential surface element $dS$
$R$	Specific gas constant
$Re$	Reynolds number, $\frac{VL}{\nu}$
$S$	Surface domain
$S$	Planform area
$S_f$	Control surface reference area
$T$	Temperature
$t$	Airfoil section thickness
$t$	Nondimensional time, $\frac{t^* a_{\text{ref}}^* L_{\text{ref}}}{L_{\text{ref}}^*}$
$t^*$	Dimensional time
$t_{\text{chr}}$	Nondimensional characteristic time, $\frac{L_{\text{ref}}}{M_{\text{ref}}}$

TED	Trailing-Edge Down
$\vec{v}$	Velocity vector
$V_\infty$	Freestream velocity
$V_{ne}$	Never-exceed speed, the maximum approved flight speed of an aircraft
$y^+$	Non-dimensional wall distance
$\alpha$	Angle of attack
$\delta$	Deflection angle, positive TED
$\Lambda$	Sweep angle
$\mu$	Dynamic viscosity
$\nu$	Kinematic viscosity
$\Omega$	Volume domain, bounded by a surface S
$\rho_\infty$	Freestream density
$\overline{\overline{\tau}}$	Viscous stress tensor

## ACKNOWLEDGMENTS

First and foremost, I would like to thank my family for supporting me in everything I have done in life. My mom and dad have never doubted my abilities, even when I doubted myself, and I know their love is unwavering. I also appreciate the delicious jams and jellies made by my mom. Lord knows I have eaten enough of them to last any normal human a lifetime.

I must specifically thank my brother, Jeremy. He is also my best friend, and I have relied on the late-night phone calls for advice, for fun, and just to vent and unwind after the longest of days.

I would also like to thank my friends, new and old, for their support and encouragement. Of my new friends, Josh was the first to start working in the lab other than me, and frankly it was getting lonely in the windowless dungeon we call the lab. I am grateful for Liz, David, Griffin, Alex, Abraham, Kyle, Reid, Brodie, and Chris who all helped to break the monotony of my daily life by providing much needed distractions. Life would be boring without unexpected interruptions, and I would much rather live a life of chaos than one of boredom. My old friends are too numerous to mention, but they are in my thoughts always, even though I am terrible at staying in touch.

I would also like to express sincere gratitude to Dr. O'Neill, who saw my potential and took me under his wing when I had little confidence in my own abilities. Without him, I would likely be right back where I was when I started the program. More than anything, he restored my confidence in myself. I could never hope for a better mentor.

I would also like to thank the other members of my thesis committee, Dr. Cheng and Dr. Zhao, for taking time out of their busy schedules to accommodate me. I appreciate all of the faculty, who have been incredibly helpful and supportive of me. I have never once

feared that I would be turned away by any professor at the University of Alabama. Thanks to the AEM department for taking a chance on me multiple times. They took a chance even accepting me to the program when others turned me away. They took a chance awarding me assistantships, without which I would have amassed significant debt. I know how fortunate I am to be where I am today, and I have never taken these opportunities for granted. I can only hope that I have earned what I have been given.

Thanks also to the wonderful people at NASA Langley Research Center with whom I had the pleasure of working during my Summer internship. That was certainly a turning point in my life, and I am grateful I had such an amazing opportunity. There is no better way to learn how to use software than spending an entire summer working with the developers. I cannot help but feel I received the better end of the deal. Beth Lee-Rausch was an amazing mentor; I can forgive the fact that she went to Auburn. I want to thank the entire FUN3D development team for providing me with support when they are not obligated to do so, especially Mike Park for teaching me what all the adaptation options do. The other students in my workspace taught me more than they can possibly know. Matt and Cameron in particular transformed my approach to programming.

Finally, I would like to thank the many accomplished individuals who have been a tremendous motivation for success. Though the most productive individuals are often denigrated in a generally uninspired society, their successes are cicerones to me.

# CONTENTS

ABSTRACT . . . . .	ii
DEDICATION . . . . .	iii
LIST OF ABBREVIATIONS AND SYMBOLS . . . . .	iv
ACKNOWLEDGMENTS . . . . .	vii
LIST OF TABLES . . . . .	xii
LIST OF FIGURES . . . . .	xiv
1 INTRODUCTION . . . . .	1
1.1 Problem Description . . . . .	1
1.2 Motivation . . . . .	5
1.2.1 Impact on Flying Qualities . . . . .	5
1.2.2 Impact on Aircraft Safety . . . . .	7
1.2.3 Difficulty of Predicting Hinge Moments . . . . .	9
1.2.4 Industry Needs . . . . .	13
1.3 Prior Works . . . . .	14
1.4 Objectives of Project . . . . .	17
1.5 Scope of Project . . . . .	18
2 OVERVIEW OF CFD METHODS . . . . .	20
2.1 2D Panel Method (XFOIL) . . . . .	20
2.1.1 Potential Flow Theory . . . . .	20

2.1.2	Integral Boundary Layer . . . . .	22
2.1.3	Geometry Construction . . . . .	22
2.1.4	XFOIL Control Surface Deflection . . . . .	23
2.2	Navier-Stokes CFD Solver (FUN3D) . . . . .	24
2.2.1	Governing Equations . . . . .	24
2.2.2	Finite Volume Method . . . . .	26
2.2.3	2D Mesh Generation . . . . .	26
2.2.4	3D Mesh Generation . . . . .	27
3	INVESTIGATION OF A GA(W)-1 AIRFOIL WITH 20% PLAIN FLAP . . . . .	28
3.1	Geometry Description . . . . .	28
3.2	Stability and Control Datcom . . . . .	30
3.3	XFOIL Results . . . . .	34
3.4	Viscous Navier-Stokes Results . . . . .	39
3.4.1	Mesh Generation . . . . .	39
3.4.2	Steady-State Navier-Stokes Solution . . . . .	44
3.4.3	Time-Accurate Navier-Stokes Solution . . . . .	51
3.5	Discussion of Results . . . . .	59
4	INVESTIGATION OF A 45-DEGREE SWEPT NACA 0012 HORIZONTAL STA- BILIZER WITH A 25% FULL-SPAN ELEVATOR . . . . .	65
4.1	Geometry Description . . . . .	65
4.2	Mesh Generation . . . . .	66
4.3	Steady-State Solution without Refined Wake . . . . .	72
4.4	Steady-State Solution with Manually-Refined Wake . . . . .	78
4.5	Discussion of Results . . . . .	80
5	Adjoint-Based Mesh Adaptation . . . . .	81

5.1	Adaptation Process . . . . .	81
5.2	Computating Hinge Moments on a GA(W)-1 Airfoil with Adjoint-Based Mesh Adaptation . . . . .	85
5.2.1	Adaptation Parameters . . . . .	86
5.2.2	Results . . . . .	88
6	COST BENEFIT ANALYSIS . . . . .	97
6.1	CFD Cost Estimates . . . . .	97
6.1.1	GA(W)-1 Reference Case . . . . .	98
6.1.2	NACA 0012 Swept Wing . . . . .	100
6.1.3	Full Aircraft Model . . . . .	100
6.2	Wind Tunnel Cost Estimates . . . . .	101
6.3	Discussion . . . . .	102
7	CONCLUSIONS AND FUTURE WORK . . . . .	104
7.1	Conclusions . . . . .	104
7.2	Future Work . . . . .	106
	REFERENCES . . . . .	108
A	SAMPLE DATCOM HINGE MOMENT CALCULATIONS FOR THE GA(W)-1 AIRFOIL . . . . .	113
B	CALCULATING HINGE MOMENTS FROM FUN3D OUTPUT . . . . .	116
C	XFOIL_HINGEMOMENT SOURCE CODE . . . . .	118
D	XFOIL.CH_SWEEPS SOURCE CODE . . . . .	125

## LIST OF TABLES

3.1	GA(W)-1 reference quantities . . . . .	29
3.2	GA(W)-1 trailing edge angle tangents . . . . .	30
3.3	GA(W)-1 Datcom hinge moment derivative predictions . . . . .	31
3.4	GA(W)-1 global grid convergence study hinge moments, $\alpha = 0^\circ$ , $\delta = 5^\circ$ . . . . .	43
3.5	GA(W)-1 time-averaged hinge moment coefficients for various nondimensional time steps; $\alpha = 0^\circ$ , $\delta = 40^\circ$ . . . . .	54
3.6	Comparison of select steady and unsteady FUN3D GA(W)-1 hinge moments	57
3.7	Comparison of GA(W)-1 hinge moment results, $\alpha = -8^\circ$ . . . . .	62
3.8	Comparison of GA(W)-1 hinge moment results, $\alpha = 0^\circ$ . . . . .	62
3.9	Comparison of GA(W)-1 hinge moment results, $\alpha = 8^\circ$ . . . . .	63
3.10	Comparison of GA(W)-1 hinge moment results, $\alpha = 12^\circ$ . . . . .	63
3.11	Comparison of GA(W)-1 hinge moment results, $\alpha = 16^\circ$ . . . . .	63
3.12	Comparison of GA(W)-1 hinge moment results, $\alpha = 20^\circ$ . . . . .	64
4.1	NACA 0012 swept wing reference quantities . . . . .	65
6.1	Comparison of cost estimates for various solution methods for predicting hinge moments on a GA(W)-1 airfoil . . . . .	99
6.2	Cost estimate for predicting hinge moments on an NACA 0012 swept wing .	100
6.3	Cost estimate for a CFD solution on a full aircraft configuration . . . . .	101
6.4	Wind tunnel assumptions and cost estimates . . . . .	102
6.5	Comparison of cost estimates of CFD solutions and wind-tunnel testing . . .	103

A.1	GA(W)-1 reference quantities. . . . .	113
A.2	GA(W)-1 trailing edge coordinates required for Datcom calculations . . . . .	114

## LIST OF FIGURES

1.1	Primary control system of a Harrier . . . . .	2
1.2	Diagram of an airfoil with a control surface. . . . .	2
1.3	Example of a Fowler flap . . . . .	3
1.4	Force and moment vector definitions. . . . .	4
1.5	Cooper-Harper scale of flying qualities. . . . .	6
1.6	Hinge moments of a supercritical-wing wind tunnel model, $M = 0.9$ . . . . .	10
1.7	An example of Frise aileron hinge moments . . . . .	12
1.8	Calculated and measured hinge moment coefficients for inboard control surface, $M_\infty = 0.6$ ; $\alpha = 1.63^\circ$ . . . . .	16
2.1	XFOIL airfoil and wake paneling scheme . . . . .	21
2.2	XFOIL local panel coordinate system . . . . .	21
2.3	GA(W)-1 airfoil with XFOIL flap deflection. . . . .	23
3.1	GA(W)-1 airfoil with 20% plain flap. . . . .	29
3.2	GA(W)-1 hinge moments computed using Datcom relations. . . . .	32
3.3	GA(W)-1 $C_{h_\delta}$ versus $\alpha$ for $\delta = 0$ (using second-order central difference) . . . . .	32
3.4	GA(W)-1 hinge moments computed using Datcom relations with reference $C_{h_0}$ . . . . .	34
3.5	GA(W)-1 XFOIL panels. . . . .	35
3.6	GA(W)-1 hinge moments computed by XFOIL. . . . .	36
3.7	GA(W)-1 lift coefficient computed by XFOIL. . . . .	36
3.8	GA(W)-1 drag polar computed by XFOIL. . . . .	37

3.9	GA(W)-1 drag polar computed by XFOIL (small deflections). . . . .	38
3.10	GA(W)-1 moment computed by XFOIL. . . . .	38
3.11	GA(W)-1 initial coordinates and connectivity and final fitted spline. . . . .	40
3.12	GA(W)-1 mesh used in FUN3D. . . . .	41
3.13	GA(W)-1 global mesh refinement study, $\alpha = 0^\circ$ , $\delta = 5^\circ$ . . . . .	43
3.14	$C_h$ versus $\delta$ , steady FUN3D. . . . .	45
3.15	GA(W)-1 steady-state flow field Mach number, $\alpha = 0^\circ$ . . . . .	46
3.16	GA(W)-1 steady-state flow field Mach number, $\delta = 0^\circ$ . . . . .	47
3.17	GA(W)-1 steady-state pressure coefficient, $\alpha = 0^\circ$ . . . . .	48
3.18	GA(W)-1 surface pressure coefficient, $\alpha = 0^\circ$ ; $\delta = 0^\circ$ . . . . .	50
3.19	GA(W)-1 surface pressure coefficient, $\alpha = 0^\circ$ ; $\delta = 20^\circ$ . . . . .	50
3.20	$C_l$ versus $\delta$ , steady FUN3D. . . . .	51
3.21	Drag polar, steady FUN3D. . . . .	52
3.22	$C_m$ versus $C_l$ , steady FUN3D. . . . .	52
3.23	GA(W)-1 time-averaged hinge moment coefficients versus nondimensional time step, $\alpha = 0^\circ$ , $\delta = 40^\circ$ . . . . .	55
3.24	Unsteady GA(W)-1 hinge moment coefficient history, $\alpha = 0^\circ$ ; $\delta = 40^\circ$ . . . . .	57
3.25	Periodic detail of unsteady GA(W)-1 hinge moment history, $\alpha = 0^\circ$ ; $\delta = 40^\circ$ . . . . .	58
3.26	Unsteady GA(W)-1 hinge moment coefficient history, $\alpha = 20^\circ$ ; $\delta = 20^\circ$ . . . . .	58
3.27	Periodic detail of unsteady GA(W)-1 hinge moment history, $\alpha = 20^\circ$ ; $\delta = 20^\circ$ . . . . .	59
3.28	GA(W)-1 unsteady flow field Mach number, $\alpha = 0^\circ$ , $\delta = 40^\circ$ . . . . .	60
3.29	GA(W)-1 unsteady flow field pressure coefficient contours, $\alpha = 0^\circ$ , $\delta = 40^\circ$ . . . . .	61
4.1	NACA 0012 wing reference geometry planform and airfoil section . . . . .	67
4.2	NACA 0012 wing reference geometry plain elevator detail . . . . .	68
4.3	NACA 0012 wing reference Reynolds number variation with Mach number . . . . .	68

4.4	NACA 0012 wing mesh . . . . .	70
4.5	NACA 0012 wing mesh with refined baffle wake . . . . .	71
4.6	NACA 0012 wing hinge moments, without refined wake . . . . .	73
4.7	NACA 0012 wing lift, without refined wake . . . . .	73
4.8	NACA 0012 wing drag, without refined wake . . . . .	74
4.9	Steady FUN3D pressure distribution on an NACA 0012 swept horizontal stabilizer, $\alpha \approx 0^\circ$ . . . . .	75
4.10	Steady FUN3D pressure distribution on an NACA 0012 swept horizontal stabilizer, $\alpha \approx -4^\circ$ . . . . .	76
4.11	Steady FUN3D pressure distribution on an NACA 0012 swept horizontal stabilizer, $\alpha \approx -8^\circ$ . . . . .	77
4.12	NACA 0012 hinge moment coefficient, refined wake mesh; $\delta = -7.8^\circ$ . . . . .	78
4.13	NACA 0012 lift coefficient, refined wake mesh; $\delta = -7.8^\circ$ . . . . .	79
4.14	NACA 0012 drag coefficient, refined wake mesh; $\delta = -7.8^\circ$ . . . . .	79
5.1	Mach 2.0 diamond airfoil mesh. . . . .	82
5.2	Mach 2.0 diamond airfoil mesh after 20 adaptations, colored by Mach number. . . . .	83
5.3	HIAD mesh after four adaptation iterations. . . . .	84
5.4	GA(W)-1 adjoint-adapted meshes, $\alpha = 0^\circ$ ; $\delta = 5^\circ$ . . . . .	89
5.5	Initial GA(W)-1 mesh detail for adjoint-based adaptation, $\alpha = 0^\circ$ ; $\delta = 5^\circ$ . . . . .	90
5.6	Final GA(W)-1 adjoint-adapted mesh detail, $\alpha = 0^\circ$ ; $\delta = 5^\circ$ . . . . .	91
5.7	GA(W)-1 adjoint-adapted flow field Mach number, $\alpha = 0^\circ$ ; $\delta = 5^\circ$ . . . . .	92
5.8	GA(W)-1 adjoint-adapted flow field pressure coefficient, $\alpha = 0^\circ$ ; $\delta = 5^\circ$ . . . . .	93
5.9	GA(W)-1 hinge moment coefficient versus number of grid nodes . . . . .	94
5.10	GA(W)-1 hinge moment coefficient versus spacing parameter . . . . .	95
5.11	GA(W)-1 lift coefficient versus number of grid nodes . . . . .	95
5.12	GA(W)-1 drag coefficient versus number of grid nodes . . . . .	96

# CHAPTER 1

## INTRODUCTION

This chapter introduces the problem, some background information, and the motivation behind the research presented in this thesis. Prior works are discussed in detail, including both successes and failures. The objectives and scope of this project are also detailed.

### 1.1 Problem Description

Control surfaces enable attitude control of an aircraft by means of changing the aerodynamic forces of a lifting surface. Control surfaces are featured on every modern fixed-wing aircraft. The ailerons, elevator, and rudder are the primary controls for a typical aircraft. A deflection of the primary controls affects the roll, pitch, and yaw rates of the aircraft. The pilot manipulates the primary controls by operating rudder pedals and either a stick or yoke, which are connected by mechanical or electromechanical means to the control surfaces. Figure 1.1 is an illustration of the primary control system in the Hawker Siddeley Harrier [1]. The control surfaces are connected to the primary control actuators via a system of linkages and cables. Not shown in the diagram is the hydraulic system for the aileron and elevator actuators. In addition to normal control surfaces, the Harrier also has jet reaction nozzles necessary for vertical takeoff and landing maneuverability.

A two-dimensional representation of a plain flap configuration is shown in Figure 1.2. The configuration shown is typical of an aileron on an aircraft wing. The control surface at the trailing edge of the wing can be deflected up or down by rotating about the hinge axis, shown normal to the page in the figure. By convention, a positive deflection is one in which the trailing edge of the control surface is moved downward.

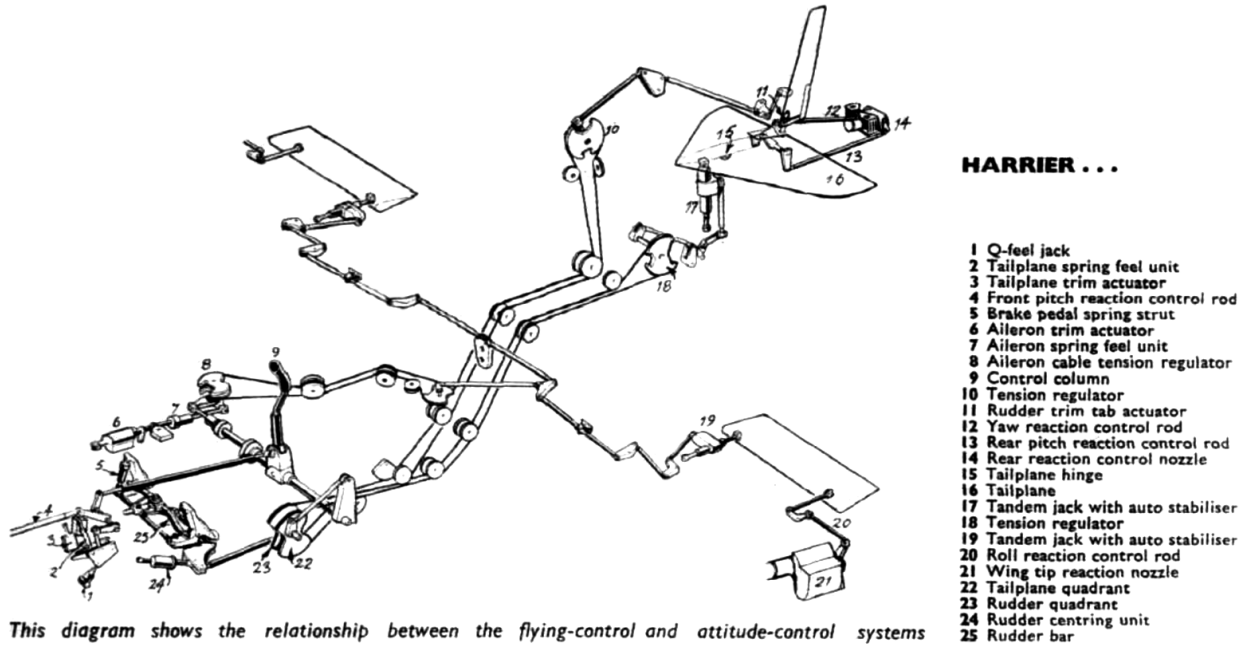


Figure 1.1: Primary control system of a Harrier [1]

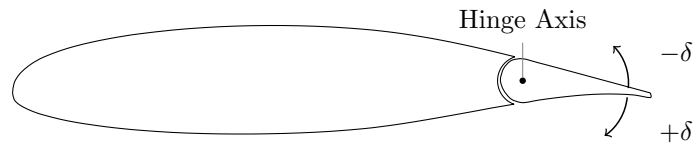


Figure 1.2: Diagram of an airfoil with a control surface.

Although the hinge axis is shown in Figure 1.2 is located within the bounds of the airfoil, it is entirely possible for a hinge axis to lie outside the wing geometry by way of an external hinge or a more complex mechanism. One example of a configuration commonly used in large aircraft that demonstrates the concept of a hinge outside of the airfoil is the Fowler flap. A Fowler flap extends via a system of linkages or an internal track mechanism, rotating the flap about a hinge axis below the wing, as shown in Figure 1.3.

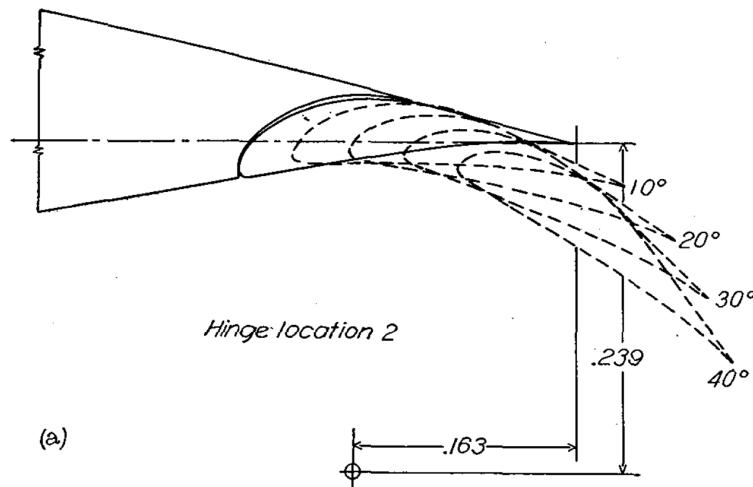


Figure 1.3: Example of a Fowler flap [2]

A control surface deflection alters both the mean camber line and the effective angle of attack of the airfoil section, and it causes a change in the pressure distribution on the geometry. The resulting change in lift induces a rotational moment on the aircraft. Attitude control of an aircraft is almost always achieved through the use of control surfaces due to the effectiveness, low cost, and relative simplicity of the system compared to other attitude control methods. However, the pressure difference between opposing faces of a control surface also produces a hinge moment on that surface.

To quantify the physical phenomena behind hinge moments, some analysis is required. Suppose a differential element exists on surface  $S$ , with a unit normal vector  $\hat{\mathbf{n}}$ , as shown in Figure 1.4. The element  $dS$  is located by a position vector  $\vec{\mathbf{r}}$  from a reference location  $A$  on the hinge axis. Ignoring body forces such as gravity, the total force on the surface is the

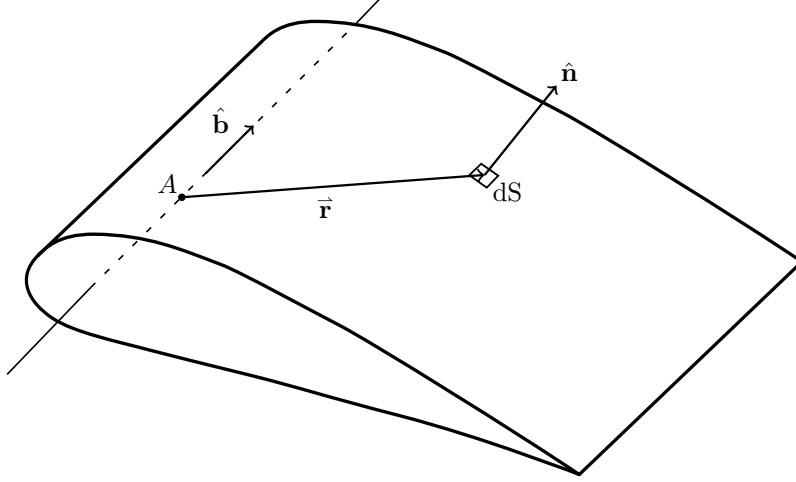


Figure 1.4: Force and moment vector definitions.

integration of the pressure and the viscous stresses over the surface,

$$\vec{\mathbf{F}} = - \iint_S P \hat{\mathbf{n}} dS + \iint_S \overline{\overline{\boldsymbol{\tau}}} \cdot \hat{\mathbf{n}} dS \quad (1.1)$$

where  $P$  is the pressure acting on the differential element and  $\overline{\overline{\boldsymbol{\tau}}}$  is the viscous stress tensor at that location. The moment on the body about point  $A$  is

$$\vec{\mathbf{M}}_A = - \iint_S \vec{\mathbf{r}} \times P \hat{\mathbf{n}} dS + \iint_S \vec{\mathbf{r}} \times (\overline{\overline{\boldsymbol{\tau}}} \cdot \hat{\mathbf{n}}) dS \quad (1.2)$$

This gives the total moment about a point on the hinge axis, but the moment of interest is the moment about the hinge axis. The hinge moment is therefore

$$H = \vec{\mathbf{M}}_A \cdot \hat{\mathbf{b}} \quad (1.3)$$

where  $\hat{\mathbf{b}}$  is a unit vector that defines the hinge axis.

Hinge moments are nondimensionalized using the hinge moment coefficient,

$$C_h = \frac{H}{q_\infty S_f c_f} \quad (1.4)$$

where  $S_f$  is the reference area of the control surface, typically taken to be planform area of the control surface aft of the hinge-line.  $c_f$  is the control surface reference chord, and is typically the mean distance from the hinge line to the trailing edge of the control surface measured normal to the hinge line.  $q_\infty$  is the freestream dynamic pressure. Dynamic pressure is defined as

$$q_\infty = \frac{1}{2} \rho_\infty V_\infty^2 \quad (1.5)$$

where  $\rho_\infty$  is the freestream density, and  $V_\infty$  is the freestream velocity.

## 1.2 Motivation

Control surfaces are an important and challenging aspect of aircraft design. Design flaws in control surfaces can not only negatively impact the handling qualities of the aircraft, but can also affect the pilot's ability to control the aircraft in certain conditions. In aircraft with a direct mechanical linkage between the primary controls and the control surfaces, the pilot experiences hinge moments directly in the form of stick forces. In larger aircraft with hydraulic actuators driving the control surfaces, the hinge moments dictate the size and number of actuators, and the total weight of the hydraulic system. In both cases, it is important that the hinge moments are predictable prior to building a prototype.

### 1.2.1 Impact on Flying Qualities

Aircraft performance is evaluated by test pilots using the Cooper-Harper rating scale [4]. Using this rating scale, various flying qualities can be quantified. Hinge moments play a large role in the flying qualities of an aircraft.

Control surfaces which are insufficiently sized will produce lower control authority, negatively impacting aircraft performance and maneuvering ability. Increasing the area of a control surface increases its effectiveness but increases the hinge moment, resulting in an increase in physical workload for the pilot. Aircraft handling qualities are impacted not only by a pilot's physical exertion, but also the mental workload associated with maintaining

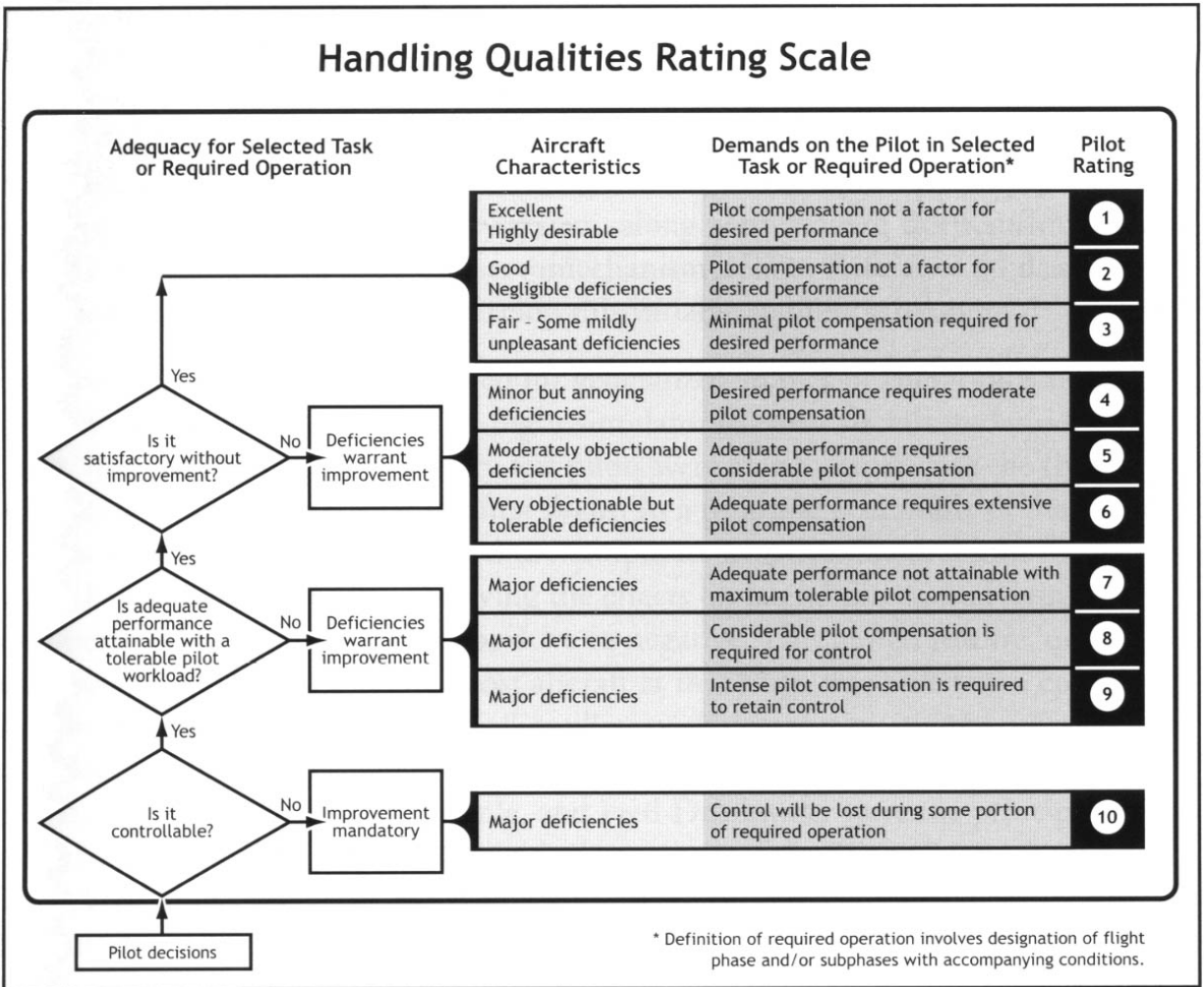


Figure 1.5: Cooper-Harper scale of flying qualities [3].

control of the aircraft. A study of seven general aviation aircraft conducted by Barber, et al. [5] found that some aircraft with light primary controls were more difficult to navigate along a specified ground track, and were therefore not always more favorable than aircraft with heavier controls.

### **1.2.2 Impact on Aircraft Safety**

Control surface performance can have a serious impact on the safety of an aircraft design. One aircraft in Barber, et al. [5] was capable of taking off at speeds below the minimum safe control speed, indicating that the control surfaces were undersized for that aircraft. Another aircraft in the same study experienced stick force reversal during low-g maneuvers in a landing configuration. These issues are difficult to identify in early stages of aircraft design.

#### **Messerschmitt Me-262**

The Messerschmitt 262 demonstrates the importance of a properly designed control surface. The Me 262 was a twin turbojet fighter aircraft developed by Germany during World War II. A Frise aileron was used on the Me 262 in an attempt to reduce hinge moments during high speed flight. The hinge axis is located at 29 to 30% of the aileron chord aft of the leading edge and slightly below center. When the aileron is deflected, the leading edge extends beyond the wing surface.

A first-hand account of test flights in the Me 262 is presented by test pilot Wolf Czaia [6]. Test flights of a restored Me 262 revealed multiple issues with the control surface design. In one test flight, when Czaia rolled the aircraft to the right at high speeds, the control force suddenly reversed, forcing the stick to the right and quickly rolling the aircraft through 60 degrees of bank before he was able to recover. This sudden control force reversal was caused by an aileron which was misaligned by 10 mm. In fact, the original factory specification required the aileron to be aligned within 1.5 mm of specification to avoid this problem. The misalignment caused flow reversal on the upper surface of the aileron, which in turn caused a reversal of hinge moment.

## **Minkler Venture M20**

At the Reno Air Races on September 13, 2002, a Minkler Venture M20 experienced a structural failure of the horizontal stabilizer, resulting in a fatal accident [7]. During development of the aircraft, one test flight was flown without an artificial force feel limiting device, and the test pilot experienced a stick force of less than 1-pound per g. The test pilot determined that the exceptionally light stick force caused severe pilot-induced oscillations. As a result, the designers added a spring assembly to the elevator circuit to give a force feedback of 10-pounds per g to the pilot. The aircraft that crashed at the Reno Air Races was assembled using a weaker spring than was intended. A combination of flutter on the horizontal stabilizer as a result of exceeding  $V_{ne}$  and pilot-induced oscillations due to insufficient stick force resulted in damage to the horizontal stabilizer, and the pilot lost control of the aircraft.

## **Piper PA-32R**

In another incident, a Piper PA-32R crashed due to a runaway trim condition [8]. The elevator servo was determined to work correctly only in one direction. When the pilot disengaged the autopilot, a control force in excess 50 pounds was required to maintain attitude. Due to the excessive force required, the pilot was unable to disengage the malfunctioning electric pitch trim.

## **ATR-72**

In 1994, 68 people were fatally injured when an ATR-72 crashed [9]. While in a holding pattern over Chicago, ridge ice formed on the upper surface of the wing beyond the deice boots. The result was a sudden reversal of aileron hinge moment, causing the aircraft to abruptly roll to one side. When the pilot attempted to recover, the aircraft again rolled to the right, resulting in an inverted attitude and subsequent rapid descent. This issue was known to exist for this type of aircraft [10], but the manufacturer failed to properly research the issue. Had a reliable method of predicting hinge moments under adverse conditions

been available, perhaps a solution could have been devised to correct the issue prior to the accident.

### 1.2.3 Difficulty of Predicting Hinge Moments

The preceding examples attest to the difficulty of predicting hinge moments. As a control surface is deflected, an adverse pressure gradient is induced on the low-pressure surface. The tendency for a flow to separate is increased in the presence of an adverse pressure gradient [11]. The separated flow that occurs on most control surface geometries is inherently unsteady. Matters are further complicated by the nonlinearity of hinge moments, especially in the transonic range.

In a 1974 study of a supercritical-wing model by Re [12], a nonlinear variation in aileron hinge moments caused a sign change in  $C_{h_\alpha}$  at a Mach number of 0.9. A sign change in  $C_{h_\alpha}$  means that as angle of attack is increased, the control force is lightened, which could cause a pilot to over-control the aircraft. The same study also shows a sign change in  $C_{h_\delta}$  at the same mach number for some angles of attack, as shown in Figure 1.6. This is perhaps a more significant issue, as the pilot would experience a control force which decreases with greater deflection. Such nonlinear control behavior increases the demand on the pilot and is a leading cause of pilot-induced oscillations [13].

The Grumman XF10F Jaguar had a free-floating horizontal stabilizer that was controlled aerodynamically using a pilot-controlled canard forward of the stabilizer. The pilot controlled the angle of the canard, which produced a pitching moment on the stabilizer and caused it to rotate. There was a lag between the pilot input command and the aircraft pitch response, which frequently caused pilot-induced oscillations [14].

As aircraft became larger and faster, hinge moments became a topic of some interest in the research community. Frise ailerons – used fairly commonly during and shortly after World War II – are ailerons which have a significantly offset hinge axis, causing a portion of the aileron leading edge to be exposed to the flow when the aileron is deflected. Frise ailerons were originally designed to balance the aileron hinge moments to enable the pilot to deflect

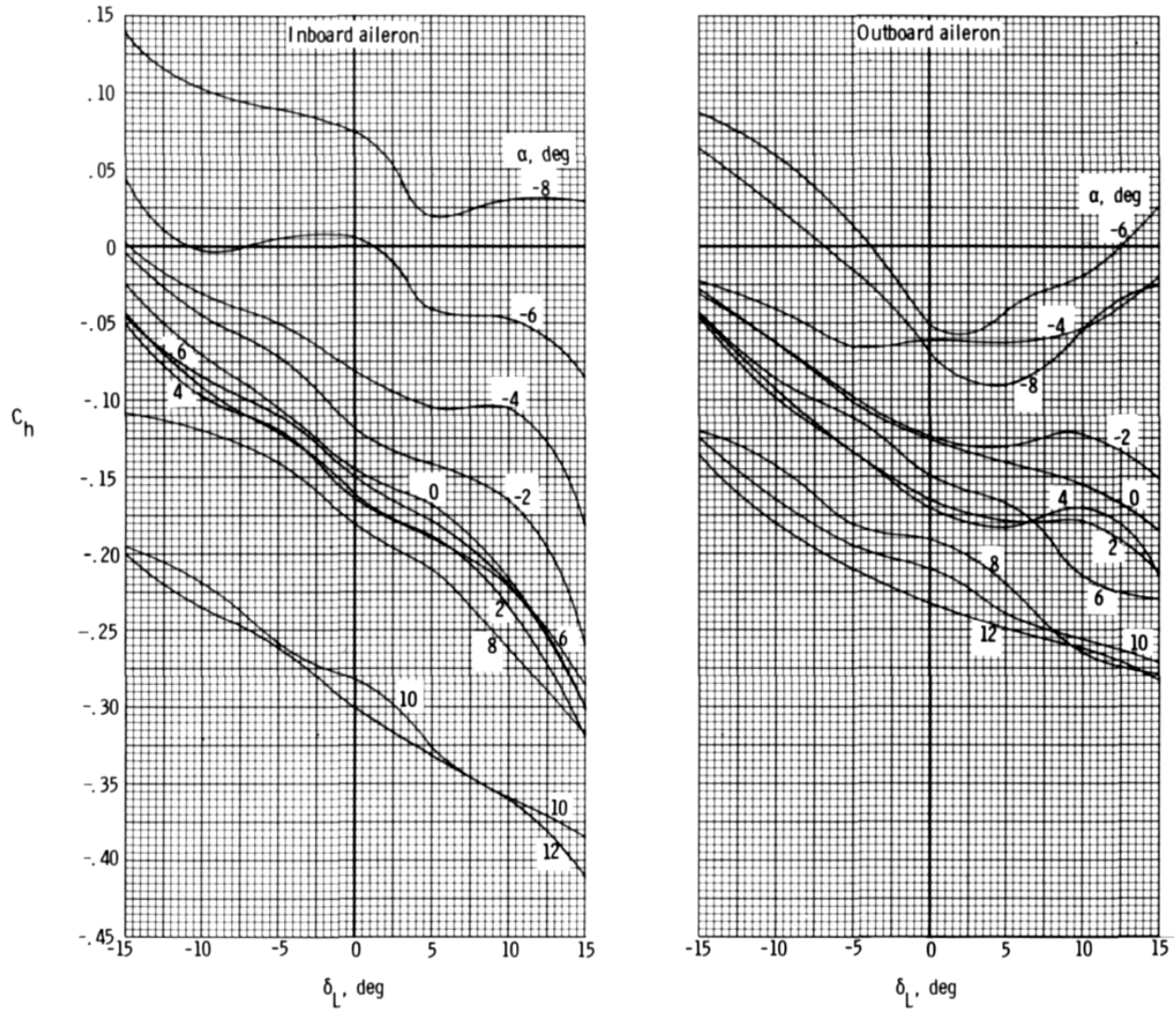


Figure 1.6: Hinge moments of a supercritical-wing wind tunnel model,  $M = 0.9$  [12]

the controls easily across an aircraft's entire flight envelope. Although not commonly used in modern aircraft, they are used in some vintage aircraft to counteract adverse aileron yaw by increasing the profile drag on the upward-deflected aileron, an effect which is achieved by placing the hinge axis close to the bottom edge of the airfoil. However, Frise ailerons have some significant drawbacks.

Figure 1.7 shows the hinge moment behavior typical of a Frise aileron. Control surfaces with conventional hinge axis location typically produce hinge moments that oppose the deflection angle and increase in magnitude as deflection angle increases and also as angle of attack increases. This behavior manifests as a negative slope of the  $C_h$  vs.  $\delta$  curve across the entire range of deflection angles. In contrast, Frise ailerons often have a tendency to produce moments in the direction of the deflection for certain deflection angles, seen as a dip in the  $C_h$  vs.  $\delta$  curve. Note that the zero hinge moment deflection angle is significantly larger than a more traditional configuration, as much as 11 degrees from neutral position for slow speeds and large angle of attack. This type of control surface can only be used in an aileron configuration because the hinge moments must be balanced, else the stick force would be reversed for the pilot. Pilots operating aircraft with Frise ailerons would experience a control force that lightens over certain deflection angles, an undesirable trait for an aircraft. Letko and Kemp [15] observed oscillations of certain Frise ailerons at certain deflection angles, and a violent vibration at small deflection angles for a higher angles of attack.

As the wing angle of attack increases, an increasingly negative hinge moment is induced on the control surface. A negative hinge moment is a trailing-edge up moment. This behavior is often called a floating tendency, as the control surface tends to "float" [16]. The floating tendency is characterized by a negative  $C_{h\alpha}$ .

As a control surface is deflected away from its neutral position, the hinge moments act to restore the control surface to that neutral position. This restoring tendency is characterized by a negative  $C_{h\delta}$ . The natural floating position of a control surface is the deflection angle at which  $C_h = 0$ . The natural position is specific to the geometry, and it changes with angle

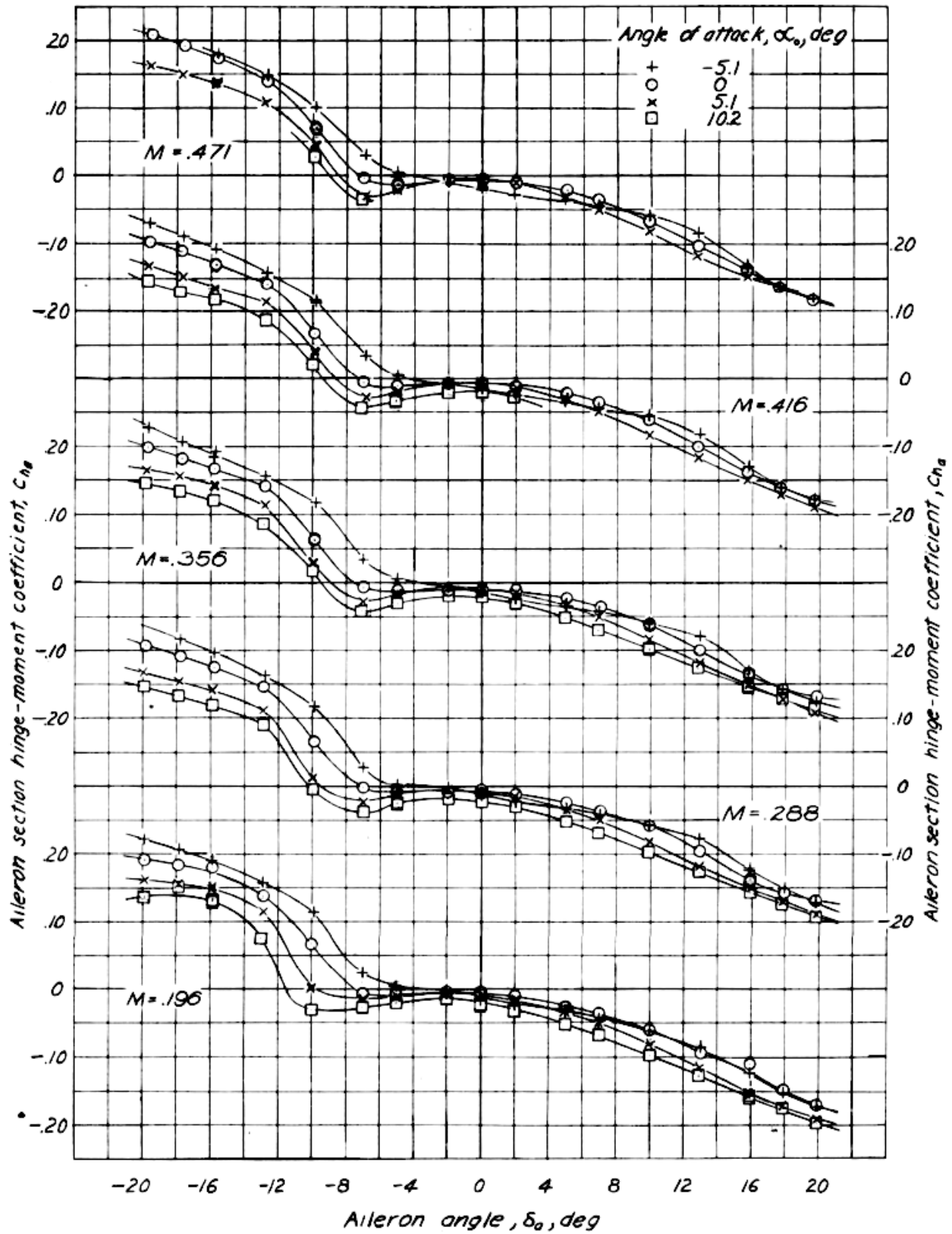


Figure 1.7: An example of Frise aileron hinge moments [15].

of attack and Mach number.

If  $C_{h_\delta}$  is positive at any deflection angle, the pilot will experience a lightening stick force as the control surface is deflected further. This is undesired and unexpected behavior. If the hinge moment coefficient changes signs when  $C_{h_\delta}$  is positive, a control force reversal occurs. In this scenario, the hinge moment acts to move the controls further away from the neutral position.

#### 1.2.4 Industry Needs

Detecting potential issues with sizing in early stages of development is critical. Aircraft design changes are significantly more expensive in late stages of the design process. Wind tunnel testing is expensive, due in part to the long cycle time associated with it [17]. Tests conducted in wind tunnels are typically conducted at a lower Reynolds number than flight tests, so experimental hinge moment measurements frequently differ from flight test measurements. This problem is relevant for the entire aviation industry because all fixed-wing aircraft make use of aerodynamic control surfaces for attitude control.

A less expensive method of hinge moment prediction is desired. CFD is relatively inexpensive compared to more traditional methods, both in terms of operating costs and hardware costs [18, 19]. CFD also enables the exploration the effects of unconventional geometry. Although CFD will never completely replace wind tunnel testing, if it can be used to reliably predict hinge moments, then it is an inexpensive means to perfect control surface designs.

As CFD becomes less expensive, it is used more frequently as a supplement – and even as an alternative – to wind-tunnel testing. Boeing’s use of CFD increased from 100-200 simulations in 1973 to over 20,000 in 2002 [19].

A study conducted by Airbus in 2004 found that hinge moments could be computed for a spoiler for small angles of attack and a relatively modest deflection angle [20]. This is an example that demonstrates the industry desires for a numerical approach to solving these problems. More recently, Makarov and Pavlenko conducted a study using CFD exclusively

to predict hinge moments for several control surface nose shapes [21]. Similar studies were conducted in the past using wind tunnels.

Little progress has been made to predict hinge moments in the last decade. This is partly because there is a common perception that other topics are more important to the industry, and the natural progression of research is to examine the most complex problems in the greatest detail. However, hinge moment prediction is an under-served area of research, so it remains a challenge for the industry. There is a need for a relatively inexpensive and reliable method to predict control surface hinge moments.

An industry professional, J. Hardin, indicated in personal correspondence that prediction of accurate control surface hinge moments is a major challenge. He explained that “early design iterations are based on handbook empirical methods and low order computational methods that cannot account for complex interactions between airframe components.” He also cited a case in which a wind-tunnel test conducted at flight Reynolds number differed from the flight test data. Hinge moments that differ significantly from expectations can lead to costly design changes. CFD may offer an affordable opportunity to account for these differences prior to building a prototype.

### 1.3 Prior Works

The idea of computing hinge moments is not a recent development. A 1945 study by Crane [22] used existing experimental data to develop an empirical model for hinge moments on an elevator. Crane used experimental results from various configurations of airfoils to correlate the hinge moments with control surface chord, hinge location, balance chord, nose gap, nose shape, airfoil section, and aspect ratio of the horizontal stabilizer.

Through a series of simple data interpolations and the application of lifting line theory, Crane was able to predict  $C_{h\delta}$  with a mean percent error of 12.38% and  $\left(\frac{\partial C_h}{\partial C_m}\right)_\alpha$  with a mean percent error of 7.16%. The results of this study show that it is possible to predict some hinge moment derivatives, but the moments are not actually computed in the study. While

knowing the hinge moment rates of change is important, the magnitude of the moments is critical to understanding the handling qualities of an aircraft. Furthermore, developing the analytical model for a specific configuration requires knowledge about similar designs, and a new model must be developed for new configurations, making this method impractical for use engineering applications.

Nielsen et al. also proposed an empirical method for predicting hinge moments in 1952 [23]. They concluded that while the empirical procedures can work in very specific applications, they can not predict hinge moments with certainty. This was also concluded by Nielsen 30 years later with a modified version of the same empirical procedures [24].

Swanson and Gillis attempted to compute aileron hinge moments by applying Prandtl lifting-line theory to a three-dimensional wing [25]. They determined that several factors oppose this approach. Viscous effects are significant, and simple corrections are insufficient to consistently predict hinge moment behavior in low-speed flows. Even using known 2D section data, lifting-line theory was found to be inadequate for accurately determining hinge moments.

The *USAF Stability and Control Datcom* [26] contains empirical relations to estimate  $C_{h_\alpha}$  and  $C_{h_\delta}$ . The relations provided are derived from fitting curves to a large selection of experimental data. Using these empirical relations for geometry configurations fitting the criteria described by the Datcom, hinge moment derivatives can be estimated quickly using only information about the airfoil geometry and flow conditions. This type of analysis is useful for conceptual design due to its ease of use, speed, and low cost. The advantage of this model over the models developed by Crane is that the relations are general in nature, and they can be used for a wide range of geometry. The Datcom methods are used in this study as part of a comparison between various prediction methods.

A study by Perry in 1978 [27] used an inviscid solver combined with a boundary layer program to iteratively solve for hinge moments on a high aspect ratio supercritical wing with inboard and mid-span ailerons. Perry was able to predict the hinge moment on the

inboard control surface with reasonable accuracy for small deflection angles and at a low angle of attack. However, the solution obtained by Perry does not capture some of the slight nonlinearity that exists in the experimental data, as shown in Figure 1.8. Additionally, the use of an inviscid flow solver is only valid in high Reynolds number flows where the viscous forces are relatively small compared to pressure forces. An integrated boundary layer method can account for viscous forces, but only in the absence of flow separation. Control surface deflections typically result in an airfoil surface which, even if made continuous by filling the gap between the control surface and wing, would not have  $C^2$  continuity. The result is a large adverse pressure gradient, which tends to lead to flow separation.

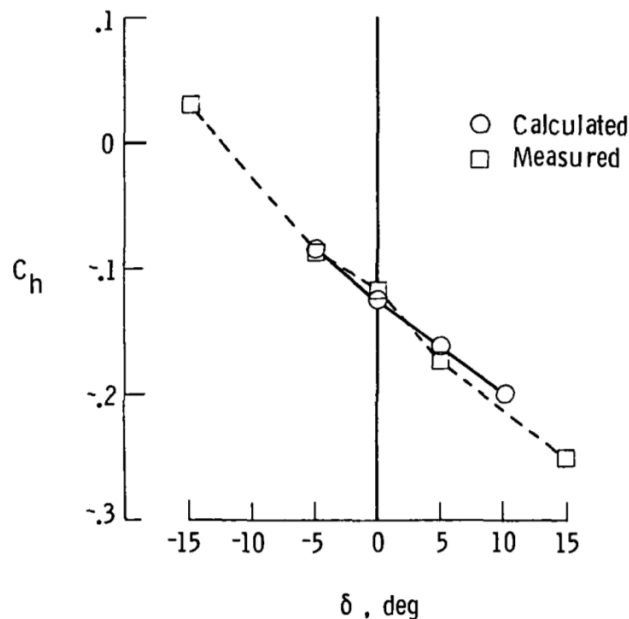


Figure 1.8: Calculated and measured hinge moment coefficients for inboard control surface,  $M_\infty = 0.6$ ;  $\alpha = 1.63^\circ$  [27]

One study conducted in 2000 by Grismer, et al. [28] investigated the use of CFD to predict control surface hinge moments for a wing from a salvaged Firebee drone. The study used the Euler/Navier-Stokes CFD solver Cobalt<sub>60</sub> with various solver configurations to predict hinge moments for only a couple deflection angles. Grismer obtained a steady-state solution, and several cases run at a time-accurate solution showed no appreciable difference. Grismer states that the steady-state solution converged in about 2500 iterations. One key conclusion

from Grismer is that predicting flow separation is critical to accurately predicting hinge moments. Due to the nature of flow separation, particularly on a complex geometry, this implies that an unsteady solver is necessary.

Three grids were evaluated by Grismer, with varying levels of resolution in the vicinity of the control surface, varying from 2.4 million cells to 3.4 million cells. Interestingly, the numerical results obtained by Grismer show poorer agreement as the grid resolution increases. The results from the coarsest grid are presented in the study, with a remark on the “relatively good agreement” with the experimental data. This is an unfair comparison between CFD and experimental data, because it neglects the additional flow physics inherently captured by a finer grid.

Although many of the conclusions made by Grismer may be correct, the shortcomings in the study are sufficient to investigate the problem in deeper detail. In particular, the spatial and temporal resolutions are in question.

## **1.4 Objectives of Project**

This thesis aims to address two main areas of investigation. First, what is the current state-of-the-art technology, and what is required to predict hinge moments accurately using CFD? Secondly, are the methods required for accurate results practical enough to use in real-world applications, or is it more cost-beneficial to use low-fidelity models and rely on wind-tunnel testing to validate control surface designs?

Quantifying the required degree of solution accuracy is somewhat subjective due to a vast spectrum of mission requirements. Different phases of the design process require different levels of fidelity from a solution. In the conceptual design phase, the objective is to quickly narrow down a wide range of design concepts. Increasingly accurate models are required as the design advances in the process, moving through preliminary design and then into detail design. Some projects that are time-critical or low-budget may choose to sacrifice solution fidelity to fit the needs of the organization. On the other hand, large-scale projects

may require the most accurate solution available to ensure that the final design meets or exceeds the specified requirements. For the purposes of this study, the accuracy of a solution method is determined by comparing the solutions with available experimental results. Each numerical method evaluated in this study is used to compute the following quantities:

1. Hinge moment coefficient
2. Deflection-induced lift, drag, and moment on the overall geometry
3. Pressure distributions

### 1.5 Scope of Project

In order to completely assess the current state of the art, and in order to gain a sense of cost-benefit for various levels of fidelity, several computational methods must be evaluated. This investigation examines the computation of hinge moments using the following methods:

1. Datcom +  $C_{h_0}$
2. Potential Flow Theory + Integral Boundary Layer
3. Steady, Turbulent Navier-Stokes
4. Time-accurate, Turbulent Navier-Stokes

The *USAF Stability and Control Datcom* [26] provides a set of empirical relations that can be used to predict  $C_{h_\alpha}$  and  $C_{h_\delta}$  based on the shape of the airfoil trailing edge. Combining this with an experimental value of  $C_{h_0}$  provides a means of predicting hinge moments. Additionally, this study examines the use of the Datcom to predict only  $C_{h_\delta}$ , and finding hinge moments for a range of  $\delta$  based on a sweep of known  $C_h$  values at various angles of attacks.

Potential flow theory is a computationally simple method of solving fluid problems. The potential flow solver used in this study is XFOIL. The integral boundary layer features of XFOIL are used in this study to account for viscous effects.

The Navier-Stokes CFD solver used in this study is NASA Langley Research Center's FUN3D. Both steady-state and time-accurate solutions are investigated as part of this study. The results presented in this study make use of the compressible, viscous governing equations. All FUN3D solutions presented use the Spalart-Allmaras turbulence model.

## CHAPTER 2

### OVERVIEW OF CFD METHODS

#### 2.1 2D Panel Method (XFOIL)

Panel method solvers are useful tools that can give fast, computationally inexpensive solutions to fluid problems. While the quality of the results may be insufficient for a detailed design, they often prove useful during conceptual design due to the speed of the solution. The fast solution time and ease of use warrants an investigation into the feasibility of using a panel method solver to predict hinge moments. This project makes use of XFOIL, a panel method solver written by Drela [29].

##### 2.1.1 Potential Flow Theory

The potential flow theory used by XFOIL is detailed by Drela [29]. An airfoil modeled in XFOIL is discretized into panels, spanning  $N$  nodes on the airfoil surface and  $N_w$  nodes in the wake. Each airfoil panel is modeled with a vortex of strength  $\gamma$  and a source of strength  $\sigma$ . Each wake panel has only a source of strength  $\sigma$ . The source terms are required to couple the potential flow solution with the viscous boundary layer calculations discussed in §2.1.2. Drela gives the stream function for the discrete airfoil-wake system [29]:

$$\begin{aligned}
 \Psi(x, y) = & u_\infty y - v_\infty x + \frac{1}{4\pi} \sum_{j=1}^{N+N_w-1} \Psi_j^\sigma(x, y) 2\sigma_j \\
 & + \frac{1}{4\pi} \sum_{j=1}^{N-1} \Psi_j^{\gamma+}(x, y) (\gamma_{j+1} + \gamma_j) + \Psi_j^{\gamma-}(x, y) (\gamma_{j+1} - \gamma_j) \\
 & + \frac{1}{4\pi} (\Psi_N^\sigma(x, y) |\hat{s} \times \hat{t}| + \Psi_N^{\gamma+}(x, y) |\hat{s} \times \hat{t}|) (\gamma_1 - \gamma_N)
 \end{aligned} \tag{2.1}$$

The last term in the Equation 2.1 models the panel that spans the finite trailing edge of an airfoil, where  $\hat{s}$  is a unit vector that bisects the trailing edge angle, and  $\hat{t}$  is a unit vector along the panel.

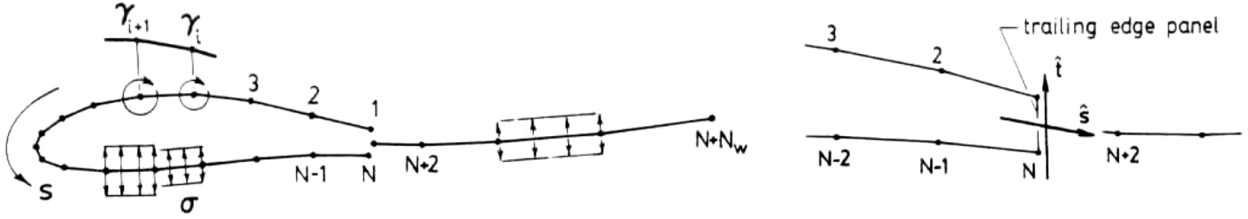


Figure 2.1: XFOIL airfoil and wake paneling scheme [29]

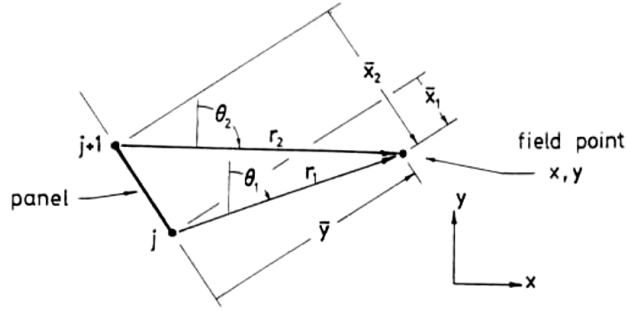


Figure 2.2: XFOIL local panel coordinate system [29]

Drela uses the local panel coordinate system shown in Figure 2.2 to define the stream function components.

$$\Psi_j^{\gamma^+}(x, y) = \bar{x}_1 \ln r_1 - \bar{x}_2 \ln r_2 + \bar{x}_2 - \bar{x}_1 + \bar{y} (\theta_1 - \theta_2) \quad (2.2)$$

$$\Psi_j^{\gamma^-}(x, y) = \left[ (\bar{x}_1 + \bar{x}_2) \Psi_j^{\gamma^+} + r_2^2 \ln r_2 - r_1^2 \ln r_1 + \frac{1}{2} (\bar{x}_1^2 - \bar{x}_2^2) \right] \frac{1}{\bar{x}_1 - \bar{x}_2} \quad (2.3)$$

$$\Psi_j^\sigma(x, y) = \bar{x}_2 \theta_2 - \bar{x}_1 \theta_1 + \bar{y} \ln \frac{r_1}{r_2} \quad (2.4)$$

Because the stream function must be some constant  $\Psi_0$  on a wall in potential flow theory, and if the Kutta condition is applied such that  $\gamma_1 + \gamma_N = 0$ , a  $(N + 1) \times (N + 1)$  linear system of equations can be formed. The linear system is solved using Gaussian elimination, giving the airfoil surface vorticities [29].

### 2.1.2 Integral Boundary Layer

This section briefly provides an overview of the viscous formulation employed by XFOIL. The viscous formulation is discussed in much greater detail in references [29, 30]. XFOIL uses the integral momentum and kinetic energy shape parameter equations that take the forms shown in equations 2.5 and 2.6.

$$\frac{d\theta}{d\xi} + (2 + H - M_e^2) \frac{\theta}{u_e} \frac{du_e}{d\xi} = \frac{C_f}{2} \quad (2.5)$$

$$\theta \frac{dH^*}{d\xi} + [2H^{**} + H^*(1 - H)] \frac{\theta}{u_e} \frac{du_e}{d\xi} = 2C_D - H^* \frac{C_f}{2} \quad (2.6)$$

A maximum rate of shear stress coefficient gives a third equation,

$$\frac{\delta}{C_\tau} \frac{dC_\tau}{d\xi} = 5.6 \left( C_{\tau_{EQ}}^{1/2} - C_\tau^{1/2} \right) + 2\delta \left\{ \frac{4}{3\delta^*} \left[ \frac{C_f}{2} - \left( \frac{H_k - 1}{6.7H_k} \right)^2 \right] - \frac{1}{u_e} \frac{du_e}{d\xi} \right\} \quad (2.7)$$

Each variable in Equations 2.5, 2.6, and 2.7 can be defined in terms of  $\theta$ ,  $\delta^*$ ,  $C_\tau$ , and  $u_e$ , the details of which can be found in reference [29]. The equations are discretized using a two-point central difference formulation. The viscous and inviscid equations together form a coupled, nonlinear system that are solved using a Newton method to give the panel source strengths.

### 2.1.3 Geometry Construction

In addition to some built-in NACA airfoils, XFOIL allows the user to import airfoils for analysis and offers tools to modify the airfoils. This section describes the method used to generate airfoils for analysis.

Most of the publicly available experimental hinge moment data precedes the age of inexpensive data storage. As a result, the airfoil coordinates are manually transcribed from written reports into a digital format. After digitization, a custom program is used to fit a cubic spline through the ordinates. The program then outputs points based on user-defined parameters. In this way, it is possible to fill gaps between known ordinates to obtain a

higher-fidelity airfoil.

Observation of the airfoil coordinates often reveals rounding errors introduced at the time of the experimental airfoil measurement. The slight rounding errors result in an airfoil surface that is wavy, particularly in regions with a greater number of points. When such errors are identified, the ordinates are altered slightly to create a spline which reduces the cubic oscillations in the spline. Such alterations are limited to a range that give identical measurements when rounded with the same precision as the coordinates provided in the reference.

Once the airfoil shape is corrected, it is imported into XFOIL. The panel discretization is performed using the maximum number of panels allowed by the program, which is 340 airfoil panels for a 64-bit system. Using the maximum number of panels gives the most precise results. The computational efficiency of panel method codes is such that performance is no concern for a typical user.

#### 2.1.4 XFOIL Control Surface Deflection

XFOIL has built-in tools that can be used to simulate a control surface on airfoil. The upper and lower surfaces are deflected about a user-specified hinge axis. Continuity and smoothness are maintained by using a tangent arc on both surfaces. This flap deflection method is limited to simple flaps with no overhanging balance. It is also important to note that multi-element sections are not possible in XFOIL. This means that hinge gaps cannot be modeled. An example of the resulting geometry is shown in Figure 2.3.

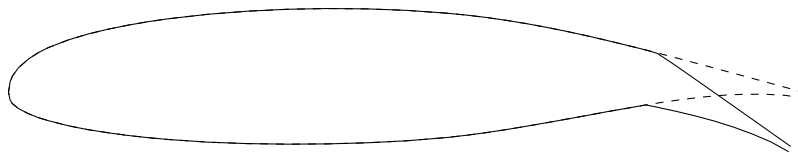


Figure 2.3: GA(W)-1 airfoil with XFOIL flap deflection.

## 2.2 Navier-Stokes CFD Solver (Fun3D)

FUN3D is a state-of-the-art CFD code developed by the Computational Aerosciences Branch at NASA Langley Research Center [31]. It has been actively developed since its conception in the 1980s. FUN3D is a fully-unstructured, node-centered CFD solver with an impressive range of capabilities. It can solve problems in 2D and 3D using inviscid, laminar, or turbulent governing equations.

FUN3D is a highly-parallel program which uses MPI to communicate information between processors. Domain partitioning is done using ParMETIS [32]. FUN3D can also be coupled with optimization programs such as MASSOUD [33] and BandAids [34] to solve inverse design problems. It is also capable of solving problems on moving geometries, including overset grids using SUGGAR++. It also has the capability to solve both ideal and real gas dynamics problems.

### 2.2.1 Governing Equations

The governing equations that drive CFD solvers are the Navier-Stokes equations. The continuity equation enforces that the time rate of change of mass in the system must equal the mass flux across the system boundary.

$$\frac{\partial \rho}{\partial t} + \nabla \cdot (\rho \vec{\mathbf{v}}) = 0 \quad (2.8)$$

Three additional equations come from conservation of momentum, which balances the inertia of the system with the forces acting on the system.

$$\frac{\partial}{\partial t} (\rho \vec{\mathbf{v}}) + \nabla \cdot (\rho \vec{\mathbf{v}} \vec{\mathbf{v}}) = -\nabla p + \nabla \cdot \overline{\overline{\boldsymbol{\tau}}} + \rho \vec{\mathbf{g}} \quad (2.9)$$

Here,  $p$  is the pressure and  $\vec{\mathbf{g}}$  is the body acceleration acting on the continuum. The viscous stress tensor  $\overline{\overline{\boldsymbol{\tau}}}$  is

$$\overline{\overline{\boldsymbol{\tau}}} = \mu \left[ (\nabla \vec{\mathbf{v}} + \nabla \vec{\mathbf{v}}^T) - \frac{2}{3} \nabla \cdot \vec{\mathbf{v}} I \right] \quad (2.10)$$

Equations 2.8 and 2.9 give four equations with five unknowns  $(\rho, \vec{v}, p)$ . Conservation of energy provides a fifth equation.

$$\begin{aligned} \frac{\partial}{\partial t} \left[ \rho \left( e + \frac{V^2}{2} \right) \right] + \nabla \cdot \left[ \rho \left( e + \frac{V^2}{2} \right) \vec{v} \right] &= \rho \dot{q} - \nabla \cdot (p \vec{v}) + \rho (\vec{g} \cdot \vec{v}) \\ &- \nabla \cdot p \vec{v} + \overline{\overline{\tau}} : \nabla \vec{v} \\ &+ \nabla \cdot (k \nabla T) \end{aligned} \quad (2.11)$$

Here,  $e$  is the specific internal energy and  $k$  is the thermal conductivity. The left side of this equation contains the kinetic energy terms. The first term on the right side is the heat addition, followed by the work done by pressure forces and body forces. The second line of the equation pertains to the work done by viscous forces, and the last term in the equation is the viscous heating term.

Equation 2.11 introduces both internal energy  $e$  and temperature  $T$  as unknown variables. However, if the gas can be considered calorically perfect, then

$$e = c_v T \quad (2.12)$$

where  $c_v$  is the specific heat at constant volume, which is specific to the gas. The system can be completed by using the ideal gas equation of state

$$p = \rho R T \quad (2.13)$$

where  $R$  is the specific gas constant.

The governing equations can also be written in integral form for a control volume  $\Omega$  bounded by a control surface  $S$ . Equations 2.14, 2.15, and 2.16 are the integral forms of the continuity, momentum, and energy equations.

$$\frac{\partial}{\partial t} \iiint_{\Omega} \rho d\Omega + \iint_S \rho \vec{v} \cdot \vec{dS} = 0 \quad (2.14)$$

$$\frac{\partial}{\partial t} \iiint_{\Omega} \rho \vec{v} \, d\Omega + \iint_S (\rho \vec{v} \cdot \vec{dS}) \vec{v} = - \iint_S p \vec{dS} + \iiint_{\Omega} \rho \vec{g} \, d\Omega + \iint_S \vec{\tau} \cdot \vec{dS} \quad (2.15)$$

$$\begin{aligned} \iiint_{\Omega} \dot{q} \rho \, d\Omega + \dot{Q}_{\text{viscous}} - \iint_S p \vec{v} \cdot \vec{dS} + \iiint_{\Omega} \rho (\vec{g} \cdot \vec{v}) \, d\Omega + \dot{W}_{\text{viscous}} \\ = \frac{\partial}{\partial t} \iiint_{\Omega} \rho \left( e + \frac{V^2}{2} \right) \, d\Omega + \iint_S \rho \left( e + \frac{V^2}{2} \right) \vec{v} \cdot \vec{dS} \end{aligned} \quad (2.16)$$

In addition to the viscous governing equations, the Spalart-Allmaras turbulence model is used in this study. The Spalart-Allmaras model is a one-equation model that solves a modeled transport equation for the turbulent eddy viscosity [35].

### 2.2.2 Finite Volume Method

FUN3D is a node-centered finite volume code. In the finite volume method, the problem control volume is divided into discrete elements. The integral form of the governing equations are applied to each element, under the assumption that the elements are small enough to consider the flux across each face of the element to be uniform. The finite volume elements are then assembled into a complete system and solved iteratively.

FUN3D employs an upwind differencing scheme for the spatial calculations, and offers multiple schemes for temporal calculations. The present work uses the second-order upwind differencing scheme in space and the second-order backward differencing scheme in time.

### 2.2.3 2D Mesh Generation

Meshes for 2D geometries in this study are created using AFLR2, an unstructured grid generation software application developed by Prof. David Marcum at Mississippi State University. Custom programs wrap AFLR2 to simplify the use of the software. A spline airfoil is first generated using the methods described in §2.1.3. A script then reads the spline output file and generates the requisite AFLR2 input files. AFLR2 is then called and the resulting mesh is displayed to the user, at which point the user can determine if the mesh is of sufficient quality to proceed. This method of mesh generation is very efficient for the user. Once provided with a spline, typical mesh generation takes only a few seconds. The automated nature of the process simplifies the mesh generation and alteration process for the user.

#### 2.2.4 3D Mesh Generation

3D configurations require more manual interaction than their 2D counterparts. Script-generated airfoils are imported into a CAD package. If the wing airfoil varies with span, multiple airfoil splines must be created to enable the creation of a lofted surface in the CAD program. A 3D CAD model of a wing is typically completed by lofting through multiple airfoil sections. Special care must be taken to ensure that the CAD model represents reality.

The complete CAD model is then imported into Pointwise, a structured and unstructured grid generator. Some simple operations are performed to ensure that each part of the geometry is a single watertight model. The surface meshes are constructed manually. The user specifies grid spacing boundary conditions on surface edges, and the built-in solver finds a mesh that fits the user-specified constraints. Surface mesh generation is a time-consuming process that is critical to the final volumetric mesh. The volumetric mesh is generated by the volumetric mesh solving algorithm in Pointwise based on the user-specified boundary conditions. After a suitable mesh is obtained, flow boundary conditions are set, and the final mesh is exported to a double-precision binary UGRID mesh file.

## CHAPTER 3

### INVESTIGATION OF A GA(W)-1 AIRFOIL WITH 20% PLAIN FLAP

The General Aviation (Whitcomb) number 1 (GA(W)-1) airfoil was developed by NASA Langley Research Center in the 1970s [36]. Wentz, et al. [37] later tested a GA(W)-1 airfoil with a 20% plain flap and obtained hinge moment measurement data for various angles of attack and deflection angles. The quantity and quality of data reported by Wentz, et al. are sufficient to create a CFD model and compare results. The airfoil was later redesignated as the NASA LS(1)-0417, and it became the basis for the LS(1) series of airfoils [38]. To avoid confusion when comparing CFD results to the reference data, the airfoil is referred by its original name of GA(W)-1 in this thesis.

#### 3.1 Geometry Description

The GA(W)-1 airfoil is a 17% thick airfoil featuring a large upper surface leading-edge radius in order to delay stall at high angles of attack. To further delay stall, the top and bottom surfaces are nearly parallel at the blunt trailing edge. The GA(W)-1 is also designed to have a nearly uniform pressure distribution near  $C_l = 0.40$  [36].

The selected reference case is the GA(W)-1 airfoil with a 20% plain flap and a 0.5% hinge gap. Wind tunnel tests were conducted by Wentz [37] for a quasi-2D GA(W)-1 airfoil with a 24 in chord. A detailed schematic of the geometry is shown in Figure 3.1. Of the several hinge gaps tested in the reference, the 0.5% hinge gap case is studied in detail in this project due to both the quantity and quality of experimental data. The reference case was tested in the Walter Beech Tunnel at Wichita State University at a Reynolds number of  $2.2 \times 10^6$  and Mach number of 0.13. A summary of reference quantities is provided in Table 3.1.

Table 3.1: GA(W)-1 reference quantities

Quantity	Symbol	Value
Airfoil chord	$c$	24 in
Airfoil thickness-to-chord ratio	$t/c$	0.17
Control surface chord ratio	$c_f/c$	0.20
Hinge axis x-coordinate	$x_h/c$	0.80
Hinge axis z-coordinate	$z_h/c$	0.03443
Reynolds number	Re	$2.2 \times 10^6$
Mach number	$M$	0.13

This test cases is similar to an aircraft with a 2.4 ft chord flying at 86 knots at sea level, making it a suitable analog for an aircraft shortly after takeoff or on approach for landing. Low-speed flight is the type of flight which requires frequent, large-angle deflections of control surfaces. As the flight speed decreases, control surface effectiveness also decreases, so larger deflections are required to induce moments. Wentz conducted wind tunnel tests of the GA(W)-1 airfoil at the following angles of attack and deflection angles:

$$\alpha \in \{-8^\circ, 0^\circ, 8^\circ, 12^\circ, 16^\circ, 20^\circ\}$$

$$\delta \in \{-40^\circ, -20^\circ, -10^\circ, -5^\circ, 0^\circ, 5^\circ, 10^\circ, 20^\circ, 40^\circ\}$$

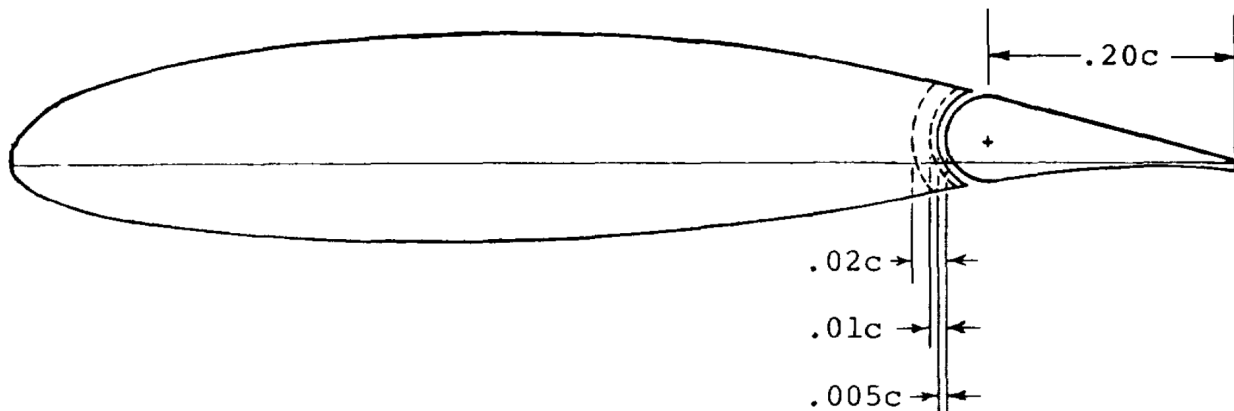


Figure 3.1: GA(W)-1 airfoil with 20% plain flap [37].

### 3.2 Stability and Control Datcom

The relations presented in the *USAF Stability and Control Datcom* [26] provide an empirical approach to predicting hinge moment derivatives. Empirical relations are convenient because they are analytical relations that are trivial to evaluate. The ease of use and the low cost associated with finding a solution is especially useful during conceptual design when frequent design configuration changes require fast, inexpensive solutions.

The Datcom assumes low-speed, attached flow with linear hinge moment behavior. No quantification for hinge gap effects is provided.

The Datcom makes use of several airfoil parameters. Among these are the airfoil thickness-to-chord ratio, the ratio of flap chord to airfoil chord, and three trailing edge angles. The first angle,  $\Phi_{TE}$ , is measured between the lines tangent to the upper and lower surfaces at the trailing edge. A second angle,  $\Phi'_{TE}$ , is measured between the lines between 95% and 99% points on each surface. A third angle,  $\Phi''_{TE}$ , is measured between lines between the 90% and 99% points on each surface. The tangent of each angle is approximated using the average distances from the mean chord line, and these values are used in the Datcom analysis. The values used for the trailing edge angle tangents are shown in Table 3.2. A complete, detailed example of the Datcom procedure is provided in Appendix A.

Table 3.2: GA(W)-1 trailing edge angle tangents

Quantity	Value
$\tan\left(\frac{1}{2}\Phi_{TE}\right)$	0.058
$\tan\left(\frac{1}{2}\Phi'_{TE}\right)$	0.08988
$\tan\left(\frac{1}{2}\Phi''_{TE}\right)$	0.12033

The Datcom computations resulted in the hinge moment derivatives shown in Table 3.3. For the GA(W)-1 airfoil, the Datcom predicts  $C_{h_\alpha} = -0.0064770$  per degree and  $C_{h_\delta} = -0.013591$  per degree. Experimental hinge moment derivatives are calculated using a second-order central difference approximation. Noise in the experimental data may be a contributing

Table 3.3: GA(W)-1 Datcom hinge moment derivative predictions

Source	$C_{h_\alpha}$ (per deg.)	$C_{h_\delta}$ (per deg.)	
		$\Delta\delta = 5^\circ$	$\Delta\delta = 10^\circ$
Reference, at $\alpha = 0; \delta = 0$	-0.008957	-0.01157	-0.013789
Datcom	-0.006477	-0.01359	
% Error	27.69%	17.47%	1.43%

factor to the discrepancy in the results. Using a larger  $\delta$  increment in the central difference formulation for the experimental hinge moment derivatives, the error is only 1.43%. Despite the greater numerical error associated with a larger  $\delta$  step, the value of  $C_{h_\delta}$  obtained by using a larger step size is a better representation of the general trend demonstrated by the experimental data for deflection angles less than about  $10^\circ$ .

To compare with the experimental data obtained by Wentz, and to demonstrate a potential use for the Datcom solution, hinge moments are computed as

$$C_h = C_{h_{00}} + C_{h_\alpha}\alpha + C_{h_\delta}\delta \quad (3.1)$$

where  $C_{h_{00}}$  is the hinge moment coefficient at  $\delta = \alpha = 0$ . For the purposes of this analysis,  $C_{h_{00}}$  is taken to be the experimental value from the reference case. With this analysis, only one data point must be known in order to obtain an estimate for hinge moments.

Figure 3.2 shows the hinge moment coefficient versus deflection angle for all angles of attack using the Datcom relations. For small angles of attack, the hinge moment predictions perform surprisingly well across a wide range of deflection angles. At large angles of attack, errors as large as 25% exist for the zero deflection case. This is due to the 27% error in  $C_{h_\alpha}$ . Additionally,  $C_{h_\delta}$  varies approximately linearly with angle of attack in the reference, as shown in Figure 3.3. Because the Datcom does not account for  $\frac{\partial C_{h_\delta}}{\partial \alpha}$ , it cannot represent a wide range of conditions. In this case, the Datcom predicts hinge moments accurately only for small angles of attack and small deflections.

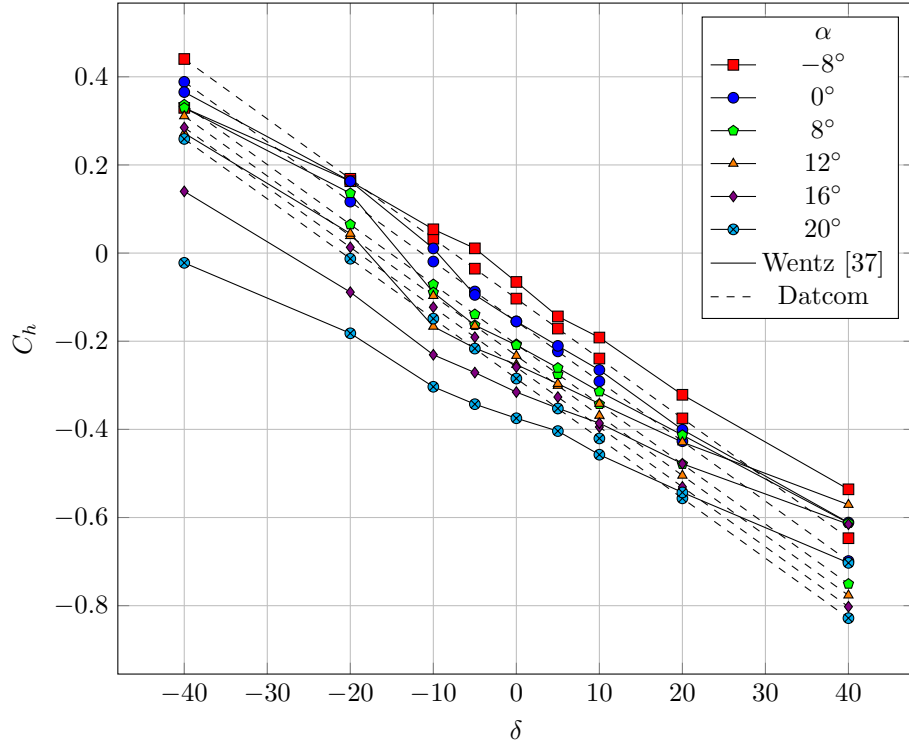


Figure 3.2: GA(W)-1 hinge moments computed using Datcom relations.

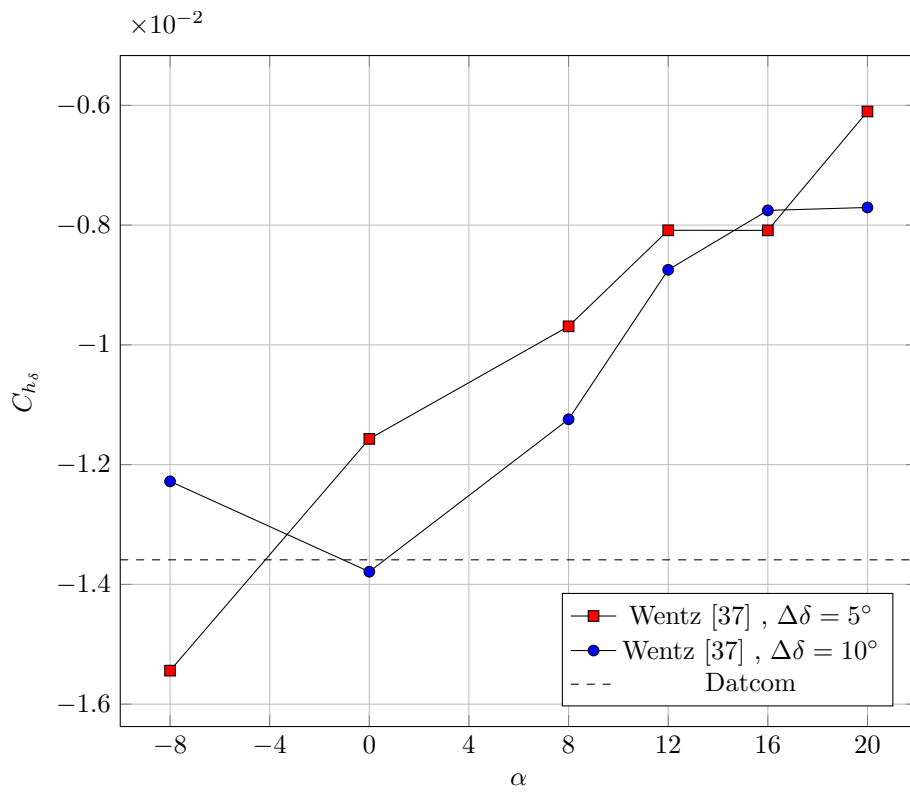


Figure 3.3: GA(W)-1  $C_{h_\delta}$  versus  $\alpha$  for  $\delta = 0$  (using second-order central difference)

In a typical wind tunnel test, an angle of attack sweep is simple to perform. It then stands to reason that a sweep of  $\alpha$  could be conducted with  $\delta = 0$ . If prior knowledge about  $C_h$  exists for zero deflection cases across a range of angle attacks, then the hinge moment coefficient can be predicted using only  $C_{h_\delta}$ .

$$C_h = C_{h_0} + C_{h_\delta} \delta \quad (3.2)$$

where  $C_{h_0}$  is the hinge moment coefficient for a given angle of attack at zero deflection. Again, for this analysis, the reference data is used for the zero deflection case. The results with this second approach are in much better agreement with the reference data, as shown in Figure 3.4. The hinge moments are over-predicted for both positive and negative deflection angles, and the error is larger at high angles of attack. This is not surprising, because the Datcom relations assume no flow separation. At large angles of attack and for large deflection angles, flow separation is likely to occur on any control surface. This is also a reason for the change in  $C_{h_\delta}$  with angle of attack, a behavior which is not captured by the Datcom.

There is a significant opportunity for errors in reading the figures presented in the Datcom. Each additional figure amplifies any prior interpretation or interpolation error. If just a 1% error is introduced with each figure read, then the overall margin for error is 4.1%. This value only includes the error in reading the figures. The Datcom does not provide a correction for the hinge gap present on most control surface configurations. The Datcom is also based on empirical data, so there is a considerable margin for error inherent in the analysis. Despite the errors, the Datcom solution gives a fairly accurate value of  $C_{h_\delta}$  at small angles of attack. An estimate for  $C_h$  is not feasible without some knowledge about the hinge moment coefficient for one condition at least. The Datcom method is best suited to a basic conceptual design, when a fast solution is preferable to expensive, highly-detailed solutions.

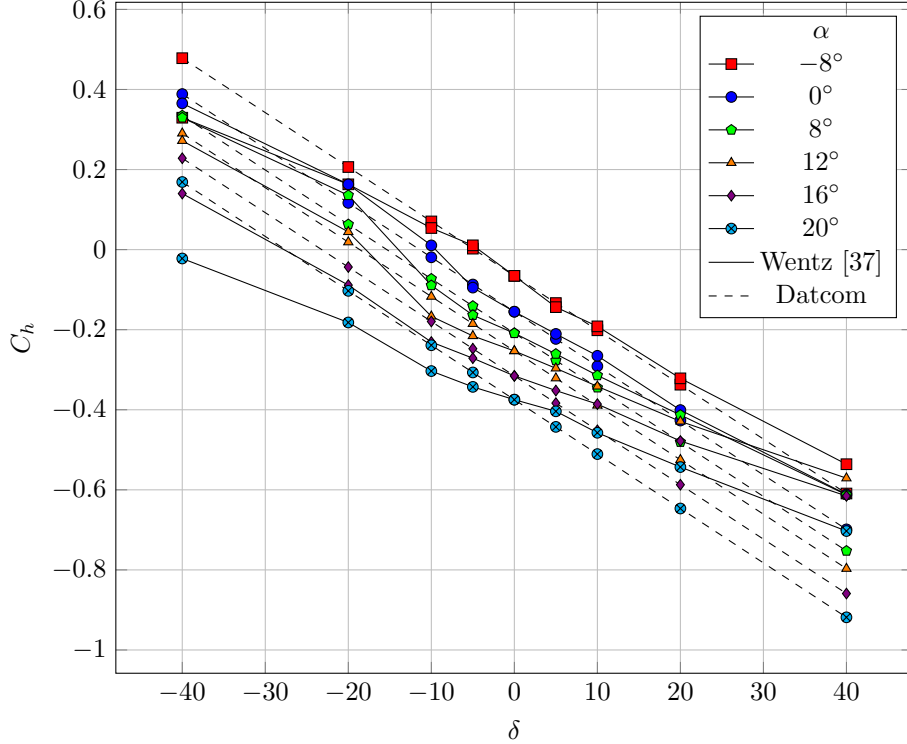


Figure 3.4: GA(W)-1 hinge moments computed using Datcom relations with reference  $C_{h_0}$ .

### 3.3 XFOIL Results

This section details the hinge moment calculation results for the GA(W)-1 airfoil using XFOIL. As a fast, low-fidelity solver, XFOIL is a suitable test to determine the lower feasible limit of hinge moment computation.

The GA(W)-1 airfoil is modeled using the procedure described in §2.1. Figure 3.5 shows the panels used in this analysis. The airfoil is divided into 340 discrete panels, with a maximum angle of 3.53 degrees between consecutive panels. The flap deflections are introduced to the base airfoil using angles ranging from  $-40^\circ$  to  $40^\circ$  in increments of  $5^\circ$ . The speed of XFOIL allows many deflection angles to be tested in a short time. An angle of attack sweep is then performed for each deflection angle, using the same angles of attack as the reference. This entire process is automated using custom Bash scripts that wrap XFOIL and pass commands to the user interface. The source code for these scripts are provided in Appendices C and D.

User interaction is minimal using this approach. The only inputs required by the script are a file containing airfoil coordinates, a set of desired deflection angles and angles of attack, Reynolds number, and Mach number. A complete run with 17 values of  $\delta$  and six  $\alpha$  sweeps takes 6.08 minutes to complete on a single Intel Xeon E5-2670 processor at 2.50 GHz. The script outputs the data into a format convenient for post-processing.

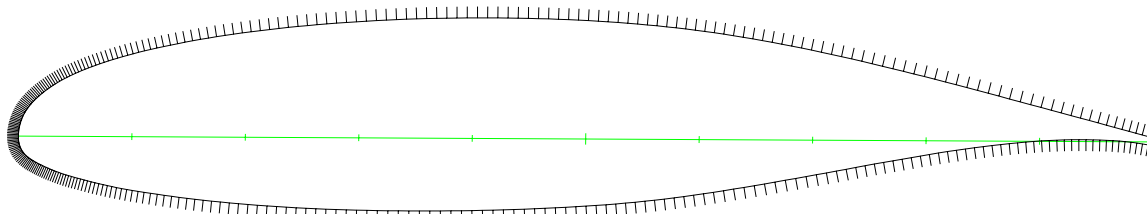


Figure 3.5: GA(W)-1 XFOIL panels.

Figure 3.6 shows the hinge moments computed by XFOIL for the GA(W)-1 test case. The hinge moments computed by XFOIL are in much better agreement with the experimental data than the Datcom predictions in the previous section. At low angles of attack and low to moderate deflection angles, the hinge moment prediction is suitable for a conceptual design analysis. There is significant error in the results at large deflection angles and moderate to high angles of attack. The results show a tendency for XFOIL to under-predict hinge moments at large angles of attack, which is not surprising given the tendency of airfoils to have flow separation in those conditions.  $C_{h_\delta}$  is surprisingly consistent with the reference case across all angles of attack. This behavior is demonstrated by the manner in which the computational results follow similar trends to the reference experimental data.

Flow separation ultimately limits the solution accuracy, as XFOIL's methodology is not designed for computing separated flows. Due to the inherent separation and unsteadiness in flows over a control surface, XFOIL is less useful for large deflection angles or angles of attack.

Agreement between computed lift coefficients and experimental values is poor compared to the hinge moments. As with the hinge moments, large deflection angles and angles of

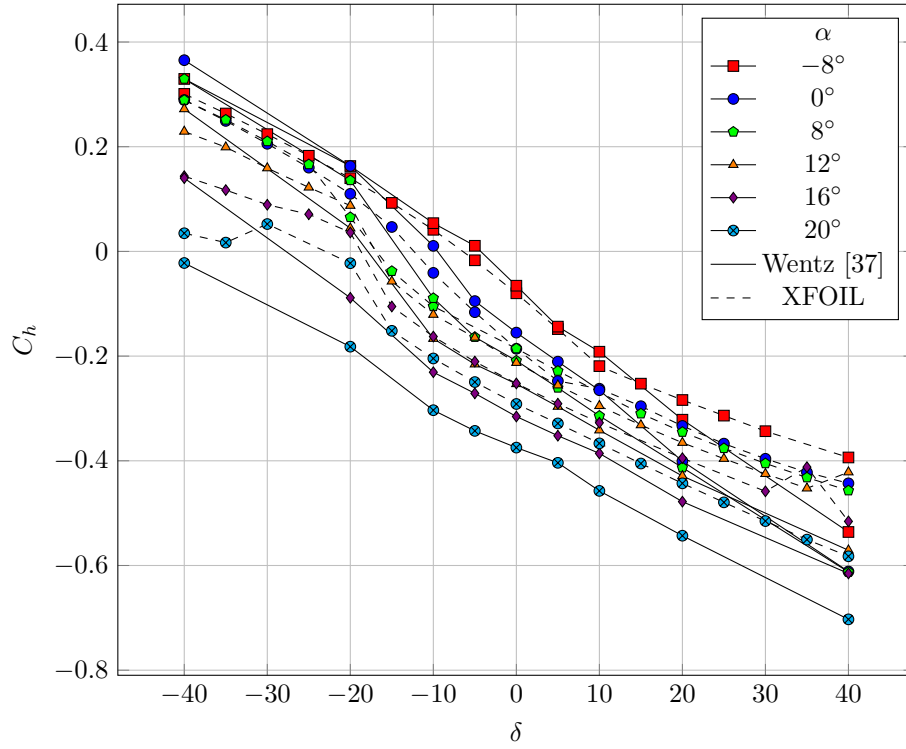


Figure 3.6: GA(W)-1 hinge moments computed by XFOIL.

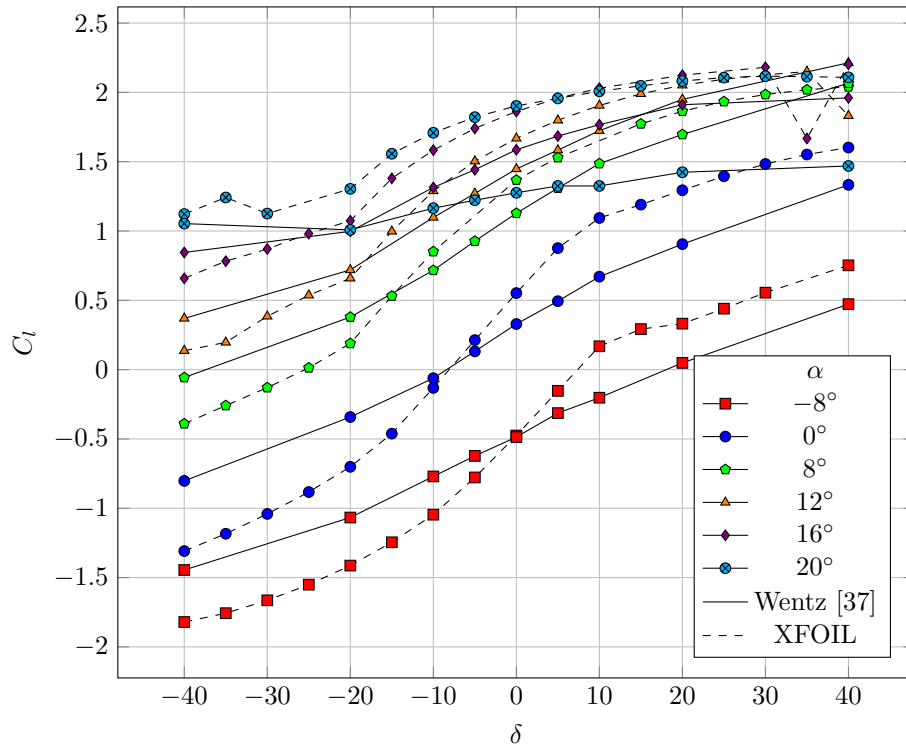


Figure 3.7: GA(W)-1 lift coefficient computed by XFOIL.

attack are problematic due to the presence of flow separation. Figure 3.7 shows an over-prediction of the overall wing lift with respect to flap deflection. Furthermore, the experimental values are relatively linear, whereas the lift coefficient computed by XFOIL is much more nonlinear. Contrary to expectations,  $C_{l_\delta}$  is in poor agreement with the experimental data for small deflection angles. One possible explanation of the over-prediction of lift is the absence of a hinge gap in the XFOIL model.

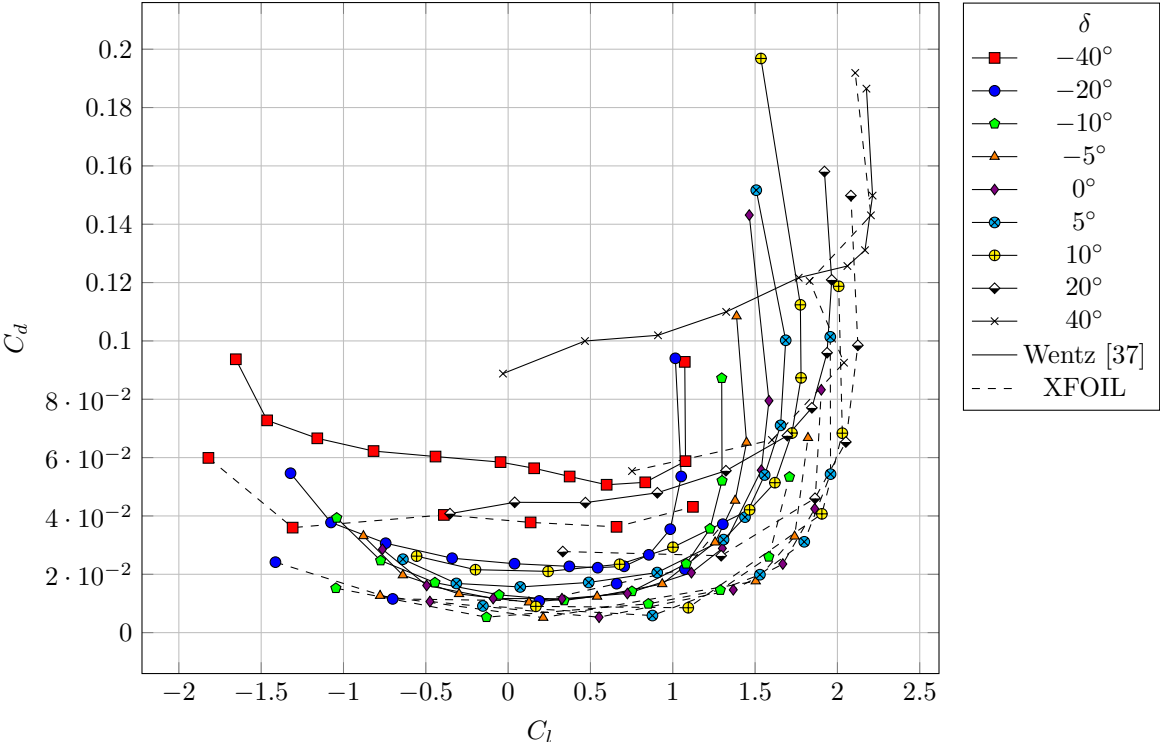


Figure 3.8: GA(W)-1 drag polar computed by XFOIL.

A drag polar for this test case is shown for all deflection angles in Figure 3.8, as well as for small deflections in Figure 3.9. The airfoil drag is significantly under-predicted in this test case. The drag prediction is poor for large deflections. Even small deflections give error on the order of 50%.

While XFOIL is capable of demonstrating some basic hinge moment trends, it is not suitable for anything more than a basic conceptual analysis due to its inability to accurately resolve the boundary layer in the presence of flow separation. Furthermore, the overall

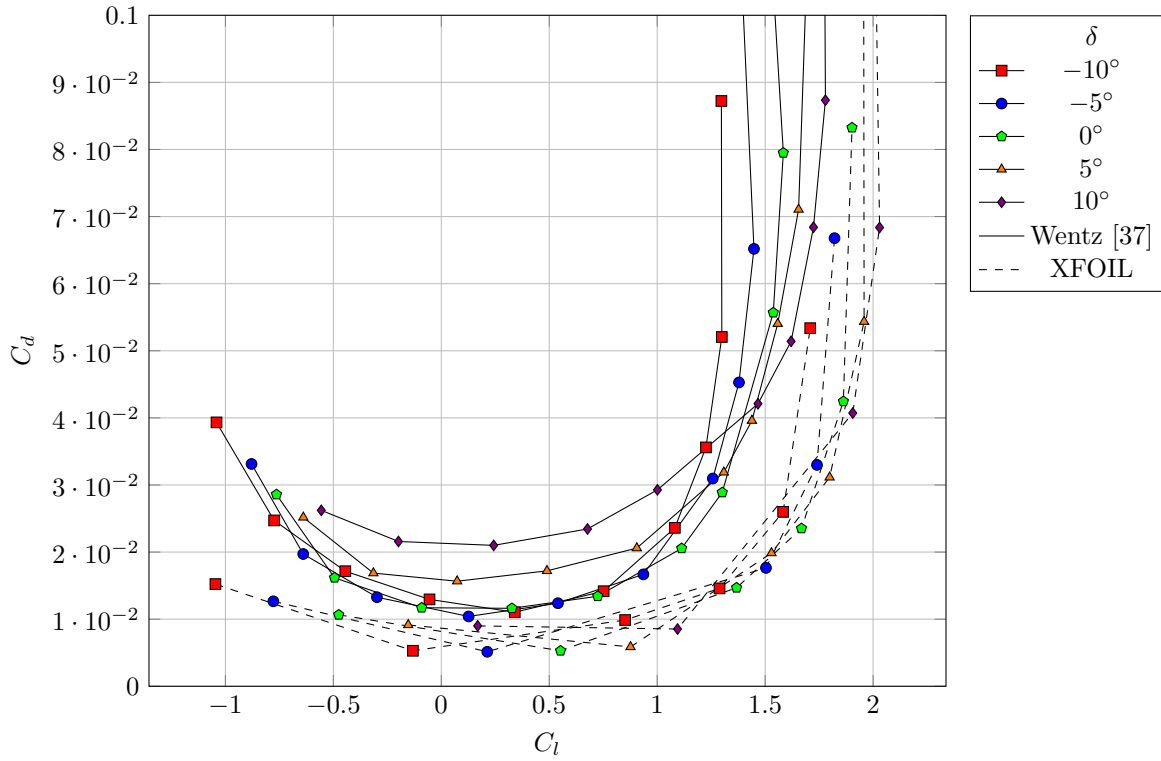


Figure 3.9: GA(W)-1 drag polar computed by XFOIL (small deflections).

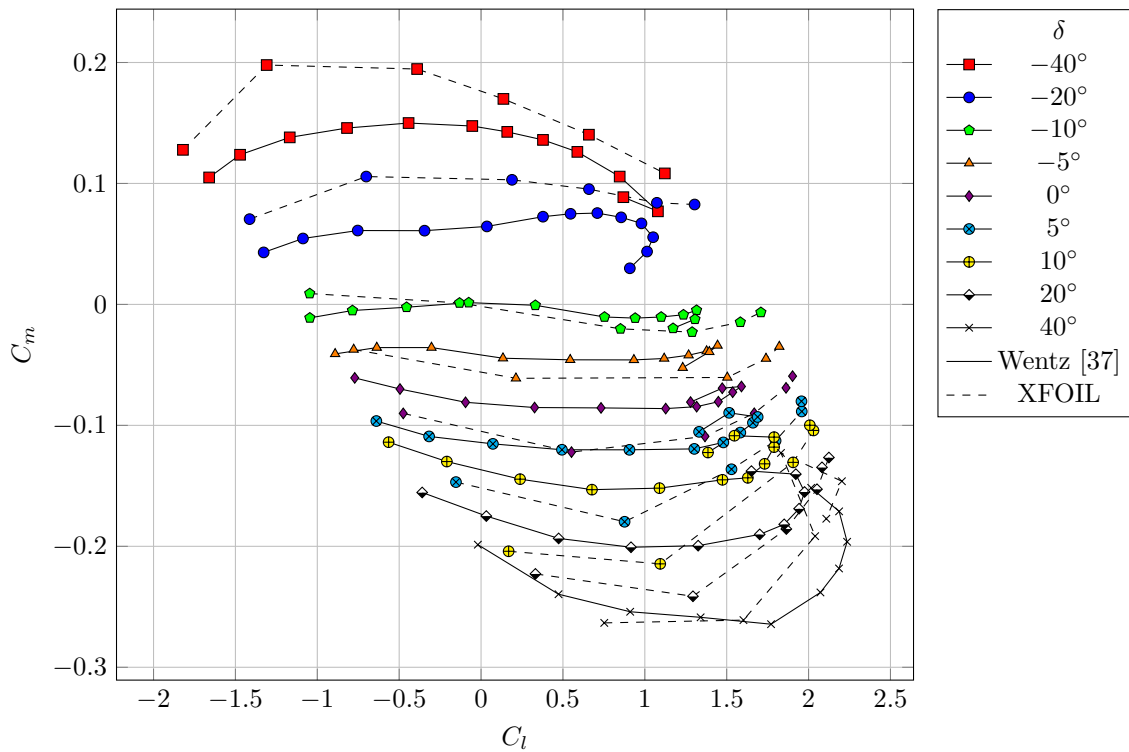


Figure 3.10: GA(W)-1 moment computed by XFOIL.

lift, drag, and moment calculations are insufficient for detailed design analysis due to large inaccuracies. XFOIL is also limited in application because it is purely a two-dimensional solution, and most problems are three-dimensional.

### 3.4 Viscous Navier-Stokes Results

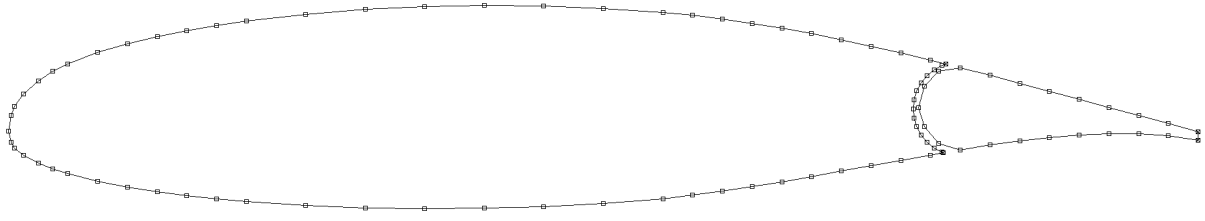
This section details the use of FUN3D to solve for hinge moments on the GA(W)-1 airfoil. A brief discussion of the mesh generation process is given. Numerical results are discussed in detail for both steady-state and time-accurate solutions. Key solver parameters used in the analysis are also discussed.

#### 3.4.1 Mesh Generation

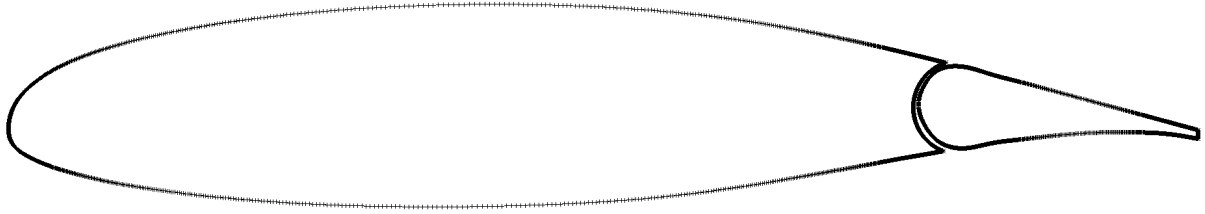
A purely triangular 2D mesh is generated using the procedure outlined in §2.2.3. Figure 3.12 shows the mesh for the zero deflection case. The airfoil has a chord of 24 in, and the farfield is a circle with a 2,000 in radius, which is  $83.3c$ . Experience shows that this is sufficiently far from the geometry to avoid numerical interactions from the imposed farfield boundary condition.

AFLR2 requires a set of discrete surface points. The provided airfoil coordinates are insufficient for a detailed CFD analysis. To add more surface nodes, a program called Splineview is used to fit a spline to the known coordinates and add nodes with given spacing parameters. Figure 3.11 shows the initial airfoil coordinates provided by the reference, as well as the spline and nodes added by Splineview.

The reference coordinates were obtained by Wentz via hand measurements of the wind-tunnel model. As a result, there is some uncertainty in the provided coordinates, which causes some poor surface geometry. The leading edge of the control surface is the primary affected area. The leading edge radius of the control surface was provided in the reference, but that radius was found to be too large to fit within the thickness of the airfoil at the hinge location. The measured coordinates also do not match the provided radius. If the



(a) Initial airfoil coordinates



(b) Final fitted spline nodes

Figure 3.11: GA(W)-1 initial coordinates and connectivity and final fitted spline.

provided radius was used, the control surface would have corners near the hinge line where the radius intersects the airfoil surface definition. It is unlikely that a physical wind-tunnel model would be constructed in that manner, so the published coordinates of the physical model were used.

The most ill-defined region of the surface geometry is in the vicinity of the hinge gap. Any pressure changes in the gap will have a negligible effect on the hinge moments because the surface normals are approximately aligned with the hinge axis. Due to the relatively low velocities through the gap and the proximity to the hinge axis, viscous forces on the leading edge of the control surface are unlikely to have a significant impact on hinge moments. Gap flow will affect the hinge moments primarily by reducing the pressure differential between the upper and lower surfaces. Wentz shows for this geometry that while the presence of a hinge gap affects hinge moments, the size of the gap has little effect on the hinge moment [37]. For these reasons, the numerical model is considered to be good enough for use in computational results.

Nodes are clustered near the leading and trailing edges, as well as in the area surrounding

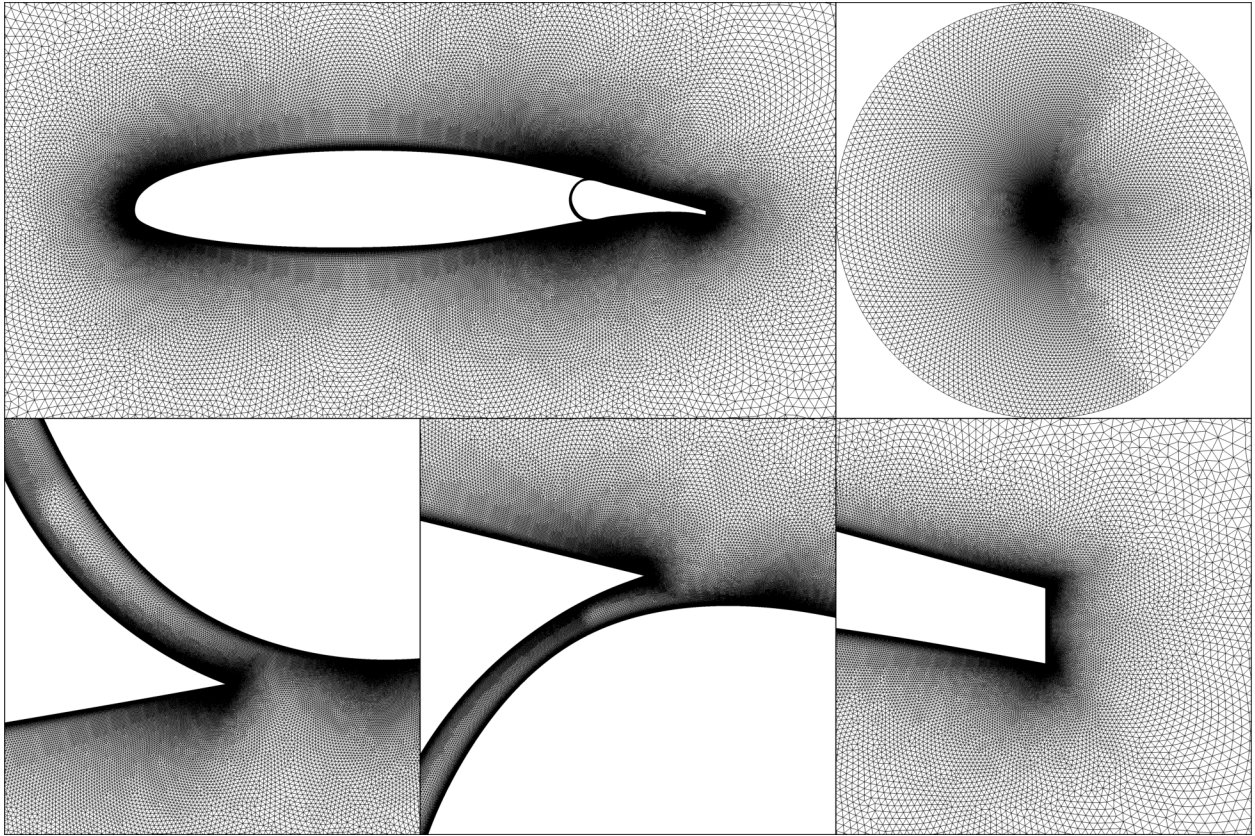


Figure 3.12: GA(W)-1 mesh used in FUN3D.

the gap. This is accomplished by specifying a spacing near these regions of  $0.5 \times 10^{-3}$  in and also by specifying the number of nodes for each segment of the airfoil. The blunt trailing edge contains 129 nodes to ensure that separation can be captured with sufficient accuracy. To accurately capture the boundary layer for the viscous solution, the mesh is generated with a normal spacing of  $10^{-5}$  in. The normal spacing is determined by finding the theoretical spacing that gives  $y^+ = 0.7$  on the first element for a flat plate at the reference Reynolds number, and then a smaller value is chosen to account for the airfoil thickness. For all steady-state solutions in this study, the actual value of  $y^+$  is less than 0.24.

Control surface deflections are applied after the spline fit and prior to mesh generation. This was done by performing a simple rotation operation on the spline coordinates about the hinge axis using a spreadsheet program. The new points were then exported and used in AFLR2 to generate a mesh. In this way, the surface definition is identical for each deflection angle, and the automated process produces a similar mesh topology for each case. Applying the control surface deflection via mesh deformation is possible in FUN3D, but it could result in stretched cells in the hinge gap and on the low-pressure side of the control surface where grid resolution is critical.

A global grid refinement study is performed for one configuration of this geometry, with  $\alpha = 0^\circ$  and  $\delta = 5^\circ$ . The global meshes are generated using the processes described in §2.2.3. The process for generating multiple levels of refinement starts with an initial surface mesh for the finest case. The surface definition is used to generate the flow field mesh. The surface mesh is then coarsened by removing every second node, and another mesh is generated. This process repeats, giving several meshes which contain approximately double the number of nodes as the next coarsest mesh.

Figure 3.13 shows the hinge moment coefficient versus number of grid nodes in the 2D flow field for case of  $\alpha = 0^\circ$  and  $\delta = 5^\circ$ . The values are also given in Table 3.4.

Table 3.4: GA(W)-1 global grid convergence study hinge moments,  $\alpha = 0^\circ$ ,  $\delta = 5^\circ$ .

2D Grid Nodes, $N$	$h = \frac{1}{\sqrt{N}}$	$C_h$
18,654	0.007322	-0.2581
39,295	0.005045	-0.2168
87,636	0.003378	-0.2011
230,277	0.002084	-0.1942
435,955	0.001515	-0.1930

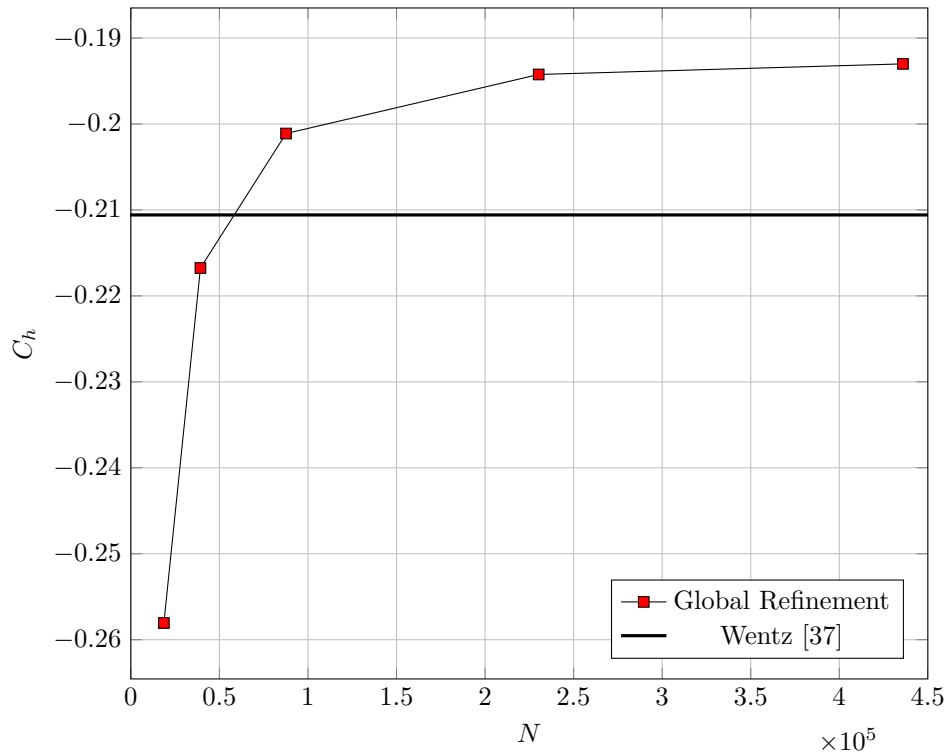


Figure 3.13: GA(W)-1 global mesh refinement study,  $\alpha = 0^\circ$ ,  $\delta = 5^\circ$ .

### 3.4.2 Steady-State Navier-Stokes Solution

A steady-state Navier-Stokes CFD solution is obtained using FUN3D for each available reference point for the 0.5% hinge gap case. This includes the following deflection angles and angles of attack:

$$\delta \in \{-40^\circ, -20^\circ, -10^\circ, -5^\circ, 0^\circ, 5^\circ, 10^\circ, 20^\circ, 40^\circ\}$$

$$\alpha \in \{-8^\circ, 0^\circ, 8^\circ, 12^\circ, 16^\circ, 20^\circ\}$$

All cases are solved at  $M = 0.13$  and  $Re = 2.2 \times 10^6$ , using the compressible, viscous governing equations and the Spalart-Allmaras turbulent model. Each test case is run on a total of 48 cores on three Dell M620 nodes of the UAHPC cluster at the University of Alabama (formerly known as RC2).

Figure 3.14 shows hinge moments versus deflection angle for each angle of attack tested. The steady-state Navier-Stokes solution is in much better agreement with the reference data than the XFOIL solution. At small angles of attack, the numerical solution closely matches the experimental data for all but the largest deflection angle. The largest deflection angle gives poor agreement for all angles of attack. At high  $\alpha$  values, the solution is poor for all deflection angles, although the solution is in closer agreement than the XFOIL solution. The quantities are provided in Tables 3.7 – 3.12.

The error at large deflection angles is most likely attributed to flow separation and unsteady effects that are not being captured with the steady-state solution. At high  $\alpha$  values, the flow separates on the upper surface of the wing, and the effects are not adequately captured by the steady-state solution.

Figure 3.15 shows the flow field Mach number and stream traces for the zero angle of attack case. At all deflection angles, flow separation is clearly visible on the low-pressure side of the control surface. The size of the separation bubble increases with deflection angle. For  $\delta$  less than  $20^\circ$  in either direction, the separation is limited to the trailing edge of the

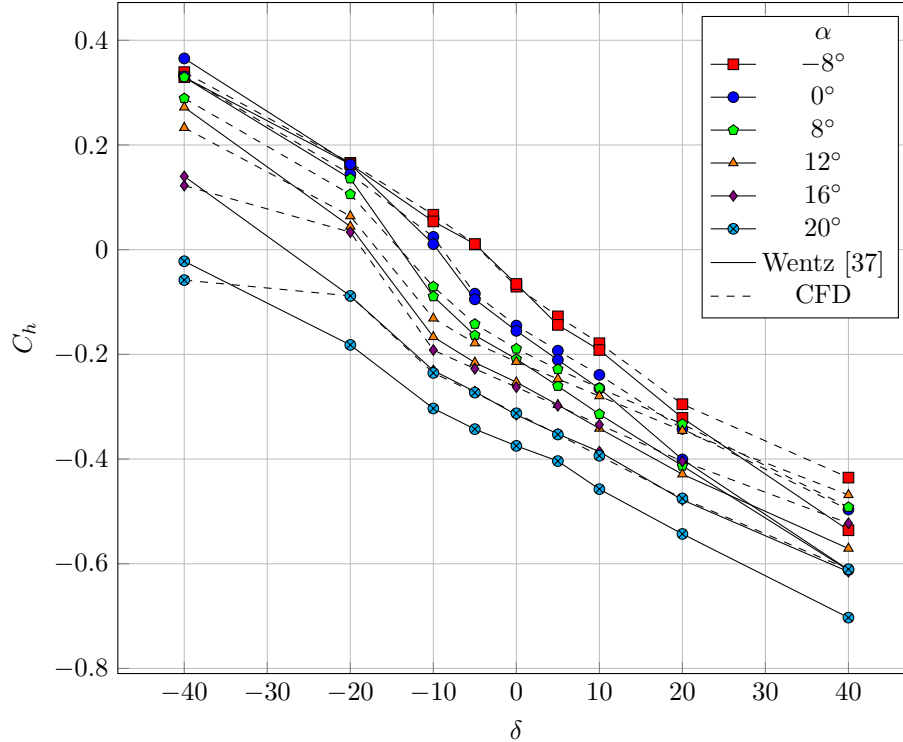


Figure 3.14:  $C_h$  versus  $\delta$ , steady FUN3D.

control surface. It is possible that the separation bubble is stationary in these cases, in which case a steady-state solution may be sufficient to capture the flow physics. However, in the cases with larger deflections, the separation resembles that of a bluff body. A bluff body will shed vortices periodically, and this flow behavior can not be captured adequately by a steady-state solution. This behavior is reflected in the hinge moment results. There is also a small region of separation on the high-pressure side of the control surface in the vicinity of the gap, resulting in a stagnation point near the middle of the control surface.

Figure 3.16 shows the Mach number and stream traces for zero deflection angle over the range of  $\alpha$ . The GA(W)-1 airfoil starts to display signs of trailing edge separation at an angle of attack of just  $8^\circ$ . At  $20^\circ$ , the airfoil has a region of separation that covers the aft half of the airfoil. Again, the steady-state solution is unable to accurately capture the inherently unsteady separated flow.

Figure 3.17 shows the pressure coefficient contours for the zero angle of attack case. The

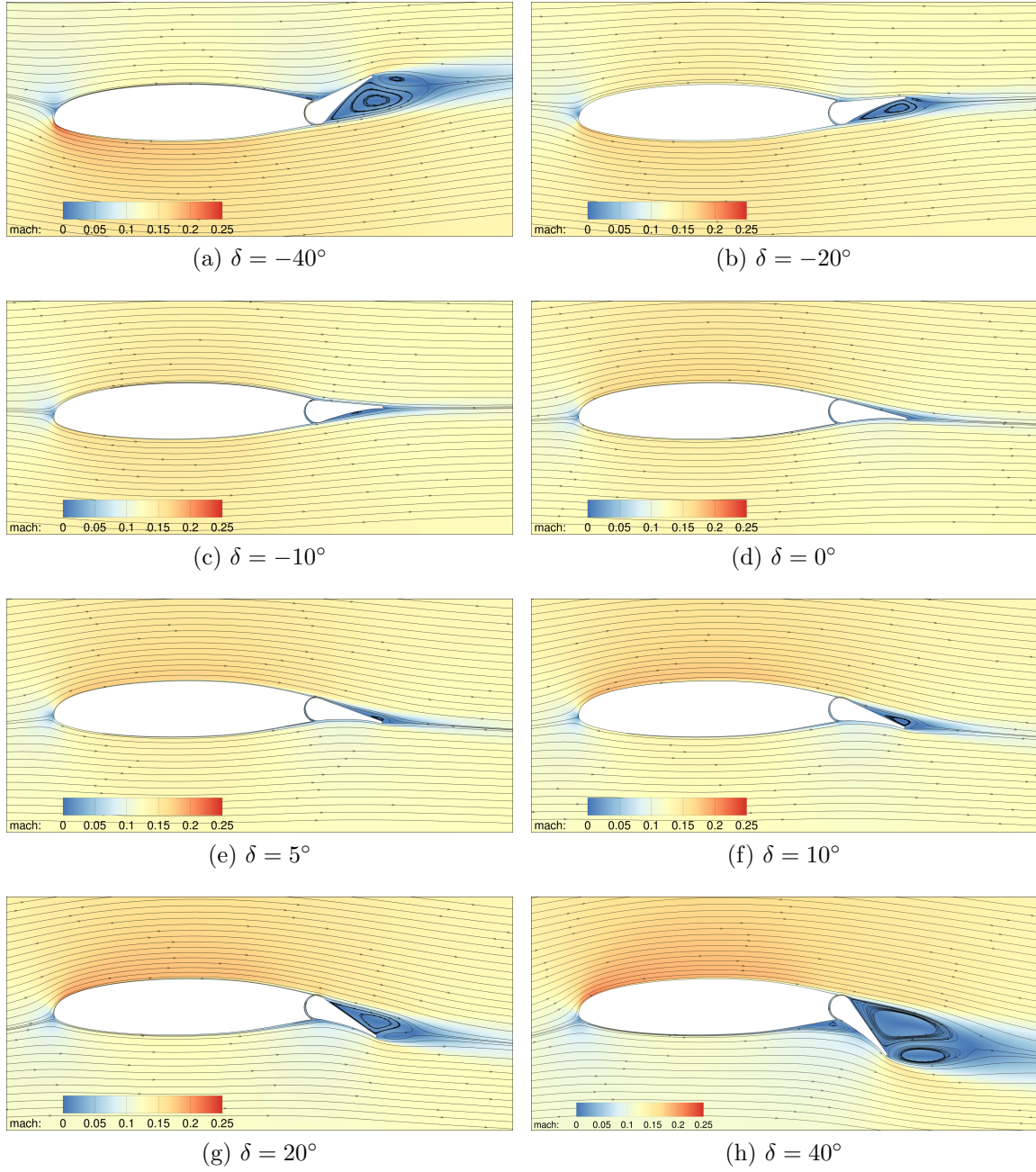


Figure 3.15: GA(W)-1 steady-state flow field Mach number,  $\alpha = 0^\circ$

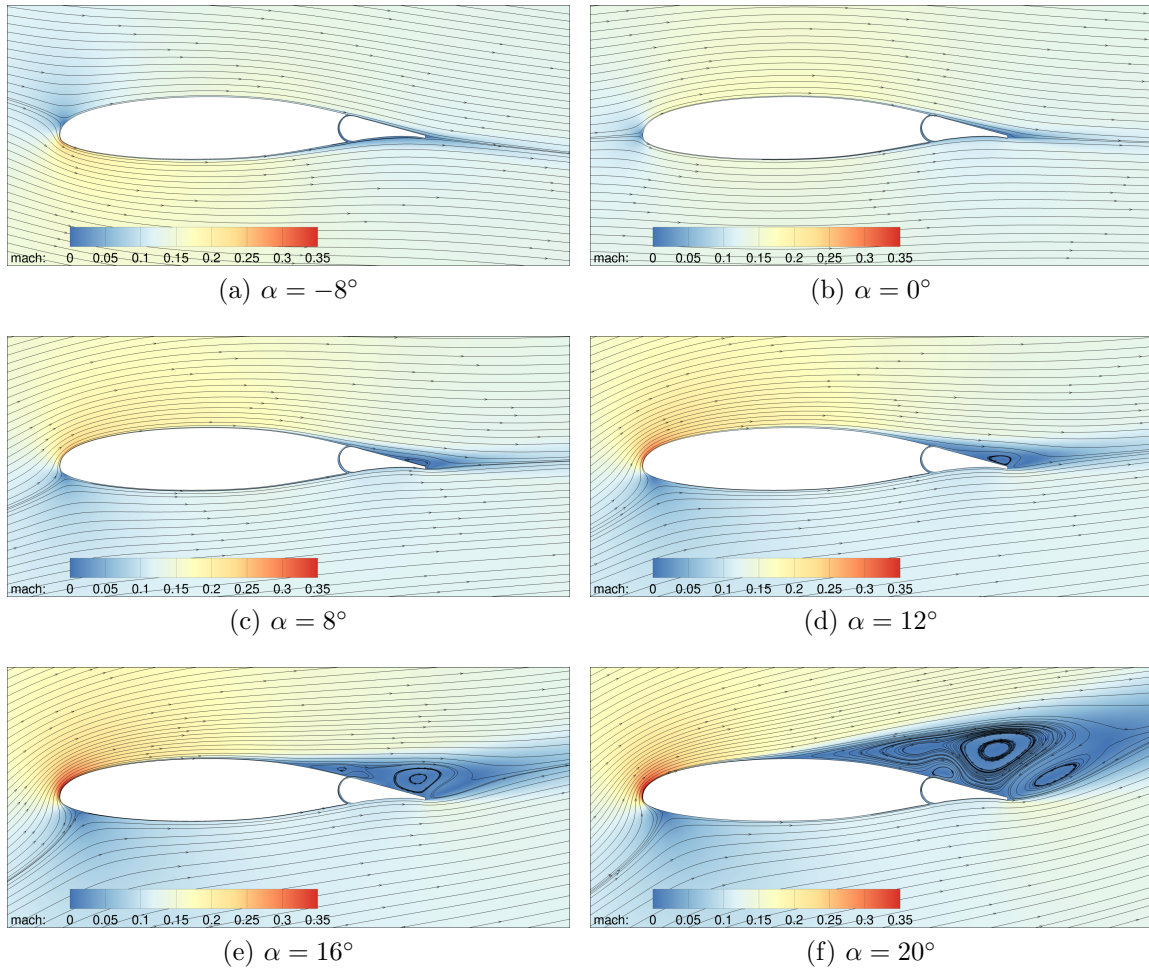


Figure 3.16: GA(W)-1 steady-state flow field Mach number,  $\delta = 0^\circ$

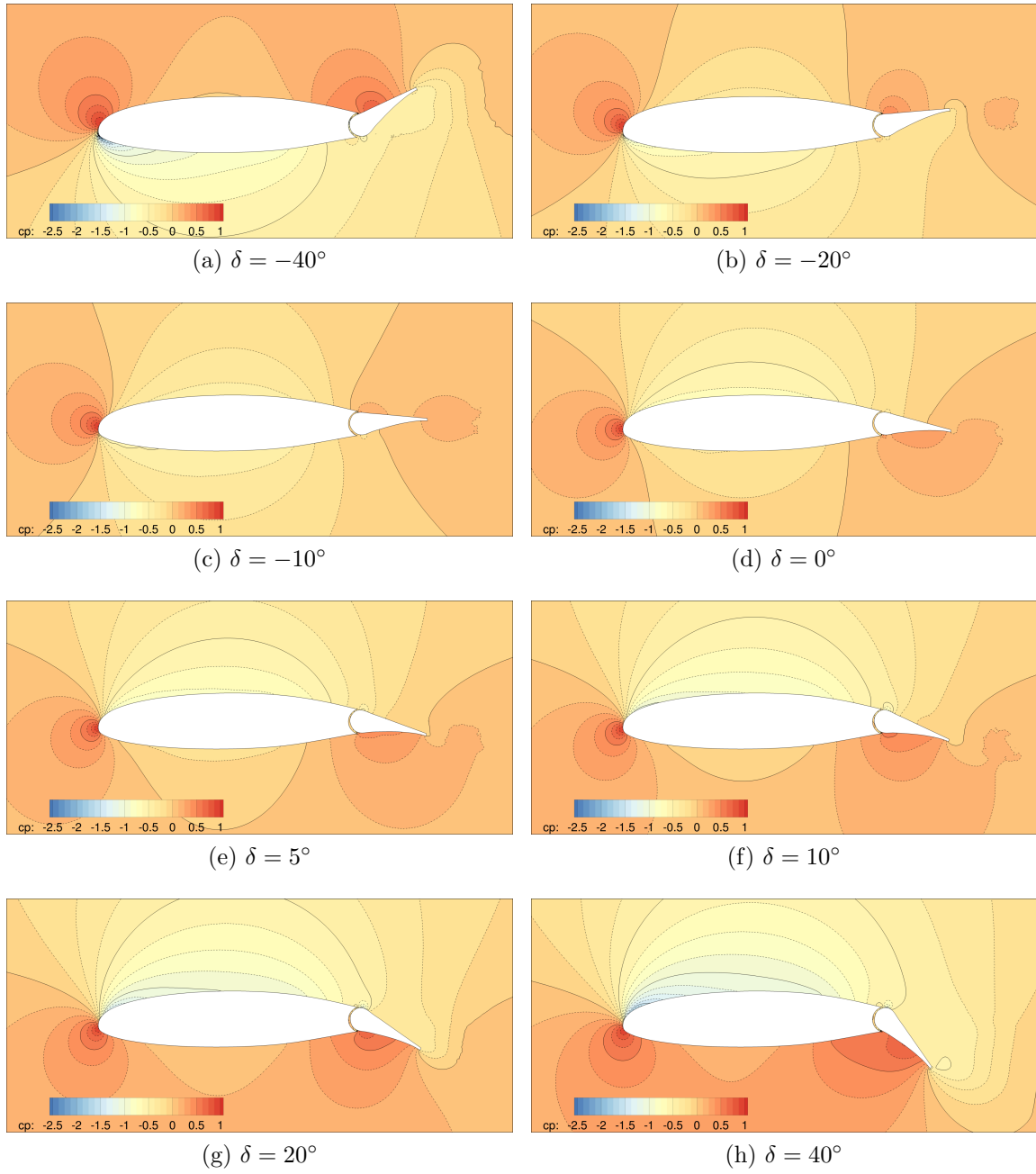


Figure 3.17: GA(W)-1 steady-state pressure coefficient,  $\alpha = 0^\circ$

pressure distribution is fairly uniform in regions of separation, especially on the low-pressure side of the control surface. In all cases, a strong adverse pressure gradient exists near the hinge gap, both on the wing and on the control surface. This adverse pressure gradient is the primary reason for flow instability.

The pressure coefficient on the airfoil surface is shown for two cases in figures 3.18 and 3.19. Due to the age of the reference, experimental data are obtained by digitizing a scanned copy of the original paper report. Some of the pressure coefficient values in the reference figures are impossible to decipher. Those data points were not digitized, and are therefore missing from the pressure coefficient figures in this thesis.

In both cases, the pressure distribution is slightly wavy near the leading edge of the wing. This is a sign that the numerical surface definition is not perfect. Despite best efforts to smooth the surface spline, some slight oscillations evidently remain in the surface definition, causing oscillations in the pressure profile.

In both figures, the pressure coefficient on the high-pressure face of the control surface is captured accurately with the exception of the leading edge. The low-pressure surface is fairly accurate for the zero deflection case, although the suction peak is significantly under-predicted. The  $20^\circ$  deflection case significantly under-predicts the pressure distribution on the low-pressure face of the control surface by about 30%. The suction peak on the leading edge is not accurately computed.

The lift coefficient computed by FUN3D more closely agrees with the reference case than the XFOIL values. Flow separation negatively impacts the computational accuracy, although to a lesser extent than the XFOIL results. FUN3D tends to over-predict the deflection-induced lift for small angles of attack. At post-stall angles of attack, agreement with experimental data is unsurprisingly poor due to the large separation region.

Drag is also predicted accurately for most of the test cases, although there is a tendency to under-predict drag in cases with large amounts of separation, particularly near stall conditions. These results also indicate that there is a tendency to over-predict  $C_{l_{\max}}$ . This

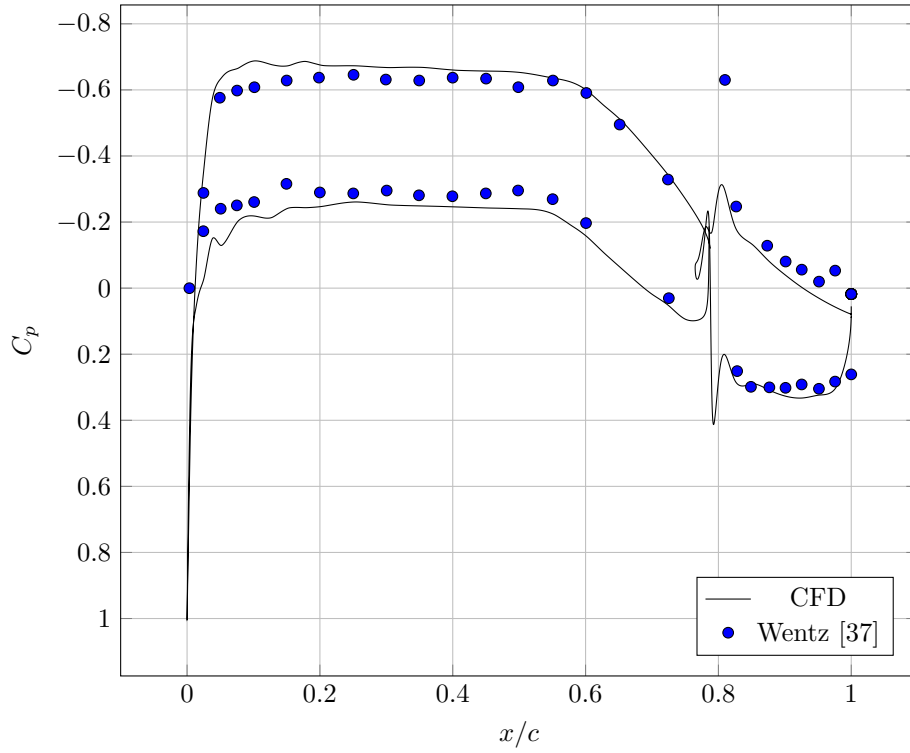


Figure 3.18: GA(W)-1 surface pressure coefficient,  $\alpha = 0^\circ$ ;  $\delta = 0^\circ$

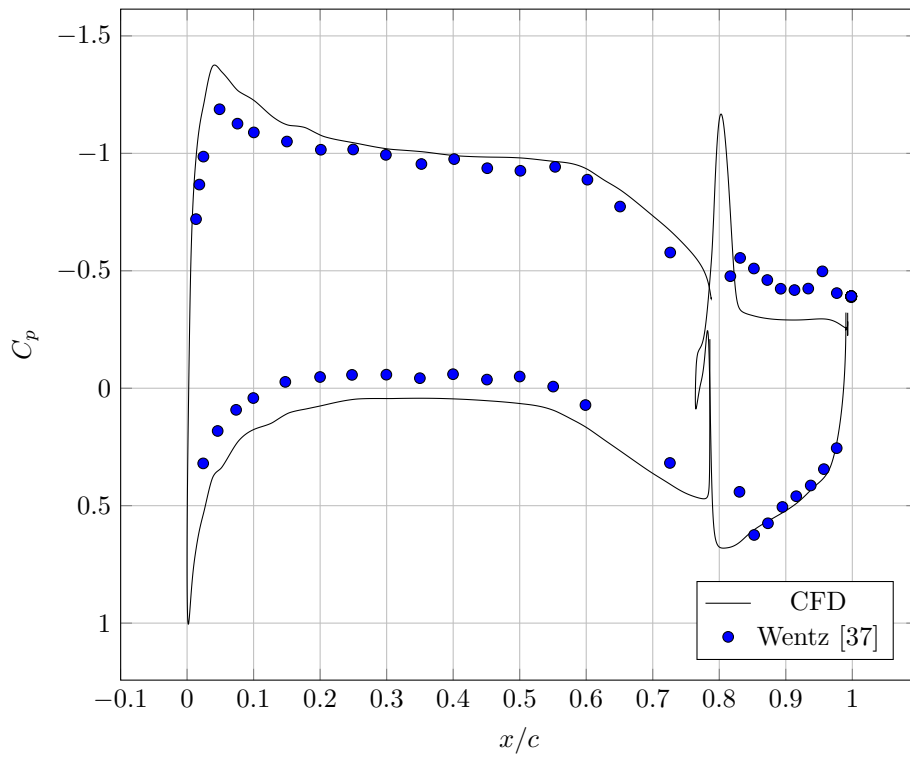


Figure 3.19: GA(W)-1 surface pressure coefficient,  $\alpha = 0^\circ$ ;  $\delta = 20^\circ$

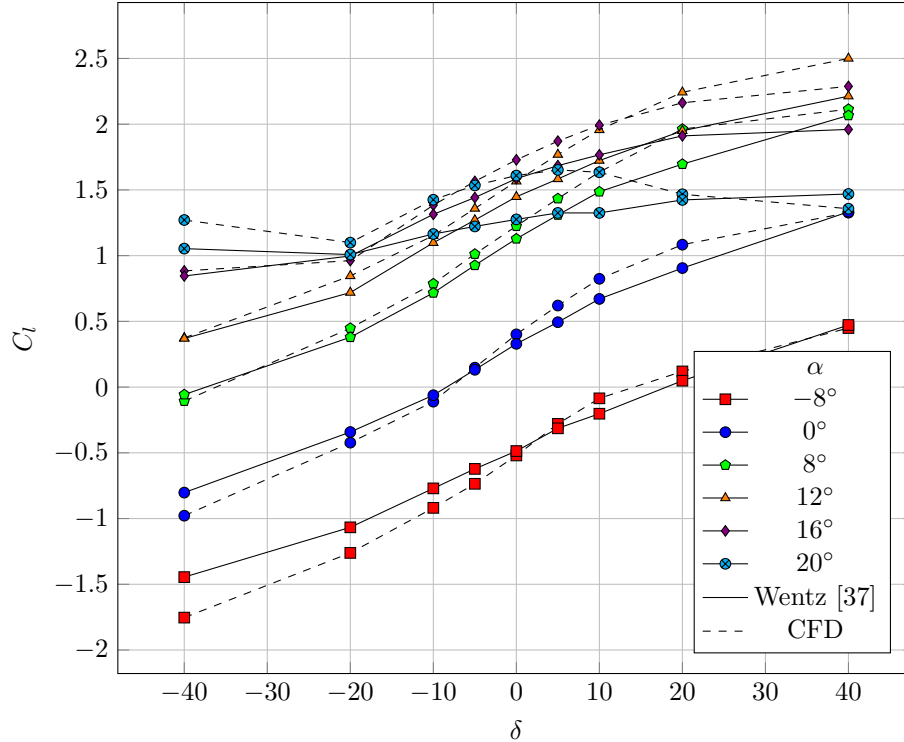


Figure 3.20:  $C_l$  versus  $\delta$ , steady FUN3D.

tendency is likely attributed to the fact that a steady-state simulation is unable capture the inherently unsteady behavior associated with separated flow. The computed pitching moment coefficients also agree with the reference except in cases with large separation regions.

For a relatively simple subsonic, two-dimensional case, the steady-state Navier-Stokes solution gives accurate results, provided configurations with flow separation are avoided. For most control surface configurations in real applications, this limits the analysis to small angles of attack and small deflection angles. Local time-stepping is insufficient to capture the inherent unsteadiness in separated flows with vortex shedding. This is most critical for predicting hinge moments near stall conditions and in configurations with large control surface deflections.

### 3.4.3 Time-Accurate Navier-Stokes Solution

While the steady-state solution gives usable results, there is room for improvement. The steady-state solution performs well in cases with little flow separation. In practical

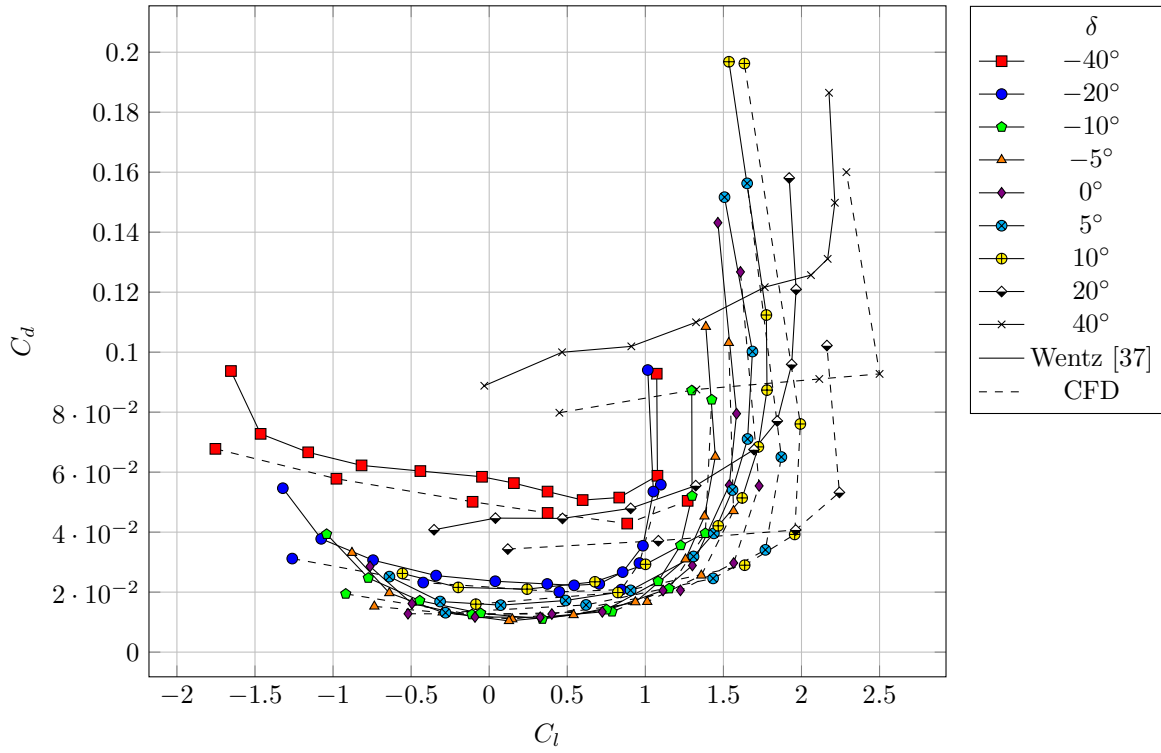


Figure 3.21: Drag polar, steady FUN3D.

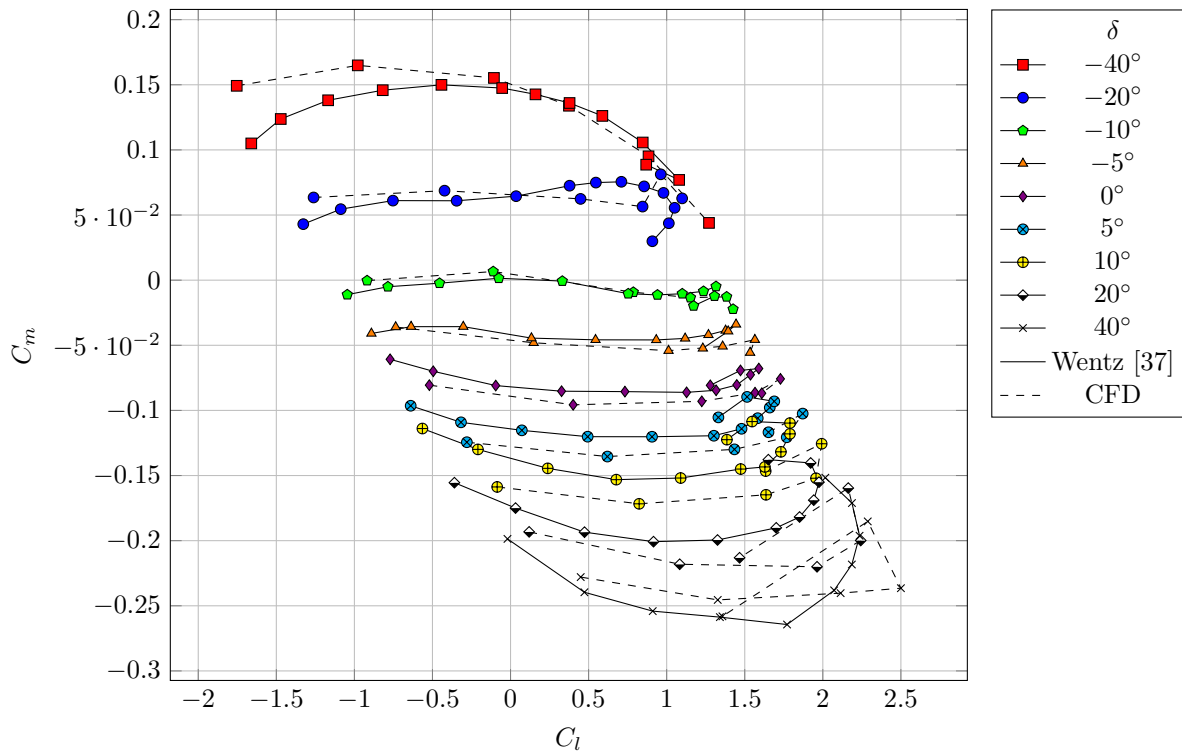


Figure 3.22:  $C_m$  versus  $C_l$ , steady FUN3D.

applications, flow over a deflected control surface is rarely a steady process. In actual aircraft, pilots frequently feel vibrations in the control surfaces when deflected to large angles, which is evidence of separation and vortex shedding.

To capture this unsteady behavior, a steady-state solution is insufficient. A time-accurate solution is required to fully capture the flow physics.

Time is nondimensionalized in FUN3D as

$$t = \frac{t^* a_{\text{ref}}^* L_{\text{ref}}}{L_{\text{ref}}^*}$$

where a star indicates a dimensional quantity. The dimensional characteristic time is

$$t_{\text{chr}}^* = \frac{L_{\text{ref}}^*}{M_{\text{ref}} a_{\text{ref}}^*}$$

The characteristic time is the time in which a particle traveling at the freestream velocity travels a distance equal to the reference length. For the GA(W)-1 reference case, the characteristic time is 0.0142 s. Nondimensionalized, the characteristic time is

$$t_{\text{chr}} = \frac{L_{\text{ref}}}{M_{\text{ref}}}$$

The reference nondimensional characteristic time is 184.62.

A study is required to determine the requisite time step resolution. A test case with  $\alpha = 0^\circ$  and  $\delta = 40^\circ$  is known to have flow separation, so that case is chosen to determine the time step required to capture the unsteady behavior. The solution is restarted from the steady-state solution with a coarse time step until a periodic behavior emerges. A time-averaged value is computed by averaging the hinge moment coefficient over multiple periods, the length of which is determined by finding the local minima in the hinge moment history. The process is then repeated for several increasingly fine time steps, each time restarting from the previous solution. The time-averaged values are provided in Table 3.5, and they

are graphically shown in Figure 3.23.

Table 3.5: GA(W)-1 time-averaged hinge moment coefficients for various nondimensional time steps;  $\alpha = 0^\circ$ ,  $\delta = 40^\circ$

$\Delta t$	$C_h$
0.5	-0.5867
0.3875	-0.6391
0.275	-0.6349
0.1625	-0.6311
0.05	-0.6291

The temporal resolution study shows that a small time step is required in order to resolve the hinge moments. To achieve sufficient temporal resolution, the smallest time step is chosen,  $\Delta t = 0.05$ . This corresponds to 3692.4 temporal iterations per characteristic time. The time-averaged hinge moment coefficient found using this value differs from the next largest time step by only 0.3%. Each temporal iteration then represents  $3.83 \times 10^{-6}$  seconds in real time. For each incremental time step, using five subiterations is found to be sufficient to consistently resolve the mean flow and turbulent residuals to within  $10^{-12}$  and  $10^{-8}$ , respectively.

In early trials, no appreciable difference was observed between steady and unsteady calculations in a large percentage of configurations. It is hypothesized that the solver converges to a steady-state solution to such an extent that perturbations are too small to trigger any weak instabilities. The steady-state solution was therefore artificially perturbed by introducing a  $1^\circ$  angle of attack increase for 1,000 iterations, and thereafter returning to the correct angle of attack for the remainder of the unsteady simulation.

For the angle of attack perturbation, and for 1,000 iterations afterward, the unsteady simulations were run at a coarse time step in order to quickly reduce transients. The coarse time step was chosen to be one order of magnitude larger than the fine time step. The simulation was then run at the fine time step until a convergent behavior appeared. For an

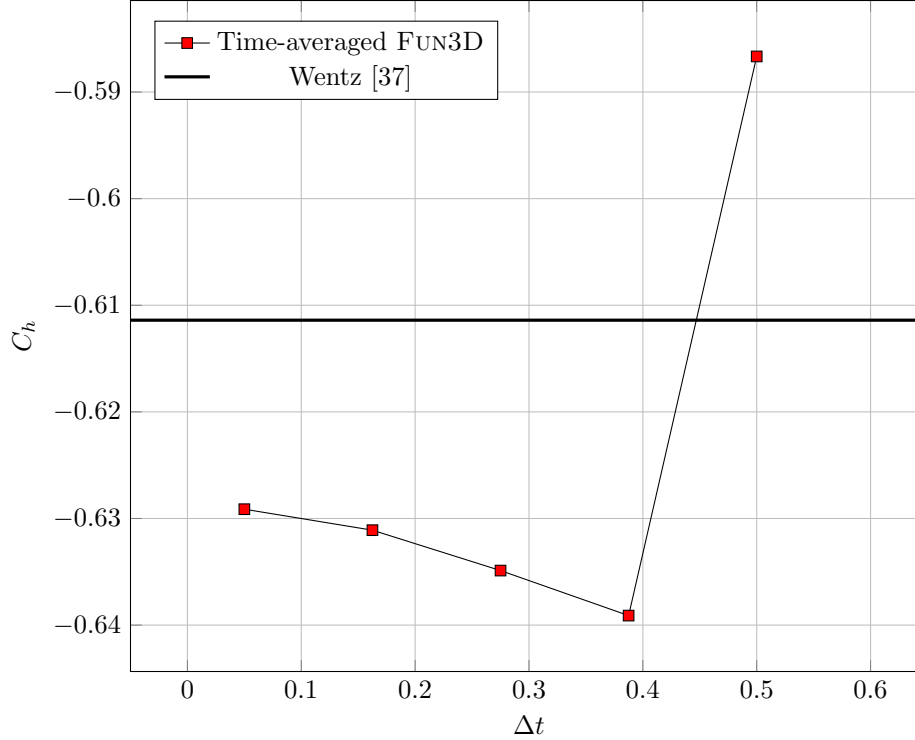


Figure 3.23: GA(W)-1 time-averaged hinge moment coefficients versus nondimensional time step,  $\alpha = 0^\circ$ ,  $\delta = 40^\circ$

unsteady case with separation, hinge moments show some periodic behavior. The solution was considered to be converged when consecutive periods are consistent.

However, even the angle of attack perturbation did not excite the expected vortex shedding in most cases. Through trial and error, it is determined that the most reliable method of triggering unsteady behavior in the time-accurate solution is to initialize the entire domain with the freestream velocity. Initializing the flow with the freestream velocity immediately triggers unsteady behavior and actually yields the periodic behavior much sooner than initializing from the steady-state solution. Restarting from the steady-state solution, the final periodic behavior is reached within about 145,000 iterations. Initializing from freestream conditions, the solution requires only 4,000 iterations to reach the periodic behavior. To reduce the initial transient behavior faster, simulations are started with a larger  $\Delta t$  of 0.5. The fine time step is then used to capture the periodic unsteady flow.

Figure 3.24 shows the complete time history of the unsteady FUN3D solution for  $\alpha = 0^\circ$

and  $\delta = 40^\circ$ . The change from the coarse time step to the fine time step occurs at iteration 5,000, which corresponds to 0.192 seconds. A detailed view of the final 0.1 seconds of the solution is shown in Figure 3.25. At this point in the solution, the flow is purely periodic with a period of 0.00927 seconds, or a frequency of 107.8 Hz. A time-averaged value is calculated by averaging the values over several trough-to-trough periods. The time-averaged hinge moment coefficient is  $-0.6348$ . This is within 3.8% of the reference value, which is a substantial improvement over the 18.8% error of the steady-state solution for the same configuration.

An additional benefit of a time-accurate solution over a steady-state solution is the ability to capture maximum hinge moments. This is important because peak loads constrain the structural design of an aircraft. In the case of  $\alpha = 0^\circ$  and  $\delta = 40^\circ$ , the hinge moment at its largest magnitude in the periodic behavior is 12% greater than the time-averaged value.

Similar improvements are seen for the case of  $\alpha = 20^\circ$  and  $\delta = 20^\circ$ . Figure 3.26 shows that the solution took much longer to resolve the transient behavior. As before, the coarse time step was replaced with the fine time step at iteration 5,000, or 0.192 seconds, although the transition is not obvious in the figure. This case requires nearly one million iterations to reach a pure periodic behavior, whereas the  $\alpha = 0^\circ$ ,  $\delta = 40^\circ$  case required only about 50,000 iterations. The final 0.1 seconds of the simulation is shown in Figure 3.27. The periodic flow has a period of 0.0213 seconds, or a frequency of 46.97 Hz. The time-averaged value is computed over several trough-to-trough periods. The time-averaged hinge moment coefficient is  $-0.5432$ , which differs from the reference by only 0.018%. This is excellent agreement with the experimental data.

Figure 3.28 depicts the flow field Mach number at various points during one period of the shedding behavior. The pressure coefficient for the same period is shown in Figure 3.29. The pressure coefficient contours clearly show the variations on the control surface that manifest as hinge moment fluctuations.

One point of interest is the difference between the time-averaged values found in the case

Table 3.6: Comparison of select steady and unsteady FUN3D GA(W)-1 hinge moments

$\alpha$	$\delta$	Reference	Steady		Unsteady	
		$C_h$	$C_h$	% Error	$C_h$	% Error
0°	40°	-0.6114	-0.4963	18.8%	-0.6348	3.8%
20°	20°	-0.5431	-0.4752	12.5%	-0.5432	0.018%

of  $\alpha = 0^\circ$  and  $\delta = 40^\circ$ . The temporal resolution study produced time-averaged hinge moment that differs from the value found in the final study. Both cases are time-averaged using an identical process, and both cases use an identical time step and an identical mesh. This implies that the initial condition of the simulation affects the long-term periodic behavior predicted by the simulation.

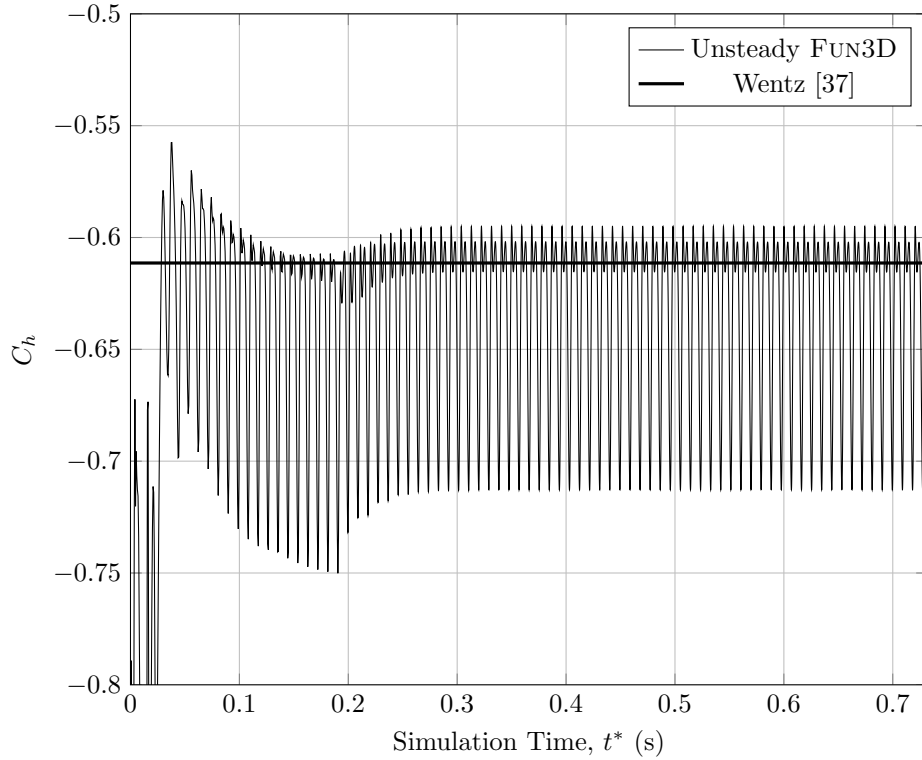


Figure 3.24: Unsteady GA(W)-1 hinge moment coefficient history,  $\alpha = 0^\circ$ ;  $\delta = 40^\circ$

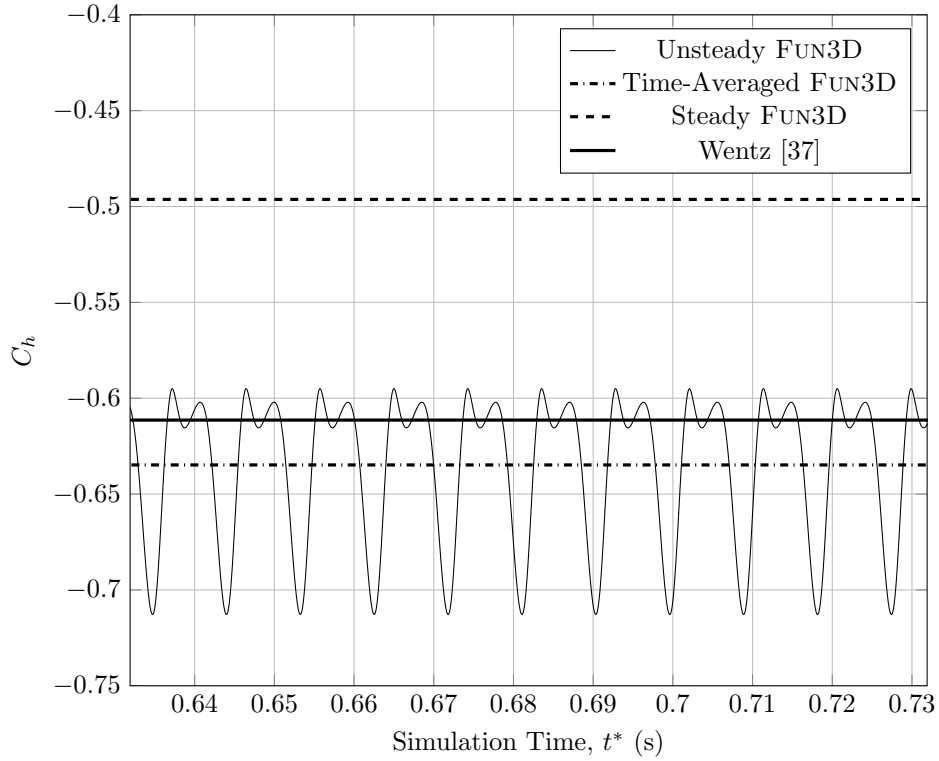


Figure 3.25: Periodic detail of unsteady GA(W)-1 hinge moment history,  $\alpha = 0^\circ$ ;  $\delta = 40^\circ$

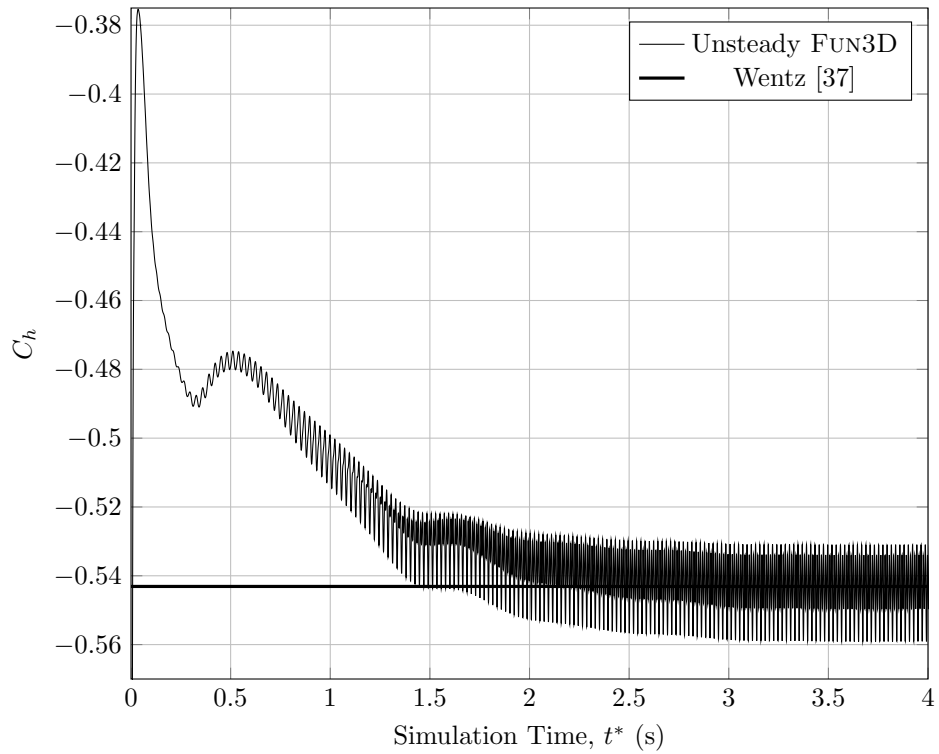


Figure 3.26: Unsteady GA(W)-1 hinge moment coefficient history,  $\alpha = 20^\circ$ ;  $\delta = 20^\circ$

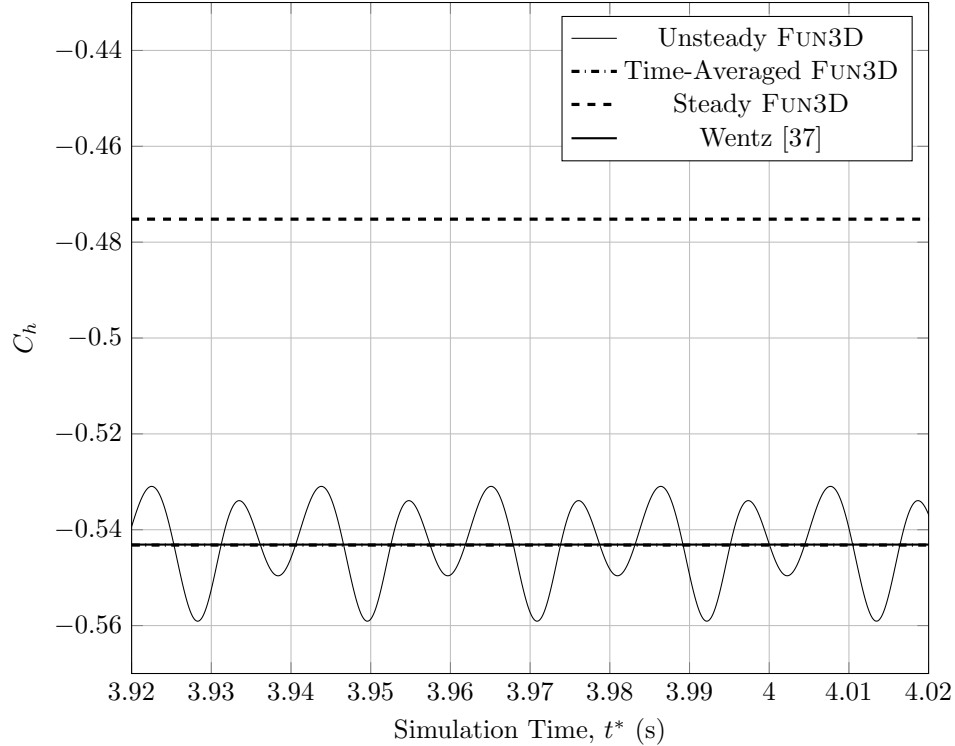


Figure 3.27: Periodic detail of unsteady GA(W)-1 hinge moment history,  $\alpha = 20^\circ$ ;  $\delta = 20^\circ$

### 3.5 Discussion of Results

A comparison of hinge moments found using each solution method in the GA(W)-1 study are provided in Tables 3.7 – 3.12.

The accuracy of hinge moment predictions depends primarily on the ability to capture the physics of separated flow. Solution methods which are not designed for separated flows, such as XFOIL and the empirical relations in the Datcom, are not well-suited to predict hinge moments for configurations with large deflections or large angles of attack. A steady-state Navier-Stokes CFD solution is suitable for most cases, although errors greater than 20% can be expected for cases with large separation regions.

The most reliable method of predicting hinge moments for this case is a time-accurate Navier-Stokes solution. Time-accurate simulations provide a significant improvement in hinge moment prediction over the steady-state solution. The time-accurate solutions require a very fine time step to accurately capture the unsteadiness associated with control surface

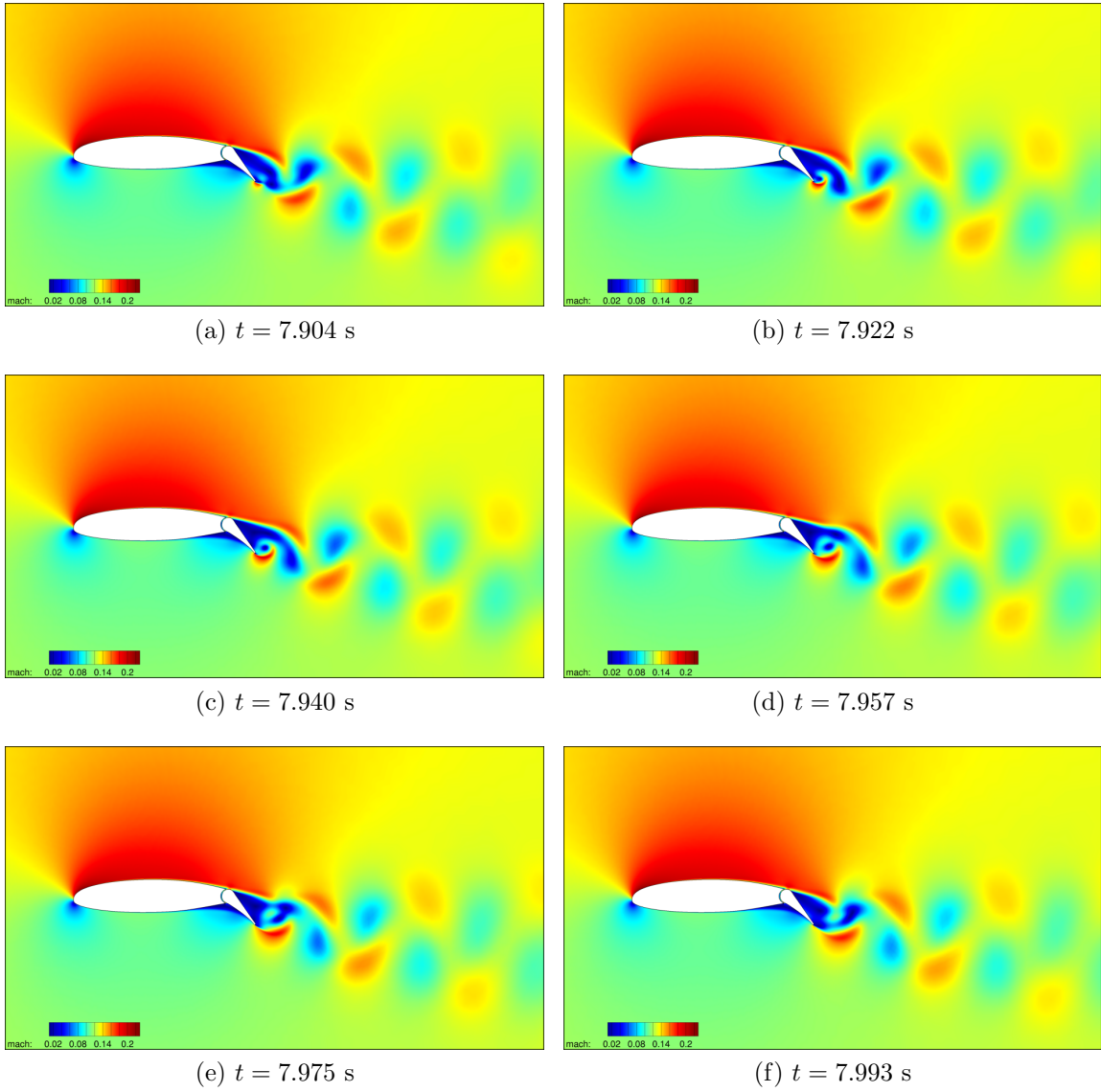


Figure 3.28: GA(W)-1 unsteady flow field Mach number,  $\alpha = 0^\circ$ ,  $\delta = 40^\circ$

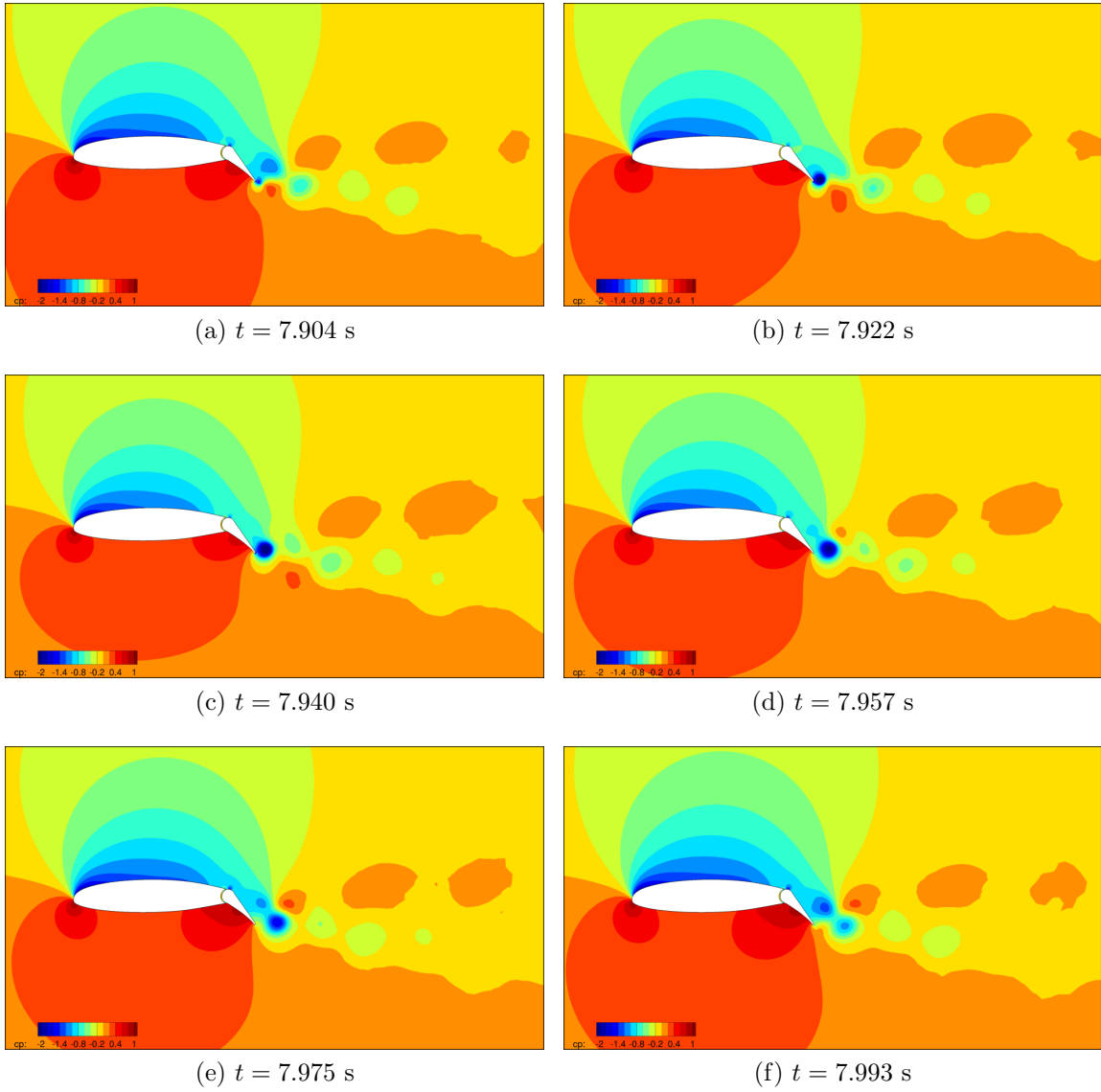


Figure 3.29: GA(W)-1 unsteady flow field pressure coefficient contours,  $\alpha = 0^\circ$ ,  $\delta = 40^\circ$

problems. As a result, they are also much more computationally expensive than steady-state solutions.

Table 3.7: Comparison of GA(W)-1 hinge moment results,  $\alpha = -8^\circ$

$\delta$	Reference	Datcom + $C_{h_0}$	XFOIL	Steady FUN3D
-40	0.3295	0.4781	0.3009	0.3391
-20	0.1631	0.2063	0.1399	0.1658
-10	0.0540	0.0704	0.0413	0.0667
-5	0.0107	0.0024	-0.0170	0.0100
0	-0.0655	-0.0655	-0.0800	-0.0707
5	-0.1437	-0.1335	-0.1484	-0.1274
10	-0.1916	-0.2014	-0.2192	-0.1787
20	-0.3215	-0.3374	-0.2839	-0.2952
40	-0.5360	-0.6092	-0.3936	-0.4354

Table 3.8: Comparison of GA(W)-1 hinge moment results,  $\alpha = 0^\circ$

$\delta$	Reference	Datcom + $C_{h_0}$	XFOIL	Steady FUN3D
-40	0.3653	0.3885	0.2892	0.3312
-20	0.1631	0.1167	0.1100	0.1442
-10	0.0106	-0.0192	-0.0410	0.0245
-5	-0.0949	-0.0871	-0.1161	-0.0840
0	-0.1551	-0.1551	-0.1859	-0.1450
5	-0.2106	-0.2231	-0.2476	-0.1930
10	-0.2652	-0.2910	-0.2623	-0.2392
20	-0.4007	-0.4269	-0.3334	-0.3423
40	-0.6114	-0.6988	-0.4431	-0.4963

Table 3.9: Comparison of GA(W)-1 hinge moment results,  $\alpha = 8^\circ$

$\delta$	Reference	Datcom + $C_{h_0}$	XFOIL	Steady FUN3D
-40	0.3295	0.3348	0.2892	0.2891
-20	0.1358	0.0630	0.0653	0.1058
-10	-0.0894	-0.0729	-0.1050	-0.0705
-5	-0.1637	-0.1409	-0.1550	-0.1420
0	-0.2088	-0.2088	-0.1855	-0.1892
5	-0.2606	-0.2768	-0.2284	-0.2284
10	-0.3142	-0.3447	-0.2710	-0.2643
20	-0.4130	-0.4807	-0.3450	-0.3331
40	-0.6124	-0.7525	-0.4569	-0.4919

Table 3.10: Comparison of GA(W)-1 hinge moment results,  $\alpha = 12^\circ$

$\delta$	Reference	Datcom + $C_{h_0}$	XFOIL	Steady FUN3D
-40	0.2720	0.2905	0.2291	0.2329
-20	0.0443	0.0187	0.0875	0.0642
-10	-0.1667	-0.1173	-0.1208	-0.1312
-5	-0.2156	-0.1852	-0.1644	-0.1786
0	-0.2532	-0.2532	-0.2127	-0.2141
5	-0.2964	-0.3211	-0.2557	-0.2470
10	-0.3416	-0.3891	-0.2951	-0.2797
20	-0.4290	-0.5250	-0.3654	-0.3459
40	-0.5709	-0.7968	-0.4218	-0.4686

Table 3.11: Comparison of GA(W)-1 hinge moment results,  $\alpha = 16^\circ$

$\delta$	Reference	Datcom + $C_{h_0}$	XFOIL	Steady FUN3D
-40	0.1400	0.2282	0.1438	0.1223
-20	-0.0887	-0.0436	0.0361	0.0334
-10	-0.2308	-0.1795	-0.1627	-0.1918
-5	-0.2712	-0.2475	-0.2105	-0.2275
0	-0.3154	-0.3154	-0.2523	-0.2626
5	-0.3521	-0.3834	-0.2909	-0.2982
10	-0.3859	-0.4513	-0.3273	-0.3343
20	-0.4780	-0.5872	-0.3950	-0.4043
40	-0.6152	-0.8591	-0.5158	-0.5227

Table 3.12: Comparison of GA(W)-1 hinge moment results,  $\alpha = 20^\circ$

$\delta$	Reference	Datcom + $C_{h_0}$	XFOIL	Steady FUN3D
-40	-0.0222	0.1689	0.0347	-0.0582
-20	-0.1820	-0.1030	-0.0226	-0.0884
-10	-0.3034	-0.2389	-0.2045	-0.2355
-5	-0.3429	-0.3068	-0.2496	-0.2731
0	-0.3748	-0.3748	-0.2915	-0.3126
5	-0.4039	-0.4427	-0.3286	-0.3531
10	-0.4575	-0.5107	-0.3667	-0.3937
20	-0.5431	-0.6466	-0.4431	-0.4752
40	-0.7029	-0.9184	-0.5825	-0.6106

**CHAPTER 4**

**INVESTIGATION OF A 45-DEGREE SWEEP NACA 0012 HORIZONTAL STABILIZER WITH A 25% FULL-SPAN ELEVATOR**

**4.1 Geometry Description**

The test case presented in the following sections is a three-dimensional horizontal stabilizer with a 25% elevator. A complete description of the geometry and experimental results are presented by Johnson and Thompson [39]. A semispan horizontal stabilizer model is used in this study for a three-dimensional test case.

Table 4.1: NACA 0012 swept wing reference quantities

Quantity	Symbol	Value
Section chord*	$c$	15 in
Wing semispan	$b/2$	31.53 in
Wing sweep	$\Lambda$	45°
Section % thickness	$t/c$	0.12
Control surface % chord	$c_f/c$	0.25
Hinge axis x-coordinate	$x_h/c$	0.75
Hinge axis z-coordinate	$z_h/c$	0.0
Reynolds number	Re	$5.52 \times 10^6$
Mach number	$M$	0.5

\* measured normal to the leading edge

The model has an NACA 0012 airfoil section of uniform chord of 15 in perpendicular to the leading edge, with 45° of sweep. A detailed schematic of the reference geometry is shown in detail in Figures 4.1 and 4.2. The horn balance shown at the tip in Figure 4.1 is not

present on the configuration modeled in this study. The plain elevator model pictured in Figure 4.2 is used. The model is equipped with a 25% unsealed plain elevator with a leading edge radius and a 1/32-inch hinge gap. The elevator consists of two spanwise segments separated by a 1/16-inch gap.

The model was tested in the Langley high-speed 7- by 10-foot tunnel in 1950. Elevator hinge moments were measured using electrical strain gauges within the stabilizer. Forces and moments on the model were measured using a force balance. Data was collected for several deflection angles and angles of attack. Johnson and Thompson also conducted wind tunnel tests for each configuration at Mach numbers ranging from 0.5 to 0.89. The Reynolds number for the test varied with Mach number. The correlation between test Mach number and Reynolds number is shown in Figure 4.3. This study investigates only the Mach 0.5 case, which has a corresponding Reynolds number of  $5.52 \times 10^6$ .

## 4.2 Mesh Generation

The mesh is constructed using the techniques described in §2.2.4. Two different meshes are compared in this analysis, one with a manually-refined wake region and one without. The surface mesh on the viscous wall boundaries are identical between the two meshes.

The farfield is constructed as a hemisphere with radius equal to 50 chords as measured in the streamwise direction. A spacing constraint of 0.01 inches is applied to most of the surface mesh boundaries. A viscous wall spacing of  $0.5 \times 10^{-6}$  inches is applied normal to all viscous wall boundaries.

The original CFD mesh is shown in Figure 4.4. The elevator is divided into two halves, exactly mimicking the reference model. In order to capture the viscous boundary layer in the  $\frac{1}{16}$  in gap between the two halves, the normal grid spacing must be approximately the same as elsewhere in the geometry. Issues arise during mesh generation in regions of the mesh where small elements are spatially close to large elements. To alleviate this issue at the center of the wing section trailing edge, the wing is constructed such that a strip of small elements is

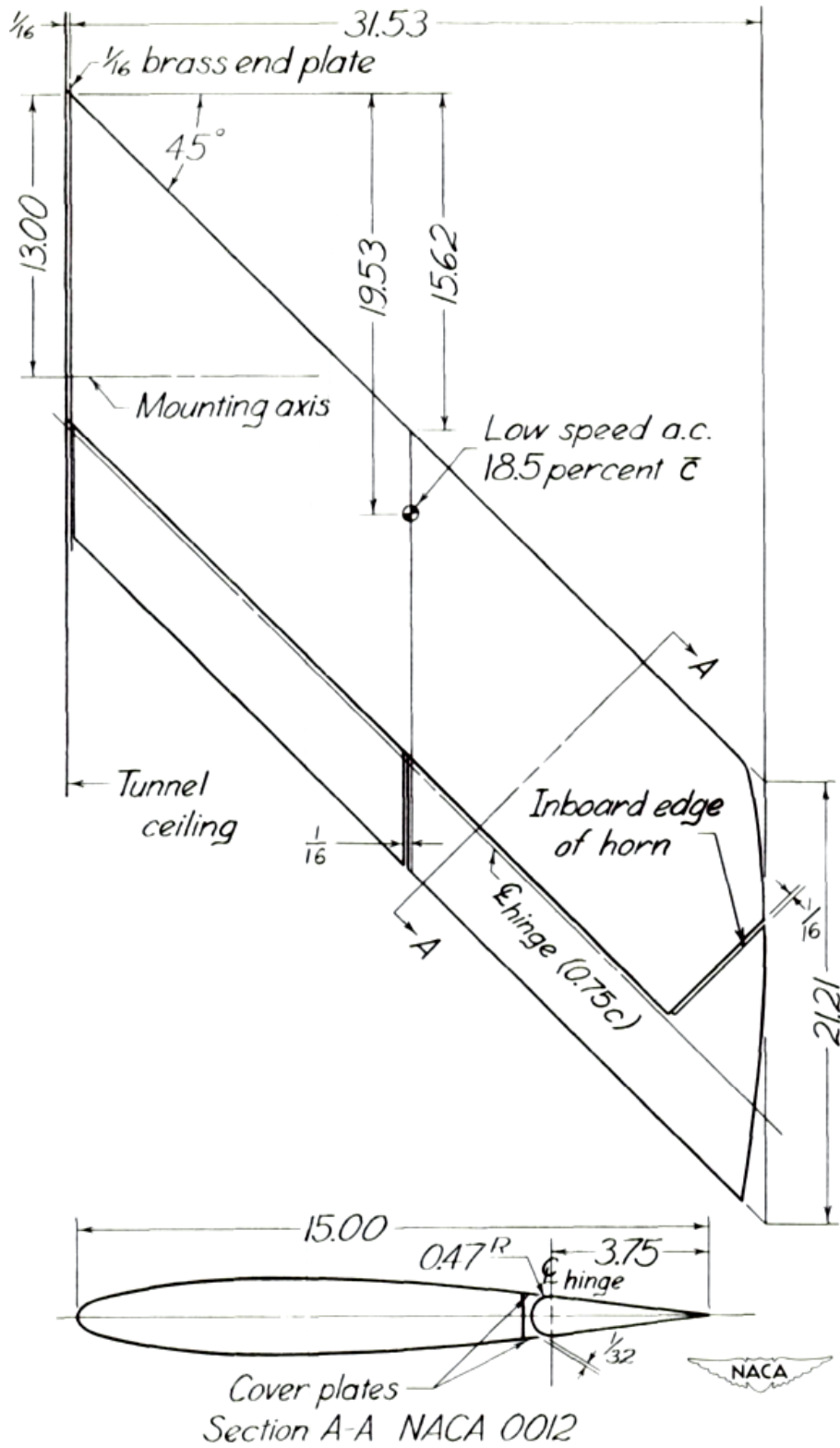


Figure 4.1: NACA 0012 wing reference geometry planform and airfoil section [39].

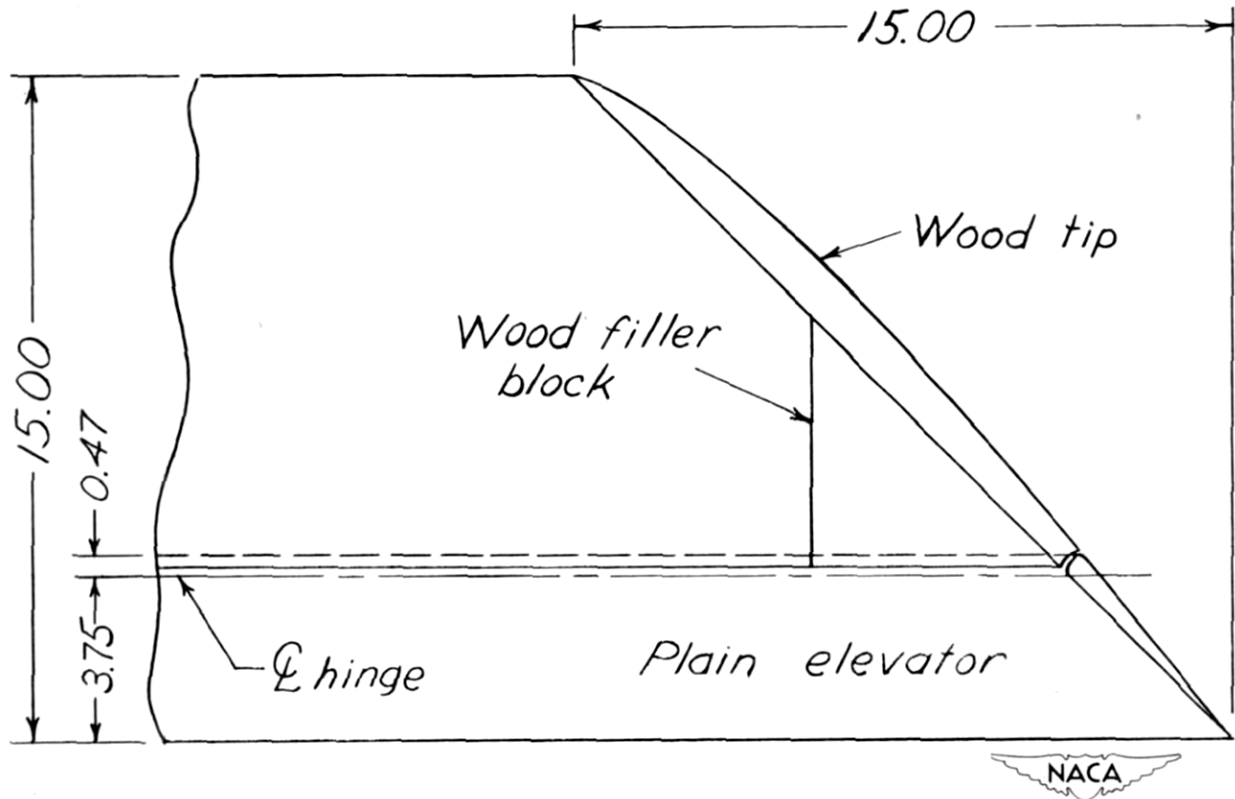


Figure 4.2: NACA 0012 wing reference geometry plain elevator detail [39].

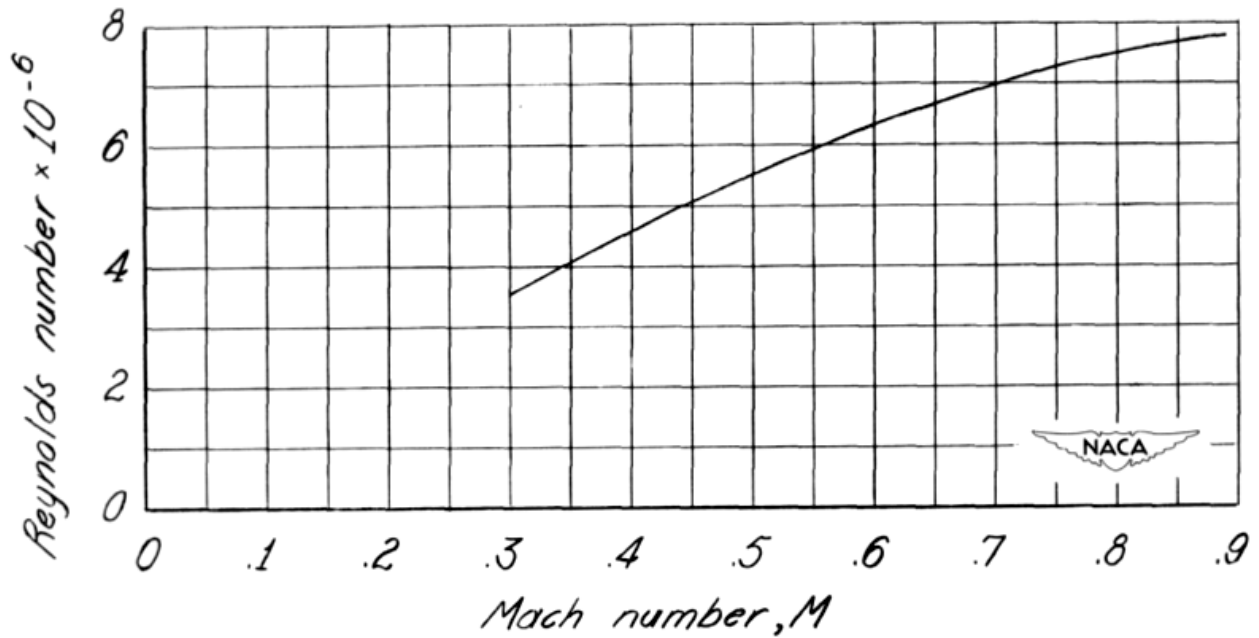


Figure 4.3: NACA 0012 wing reference Reynolds number variation with Mach number [39].

aligned with the gap between the elevator halves. This ensures that volumetric elements are similarly sized to their neighbors in that region. The mesh could be constructed such that the mesh becomes more coarse locally in the span-wise direction toward the leading edge. However, personal experience shows that this is difficult to do well, and the time required to do so outweighs the benefit of a slight reduction in solution time. Each complete mixed-element volumetric mesh contains about 13.9 million grid nodes and 33.9 million total finite volume elements, with just over 536,000 surface elements.

Often, the solution accuracy depends on the mesh having sufficiently many elements in a wake aft of the wing. This is particularly important for drag prediction. A second mesh is therefore created with a manually-refined wake. This type of refinement is simply a method of introducing a region of small elements that can more accurately capture the wake, typically constructed by growing elements from a planar baffle surface. The refined wake constructed in this study is constructed by creating a planar surface measuring one chord length in the streamwise direction, and wide enough to span the entire wing. It is positioned such that the wake baffle surface is a parallelogram with two of its edges parallel with the swept wing and the other two aligned with the streamwise direction. Figure 4.5 shows the details of the mesh with the refined wake. The complete mixed-element volumetric mesh with a refined wake contains approximately 10.1 million nodes and 25.9 million total finite volume elements. The mesh topology on the wing and control surfaces are identical to the base mesh.

Constructing a mesh with a baffle wake is difficult. One primary source of difficulty is the nature of using traditional mesh generation software to construct a mesh of this type. The baffle typically cannot be placed directly adjacent to the geometry due to topology interference with the viscous wall elements. However, if the baffle is placed too far away from the geometry, large elements form in the gap. The ideal spacing is subjective, and it can be difficult to find a spacing that works for a given geometry.

To further complicate matters, the downwash that exists on any lifting surface creates

a wake that is inherently nonplanar. Flow field velocity information must be known at the time of mesh generation in order to accurately capture the shape of the wake. The most straight-forward solution to this issue is to refine the mesh globally, increasing the cell count in some or all regions of the mesh. However, the major disadvantage to global refinement is the increased computational cost. Globally refining the mesh by some factor  $N$  will increase the node count of a 2D mesh by a factor on the order of  $N^2$ , and the node count of a 3D mesh will increase on the order of  $N^3$ .

In order to achieve the most accurate solution within a reasonable amount of time, the mesh must contain many elements in regions where gradients are largest, and fewer elements where permissible. With some practice, an engineer can become skilled at guessing where additional elements are needed, but even the most experienced CFD users will find that the final solution reveals regions in the mesh that may need additional refinement.

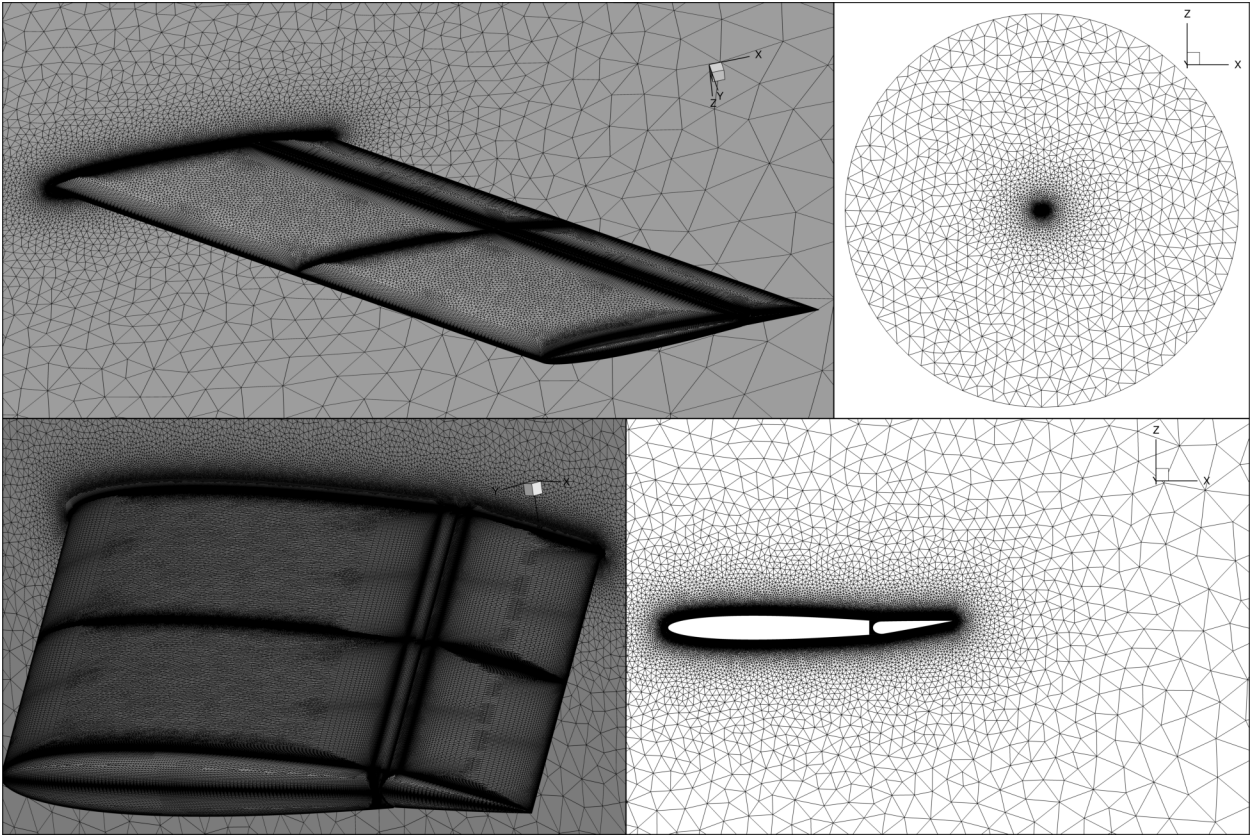


Figure 4.4: NACA 0012 wing mesh

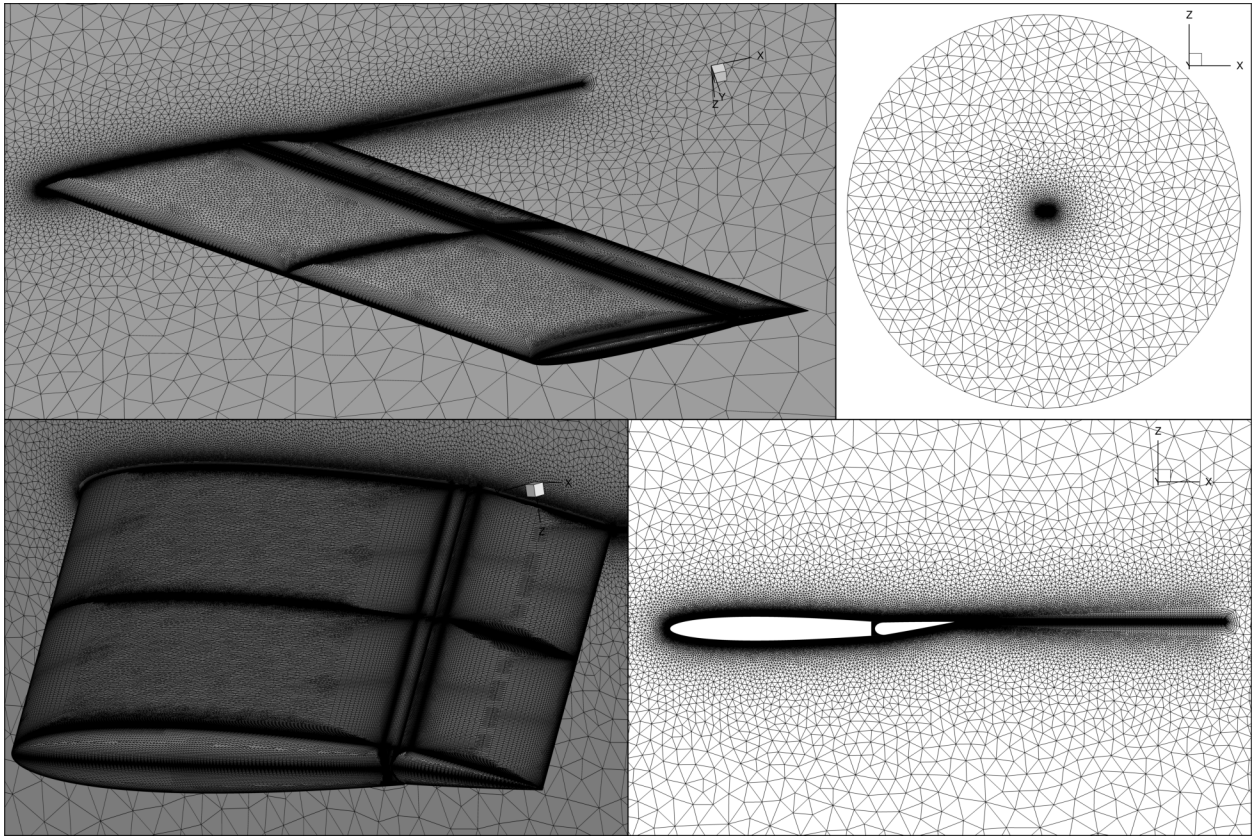


Figure 4.5: NACA 0012 wing mesh with refined baffle wake

### 4.3 Steady-State Solution without Refined Wake

A steady-state solution is found using FUN3D for the mesh without a refined wake. The reference case chosen for this study is a set of runs at a Mach number of 0.5 and a Reynolds number of  $5.52 \times 10^6$ . Johnson and Thompson [39] report values for this case at angles of attack and deflection angles

$$\alpha \in \{-8^\circ, -6^\circ, -4^\circ, -2^\circ, 0^\circ, 2^\circ, 4^\circ, 6^\circ, 8^\circ\}$$
$$\delta \in \{0^\circ, -1.7^\circ, -3.7^\circ, -7.8^\circ\}$$

Johnson and Thompson applied a tunnel correction to the angle of attack and drag coefficient. Corrected angle of attack values are used in the present CFD study. All simulations of this geometry are run on 176 cores across 11 Dell PowerEdge M620 nodes on the UAHPC cluster. This is the entirety of the computing power available to the author at the time of writing this thesis.

Figure 4.6 shows the hinge moments computed by FUN3D versus angle of attack for each deflection angle, using the original mesh with no refined wake. The hinge moments predicted by a steady-state solution in FUN3D are accurate for low deflection angles across the angle of attack range. The hinge moment error increases with deflection angle, and at  $\delta = -7.8^\circ$ , the hinge moments do not agree at all with the reference, with errors on the order of 35%. Given the relatively high Mach number, it is not surprising that larger deflection angles give rise to such inaccuracies.

Lift is predicted with reasonable accuracy across all angles of attack for low deflections. The lift curve slope,  $C_{l_\alpha}$ , is accurate for all deflection angles, but an offset is present in all cases. As with hinge moments, the lift coefficient error increases with deflection angle.

Drag predictions are quite accurate across all angles of attack, and for all deflection angles except  $\delta = -7.8^\circ$ . Many factors can attribute to an inaccurate drag prediction. The solution tends to over-predict drag for angles of attack that cause the control surfaces to

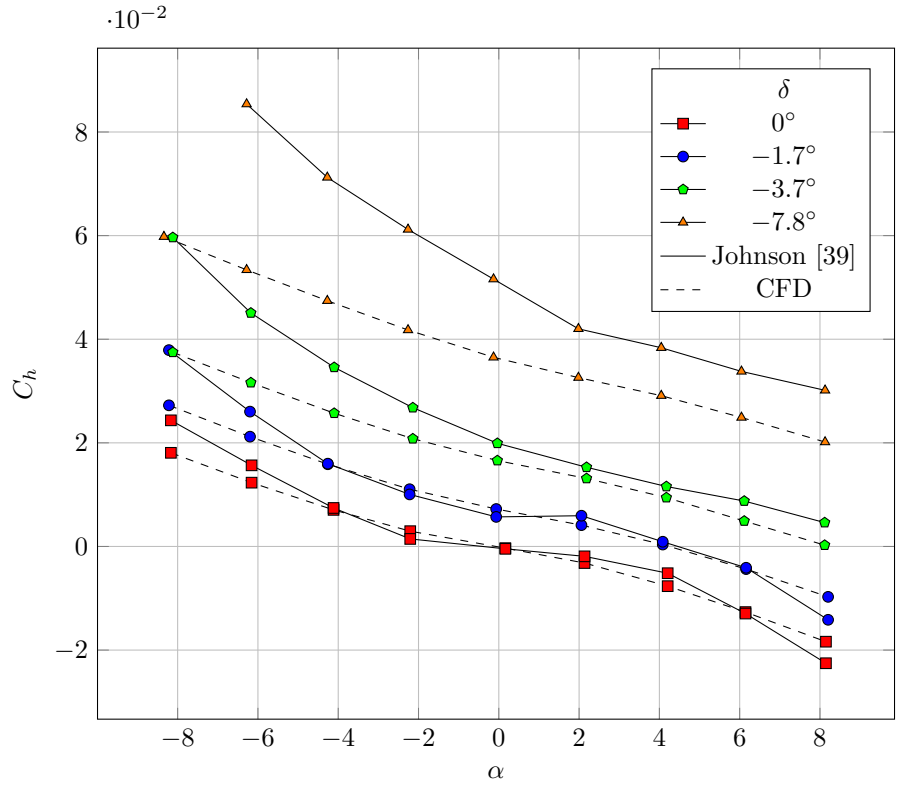


Figure 4.6: NACA 0012 wing hinge moments, without refined wake

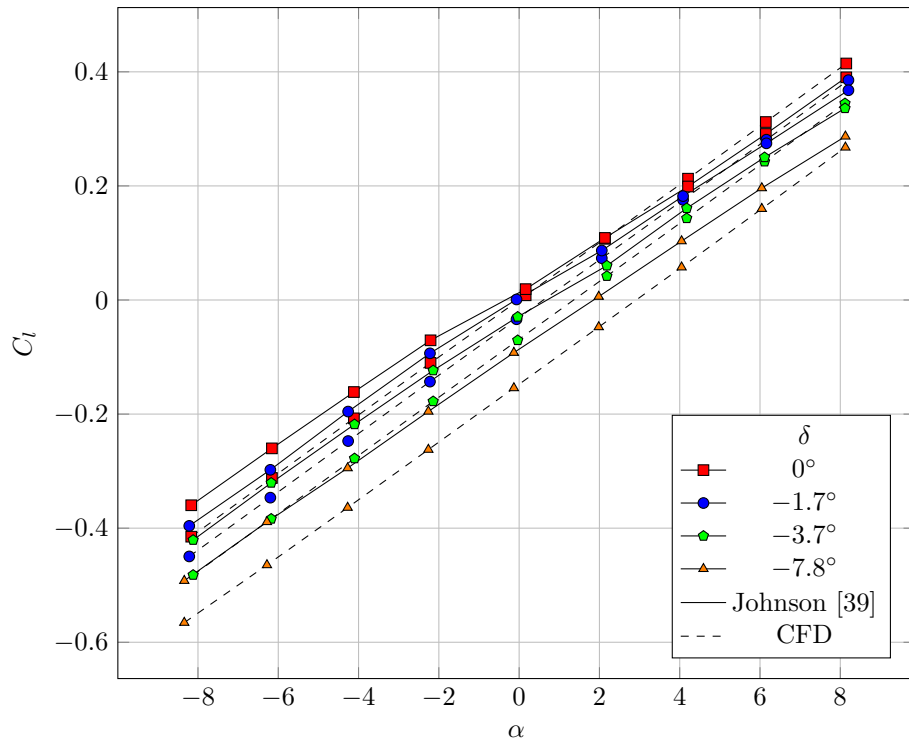


Figure 4.7: NACA 0012 wing lift, without refined wake

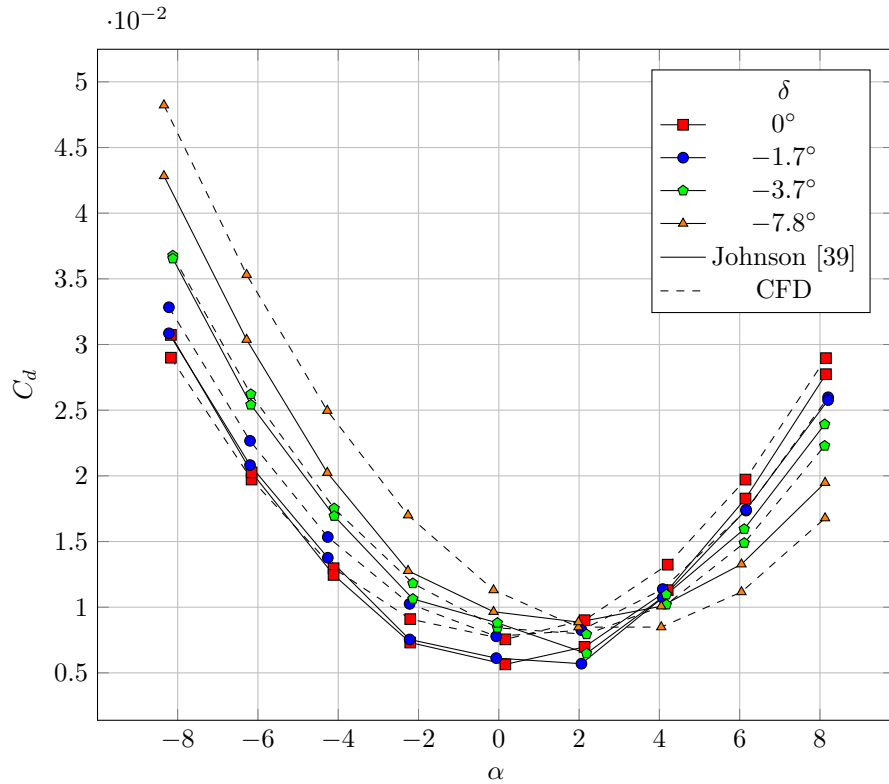


Figure 4.8: NACA 0012 wing drag, without refined wake

see an increase in apparent angle, and it under-predicts the drag when the angle of attack causes a reduction in apparent angle for the control surface. This is an indication that flow separation is a major factor in the drag contribution.

Figures 4.9 – 4.11 show the pressure distribution on the low-pressure surface of the horizontal stabilizer. The effect of the tip vortex is visible as a local region of low pressure on the surface. Increasing either the deflection angle or the angle of attack results in a stronger tip vortex, causing a local change in the pressure distribution on the outboard surface. This also adds to the instability of the flow, which is an indication that a time-accurate solution may be beneficial.

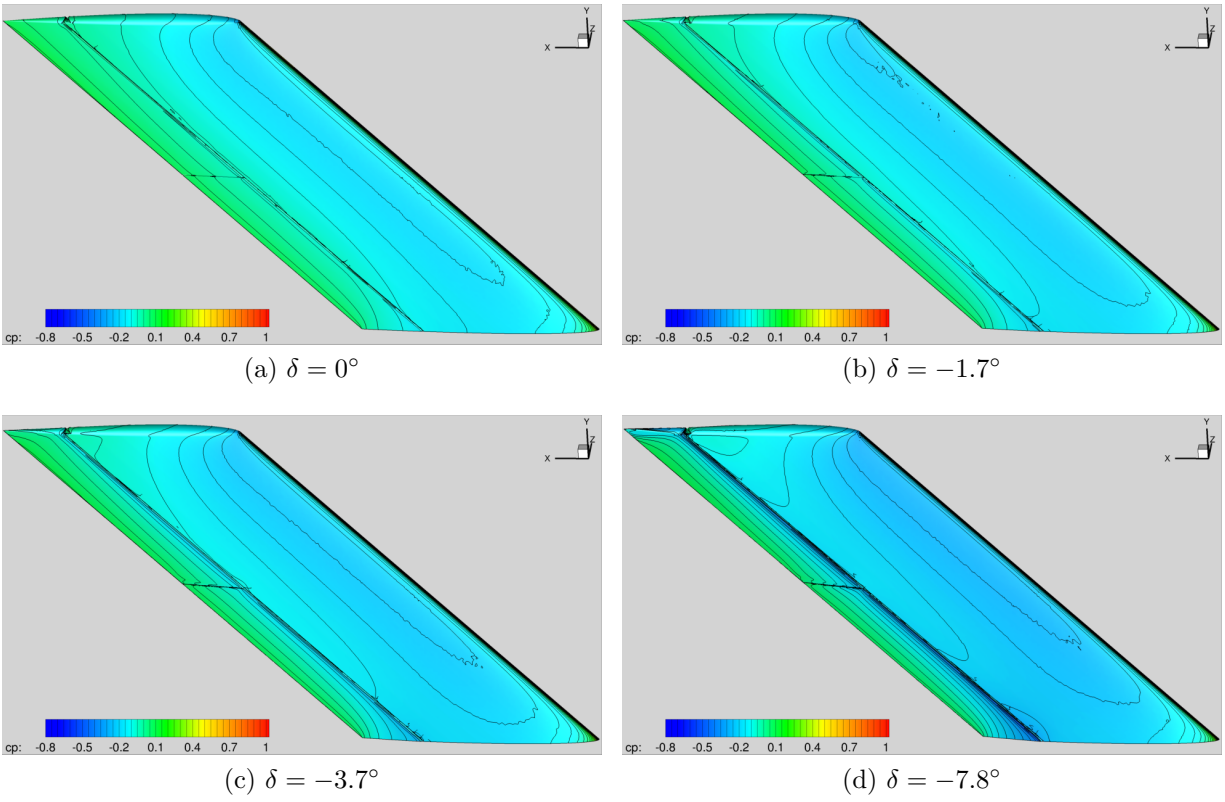


Figure 4.9: Steady FUN3D pressure distribution on an NACA 0012 swept horizontal stabilizer,  $\alpha \approx 0^\circ$

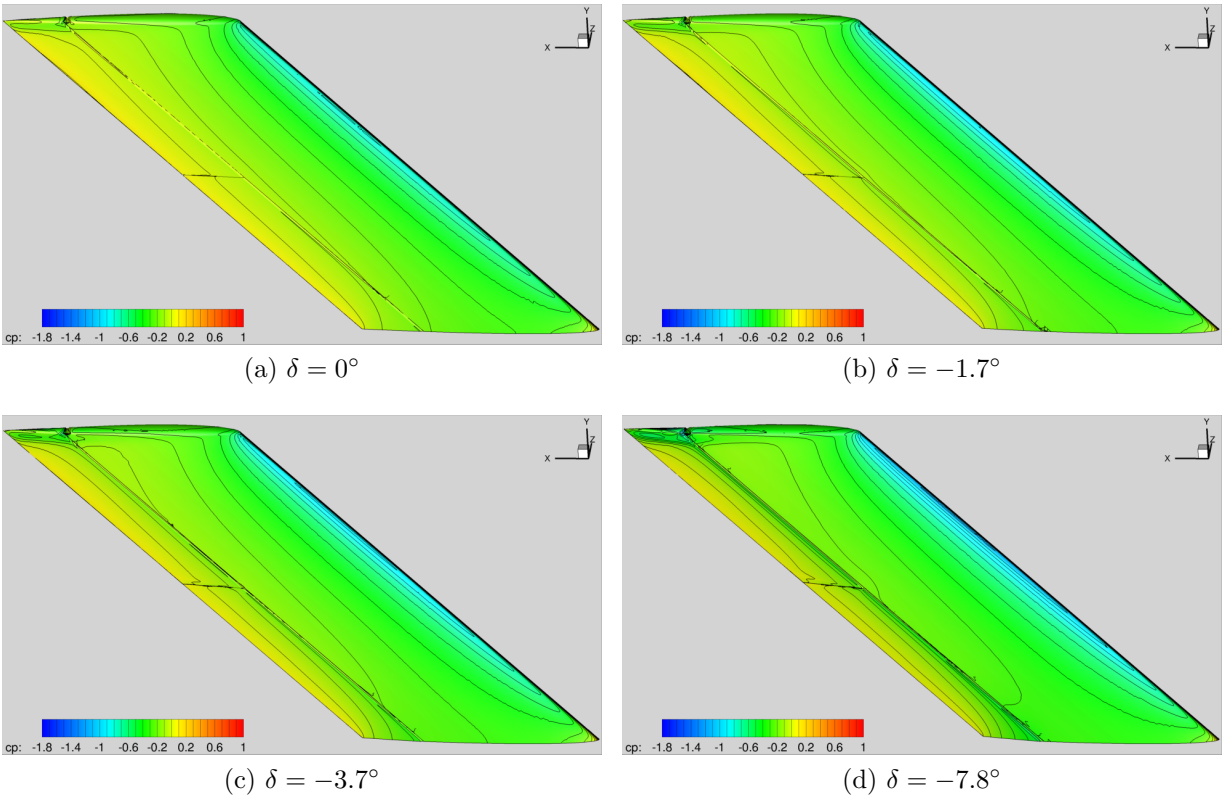


Figure 4.10: Steady FUN3D pressure distribution on an NACA 0012 swept horizontal stabilizer,  $\alpha \approx -4^\circ$

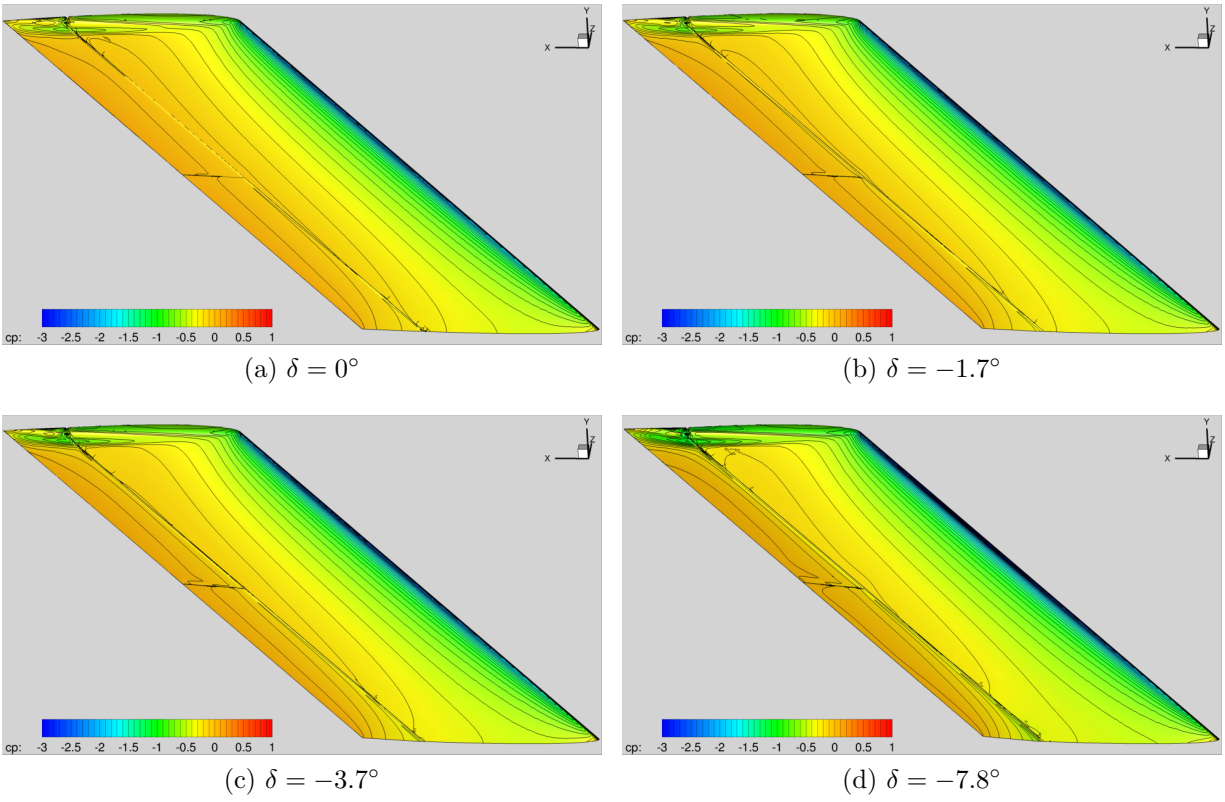


Figure 4.11: Steady FUN3D pressure distribution on an NACA 0012 swept horizontal stabilizer,  $\alpha \approx -8^\circ$

#### 4.4 Steady-State Solution with Manually-Refined Wake

The refined wake mesh is used to compute an angle of attack sweep set of solutions for the  $-7.8^\circ$  deflection case. The solver inputs are otherwise identical to the original mesh.

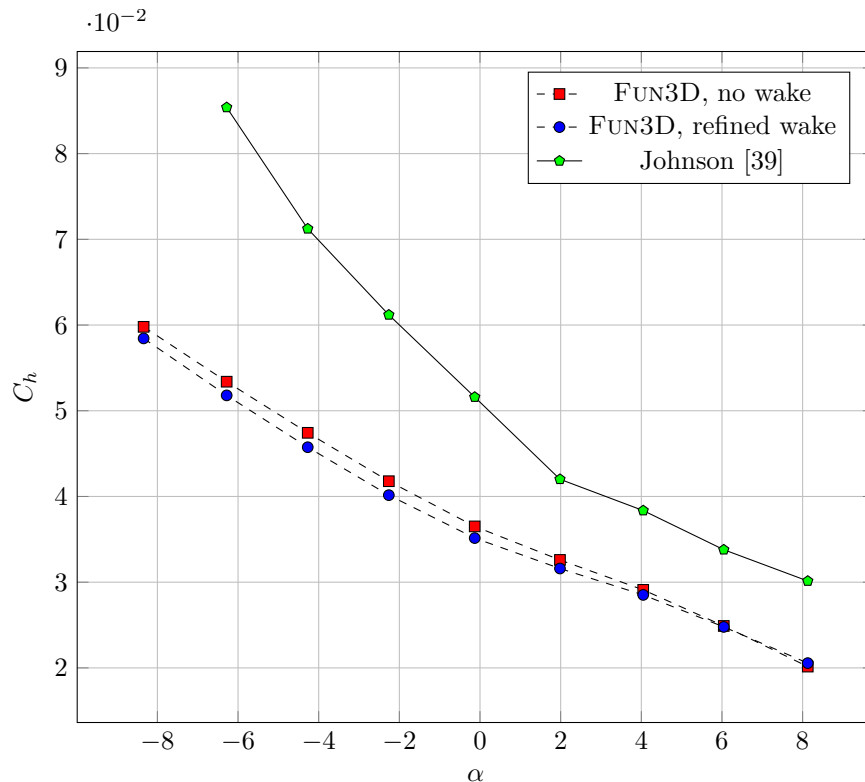


Figure 4.12: NACA 0012 hinge moment coefficient, refined wake mesh;  $\delta = -7.8^\circ$

Figure 4.12 displays the hinge moment coefficient versus angle of attack for both steady-state solutions. The presence of the refined wake does not significantly affect the hinge moment solution accuracy in this case. No appreciable difference is present in either the lift or drag predictions. This indicates that either the spatial resolution is still insufficient even after the manual wake refinement, or the issue is temporal in nature. Based on the results of the GA(W)-1 test case in the previous chapter, it is believed that a time-accurate solution will provide the most accurate results, particularly for a case with flow separation such as this one.

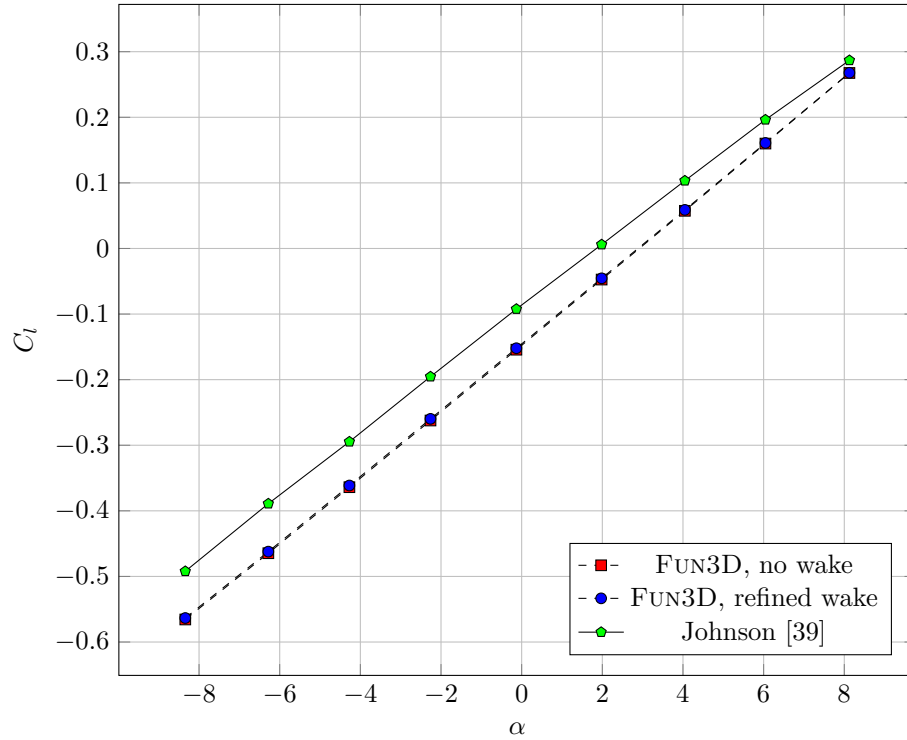


Figure 4.13: NACA 0012 lift coefficient, refined wake mesh;  $\delta = -7.8^\circ$

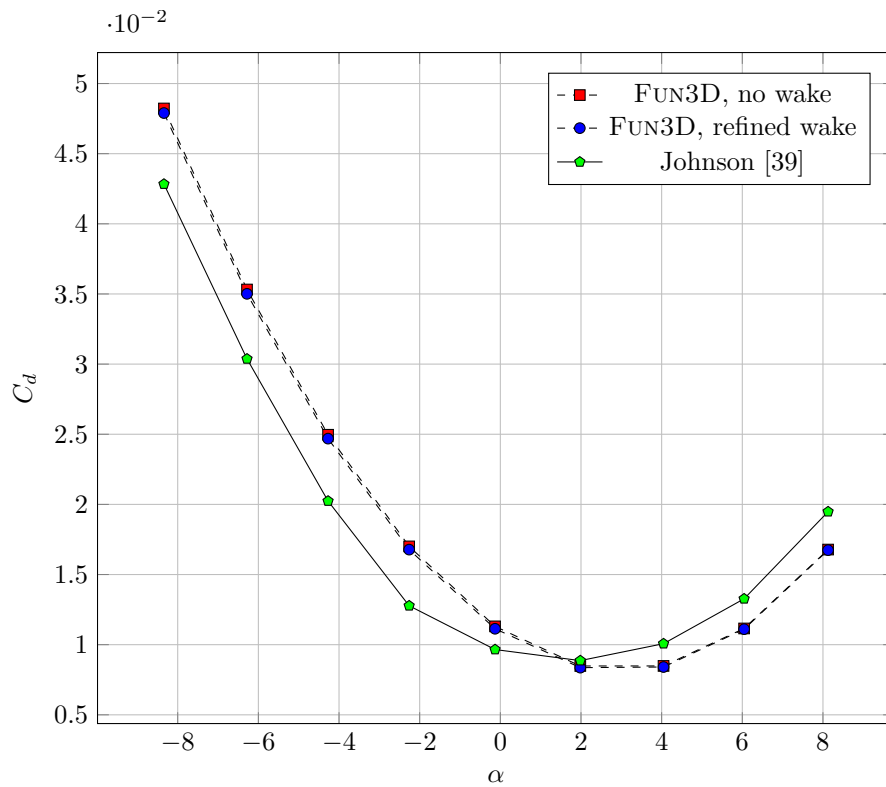


Figure 4.14: NACA 0012 drag coefficient, refined wake mesh;  $\delta = -7.8^\circ$

## 4.5 Discussion of Results

As with the 2D case, a steady-state Navier-Stokes solution is adequate for configurations with little to no flow separation. The higher Mach number causes flow separation at smaller angles of attack and deflection angles, so the range of feasible conditions for using the steady-state solution is narrower than that for a low-speed flow.

Based on the results from the 2D case, a finer mesh would likely increase the accuracy of the hinge moment predictions. However, a finer mesh is not currently feasible for the author due to computational resource constraints. The addition of a baffle wake had little effect on the hinge moment prediction, which suggests that the likely reason for the discrepancy between the reference case and the CFD results is unsteady behavior, as was the case with the GA(W)-1. A time-accurate solution is expected to give a better prediction of hinge moment coefficient.

## CHAPTER 5

### ADJOINT-BASED MESH ADAPTATION

One adaptive mesh algorithm that has received much attention lately is adjoint-based adaptation. Adjoint-based mesh adaptation is an attractive option because it is based on the solution itself rather than on heuristics determined by a subjective engineer. FUN3D is capable of both adjoint-based mesh adaptation and gradient-based adaptation. The description of adjoint-based adaptation that follows is only a brief overview of the process. A complete description of the mathematics involved in adjoint-based adaptation is provided in references [40–44].

#### 5.1 Adaptation Process

The adjoint-based adaptation process starts with an initial mesh. A flow solution is computed on that initial mesh. The engineer specifies a cost function to define the quantities that are significant. For example, the engineer may specify only the drag on a specific component if that is the only quantity of interest.

A flow solution is computed on an initial mesh. The sensitivity of the solution to the location of each node in the mesh is then computed using the adjoint solver. The mesh is then adapted in a way that clusters additional nodes in regions with high sensitivities, and nodes may move away from areas in the mesh which are considered less sensitive to mesh spacing. The process is then repeated to give progressively more refined meshes.

If all goes well, the flow solution obtained using the adapted mesh will converge, and the mesh will be refined in an efficient manner, with more elements in areas of importance and fewer elements in areas that do not affect the solution. The benefit of an adjoint-based

method is that not every gradient needs to be captured to find an accurate solution based on the cost function.

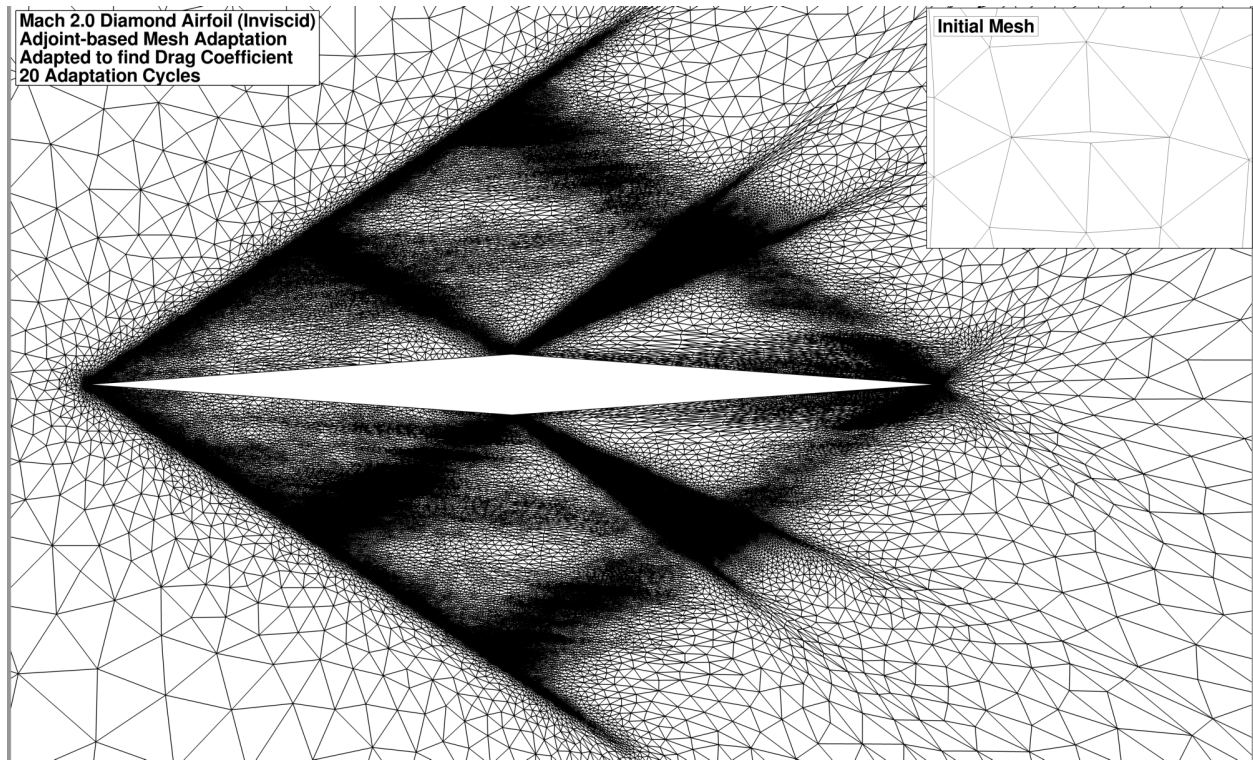


Figure 5.1: Mach 2.0 diamond airfoil mesh.

An inviscid, Mach 2.0, 2D diamond airfoil test case is used to demonstrate a successful application of a solution with adjoint-based mesh adaptation. The objective of this test is to predict the drag on the airfoil. The initial mesh contains 190 nodes and 344 elements, which increases to 579,498 nodes and 1.16 million elements after 20 adaptation cycles. Figure 5.1 shows the initial mesh and the adapted mesh after 20 adaptation cycles. The final mesh clearly shows refinement along characteristics, particularly in regions where shocks and expansion waves are expected. The mesh is considerably coarser in regions where the flow does not strongly affect the drag prediction on the airfoil, especially upstream of the oblique shock waves, downstream of the trailing edge, and generally outside the area of influence as defined by the characteristics. Figure 5.2 shows the final mesh, colored by the solution Mach number.

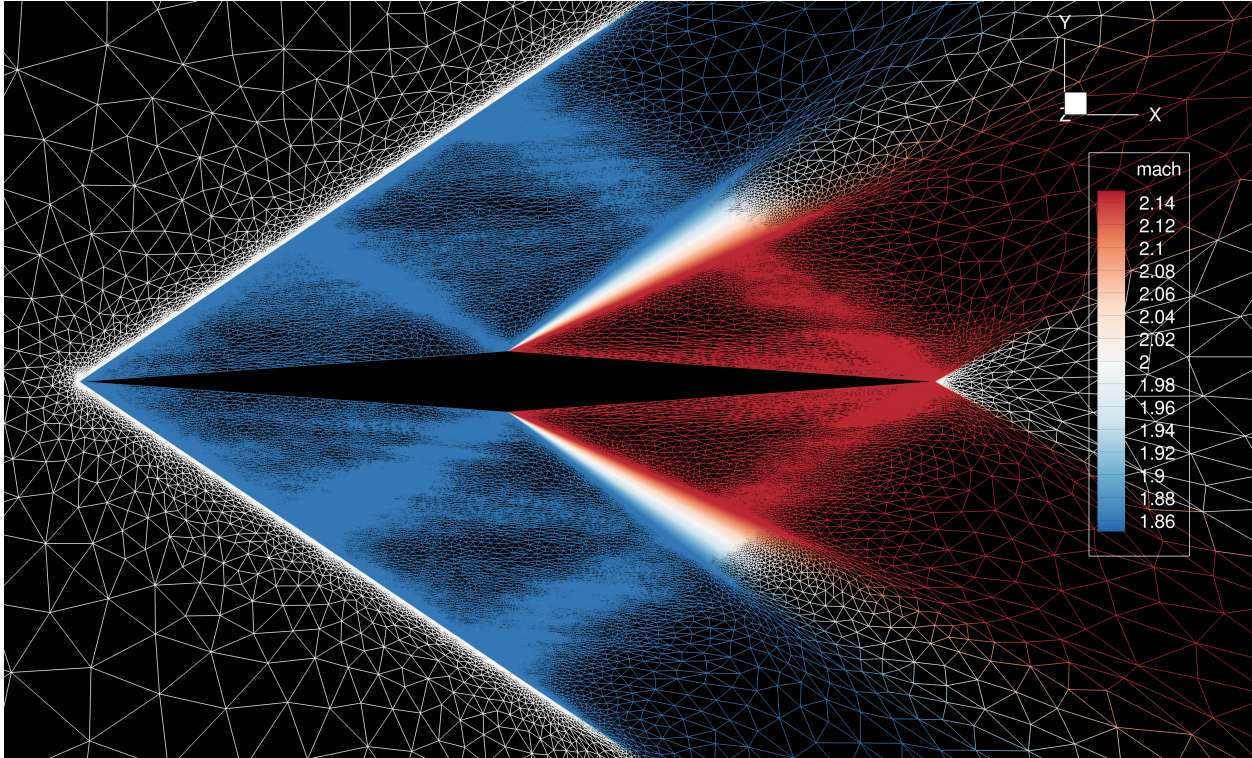


Figure 5.2: Mach 2.0 diamond airfoil mesh after 20 adaptations, colored by Mach number.

A 3D example of a successful adjoint solution is the work done by this author for the 2016 Big Idea Challenge HIAD team from The University of Alabama [45]. The team was responsible for the conceptual design of a Hypersonic Inflatable Aerodynamic Decelerator (HIAD) for Martian atmospheric entry. A 3D CAD model and CFD mesh were created for a particular design configuration. An Euler solution was computed for the configuration using FUN3D's inviscid solver. With a freestream Mach number of 10 and a complex curved geometry, a detached bow shock is known to exist. Furthermore, multiple angles of attack change the shape of the detached bow shock. Manual refinement of the bow shock is infeasible due to the complex shape, so adjoint-based mesh adaptation was used to adaptively refine the mesh. After just 3 adaptation iterations, the bow shock is plainly visible in the resulting mesh as shown in Figure 5.3. The mesh has been refined by the adaptation process to capture the strong gradients associated with the shock wave. The flow aft of the HIAD is completely unsteady. Although the adjoint solver adapted the mesh in that region, the steady adjoint

solver is not well-suited to adapt to unsteady flows, and the mesh is not truly adapted to the correct output in that region. An unsteady adjoint solver is required to adapt a mesh to an unsteady flow.

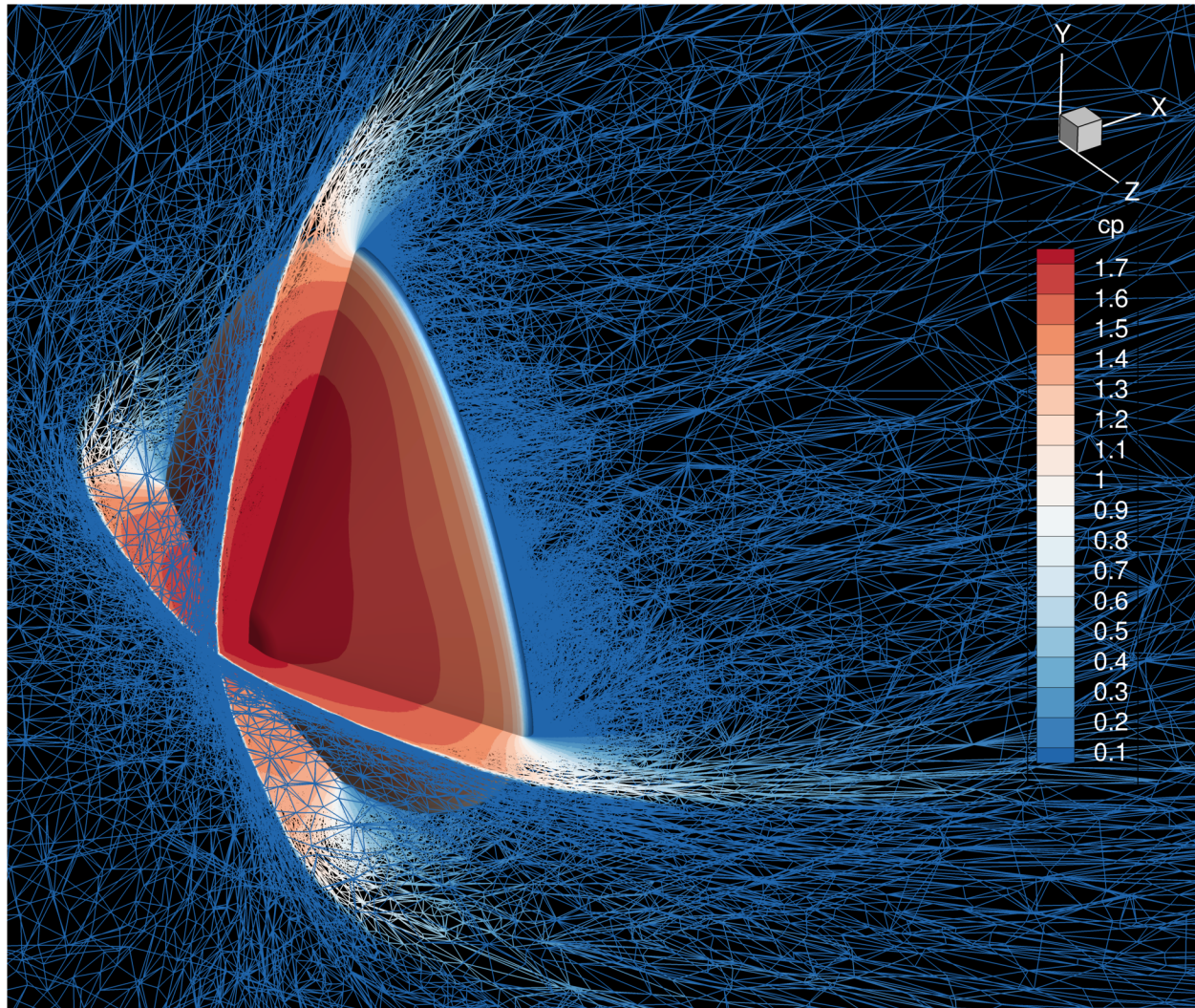


Figure 5.3: HIAD mesh after four adaptation iterations.

The major disadvantage of adjoint-based adaptation is the cost associated with finding the final solution. A complete solution must iteratively adapt the mesh and compute the flow solution for each new mesh. The adjoint solution must be computed again for the new mesh and flow solution. Even after interpolating an existing solution onto the new mesh, the time required to converge to a solution remains significant as the adapted mesh captures additional flow features.

In addition to a greatly increased computational expense, the human cost is not necessarily reduced by using adaptive mesh algorithms. An initial mesh is still required for an adaptive mesh solution. Progress is being made to allow the adaptation of surface meshes, but the implementation in FUN3D is still in development. If the surface cannot be refined automatically, the engineer must create a full-resolution surface mesh. Experience shows that generating a quality surface mesh is one of the dominant challenges in CFD, and as a result it is a significant human cost that is not currently negated by adaptive mesh routines.

The adaptation process requires more user supervision and interaction than a typical CFD solution. A script is used to control the adaptation process, but the user must monitor the residuals to ensure that solutions are converging within the specified number of iterations. The adjoint solution in particular must converge in order to reduce the estimated error. If the adjoint solution does not converge, then the mesh adapts to a divergent output. It is also beneficial for the user to monitor the adapted meshes after each cycle to ensure that the mesh adapts in a manner that makes sense. The desired output can also be monitored to see when the solution has reached a desired convergence.

## **5.2 Computating Hinge Moments on a GA(W)-1 Airfoil with Adjoint-Based Mesh Adaptation**

Due to the complex nature of the flow field around control surfaces, mesh generation can be difficult. The adjoint-based mesh adaptation capabilities of FUN3D are investigated as a means to automatically refine regions in the mesh which are mathematically significant to the solution.

The 2D GA(W)-1 reference case is well-suited for this test due to the relatively large wake region caused by the thick airfoil. A test case with no flow separation is chosen to avoid the need for a time-accurate solution. This case has a deflection angle of  $5^\circ$  and an angle of attack of  $0^\circ$ .

### 5.2.1 Adaptation Parameters

This adaptation case uses FUN3D's `refine/two` mesh adaptation library. In addition to providing routines for adapting the flow field mesh, the `refine/two` library allows the surface mesh to be refined. Surface elements are refined by subdividing elements. At the time of this study, new surface grid points are inserted on the mesh boundary rather than the actual surface boundary, resulting in artificial faceting of curved surfaces. The effects of this faceting are believed to be small for this geometry.

If using an adaptation library that is incapable of surface element refinement, the initial surface mesh must be generated by hand with sufficient resolution. The adaptation process can resolve the viscous boundary layer elements, so an Euler mesh is sufficient for the first iteration.

This case was run on 40 cores on the Cypher cluster at NASA Langley Research Center during a 2015 Summer internship with the Computational Aerosciences Branch. The adaptive solution was allowed to run for 20 adaptation cycles.

The adaptation cycles are controlled using a script that wraps the flow and adjoint solvers. There are a number of parameters available to control the mesh adaptation process, but the three main parameters are the complexity, the maximum anisotropy, and the gradation.

The complexity is used to control the approximate number of nodes in the adapted mesh. The number of nodes in the adapted mesh is linearly related to the complexity, but it is not a 1:1 ratio. The complexity for the  $i^{\text{th}}$  adaptation iteration for this case is set using the equation

$$c = 30000 + 10000i$$

By using an equation like this, the mesh grows linearly with each cycle. Another approach is to scale the complexity by using a growth factor, such as

$$c = A^i c_0$$

If the complexity is left unconstrained, the mesh refinement step tends to add huge quantities of new elements to the mesh, resulting in over-refinement in many areas of the mesh in early adaptation cycles.

The maximum anisotropy constrains the anisotropy allowed in the adapted mesh. It is usually best to start the process using a value that is at least as large as the maximum anisotropy of the initial mesh. Large changes to the mesh are typical in the beginning of the adaptation process, so it is important to keep the aspect ratios fairly low to avoid aggressive stretching in certain regions of the mesh. A larger anisotropy can be allowed in later adaptation cycles to allow the mesh to stretch more in certain regions. The maximum anisotropy for this case is set using the equation

$$a = 10000 (10^{0.1i})$$

In this case, since 20 total cycles are used, this causes the maximum anisotropy to scale from 10,000 in the first iteration up to 1,000,000 in the last iteration.

The gradation is analogous to a growth rate. It governs the relative size of one cell to its neighbors. This is useful for preventing over-refinement of the mesh in early adaptation cycles. In this case, the gradation was fixed at 1.2 to prevent excessive refinement near the airfoil surface for the first five adaptation iterations. The gradation was unconstrained for the remaining cycles. This keeps changes to the mesh relatively moderate in early adaptation iterations, while allowing the solver to more aggressively adapt the mesh in later iterations when changes are typically more subtle.

The hinge moment is chosen as the adaptation objective function. Each adaptation cycle is run for 4000 iterations using the steady-state formulation. The CFL number is ramped from 10 to 100 over the first 300 iterations of each cycle, and the turbulent CFL number is ramped from 1 to 10 over the first 300 iterations. After the 300 iterations, both CFL numbers remain constant. The Spalart-Allmaras turbulent model is used for this case.

### 5.2.2 Results

Figure 5.4 shows the progression of the mesh at various steps in the process. The most drastic changes to the mesh occur in the first few iterations. In early iterations, many elements are primarily added around the control surface and in the viscous boundary layer. As the adaptation continues, a clear wake region forms, and it continues to become more refined in later meshes. The boundary layer reduces in thickness as the adaptation progresses and the flow solution adjusts to the changing mesh. Detailed views of the initial and final meshes are shown in Figures 5.5 and 5.6.

The flow field Mach number for several iterations can be seen in Figure 5.7. The initial Euler mesh clearly gives a poor solution, which is not surprising given the size of the elements adjacent to the viscous wall boundaries. As the mesh is refined, the viscous boundary layer is resolved in much greater detail. The mesh in the wake region is also much more refined. In addition, the stagnation point shifts downward on the leading edge of the airfoil.

The pressure coefficient results show similar improvements, as shown in Figure 5.8. The pressure contours change significantly in the first few cycles. Initial adaptation cycles result in dramatic changes in the shape of the pressure contours, especially in areas around the control surface. After several cycles, changes are relatively minor. In this case, the pressure contours change little between iterations 8 and 20. This is typical of the adjoint-based adaptation. Significant gains are typically seen initially, with diminishing returns in later iterations.

In addition to the adjoint-based mesh adaptation, the global refinement study conducted previously gives a baseline for comparison. Figure 5.9 shows how the hinge moment coefficient varies with the number of nodes. The adaptive solution agrees relatively well with both the reference value and the finest resolution steady-state solution. The adapted mesh gives a solution slightly closer to the reference quantity than the globally-refined mesh, although there is some noise in the adapted solution.

The lift coefficient is shown in Figure 5.11. The adapted solution converges to a slightly

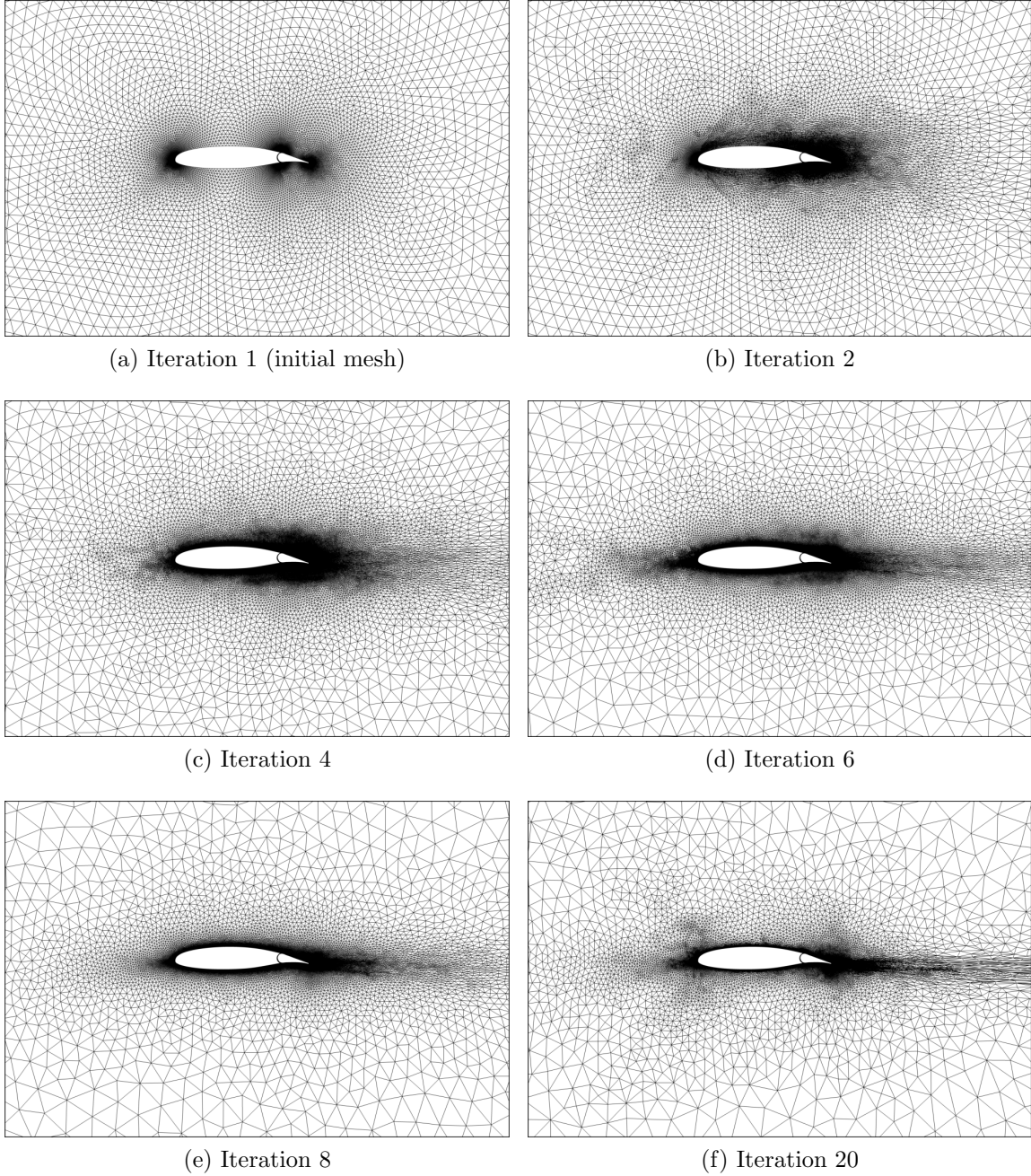


Figure 5.4: GA(W)-1 adjoint-adapted meshes,  $\alpha = 0^\circ$ ;  $\delta = 5^\circ$

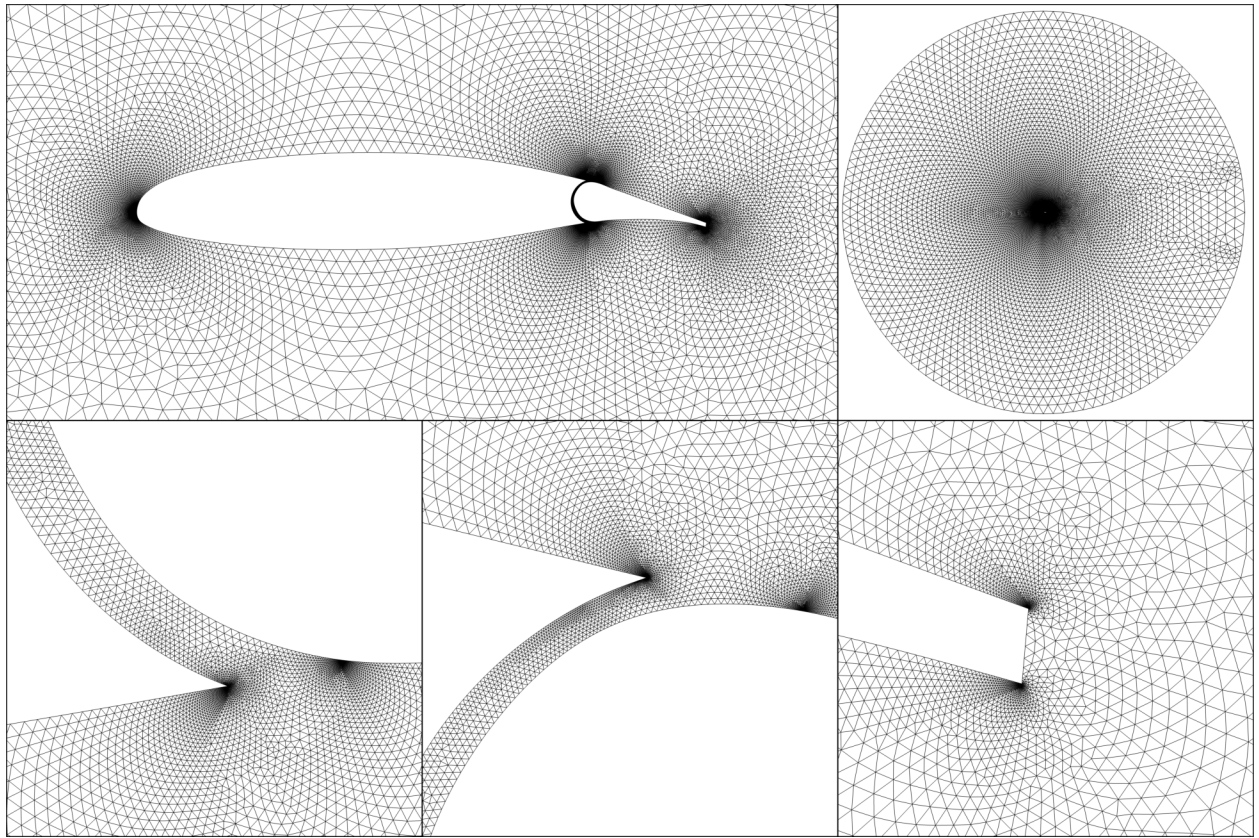


Figure 5.5: Initial GA(W)-1 mesh detail for adjoint-based adaptation,  $\alpha = 0^\circ$ ;  $\delta = 5^\circ$

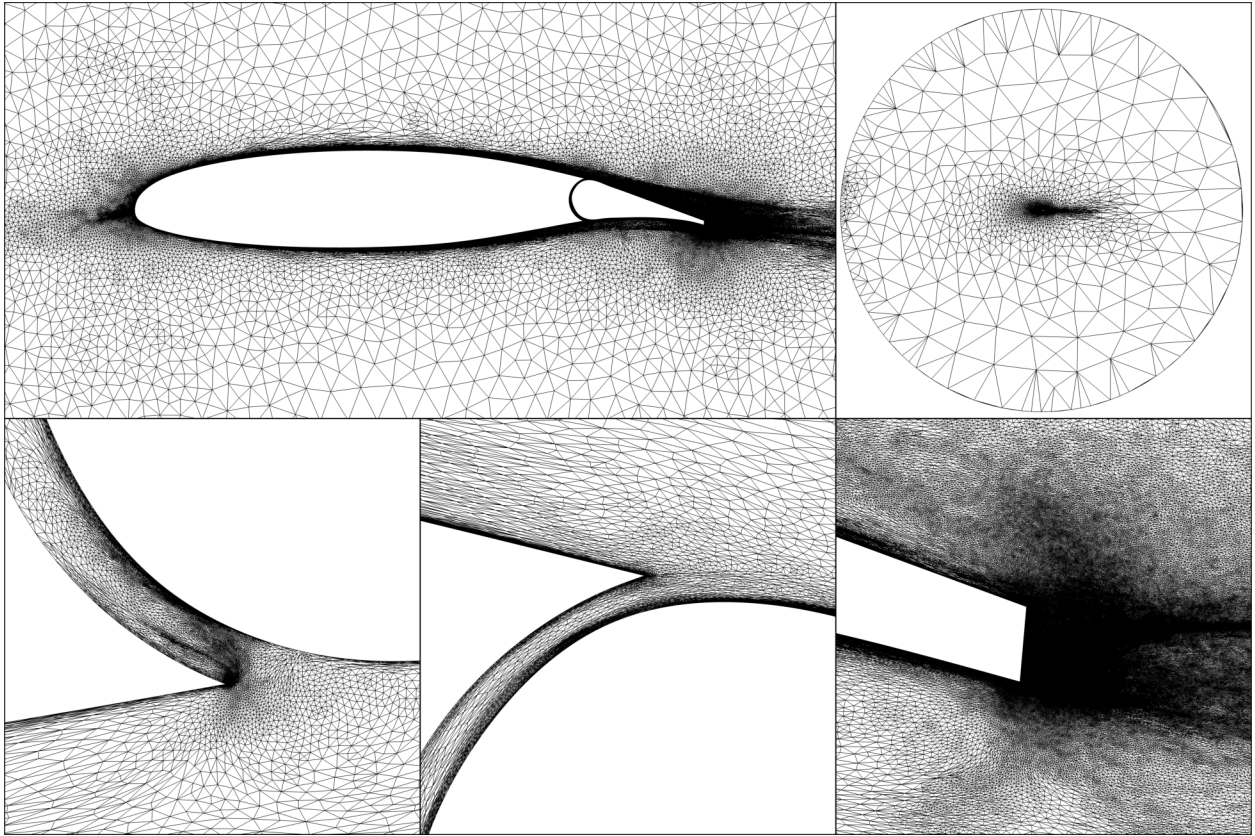


Figure 5.6: Final GA(W)-1 adjoint-adapted mesh detail,  $\alpha = 0^\circ$ ;  $\delta = 5^\circ$

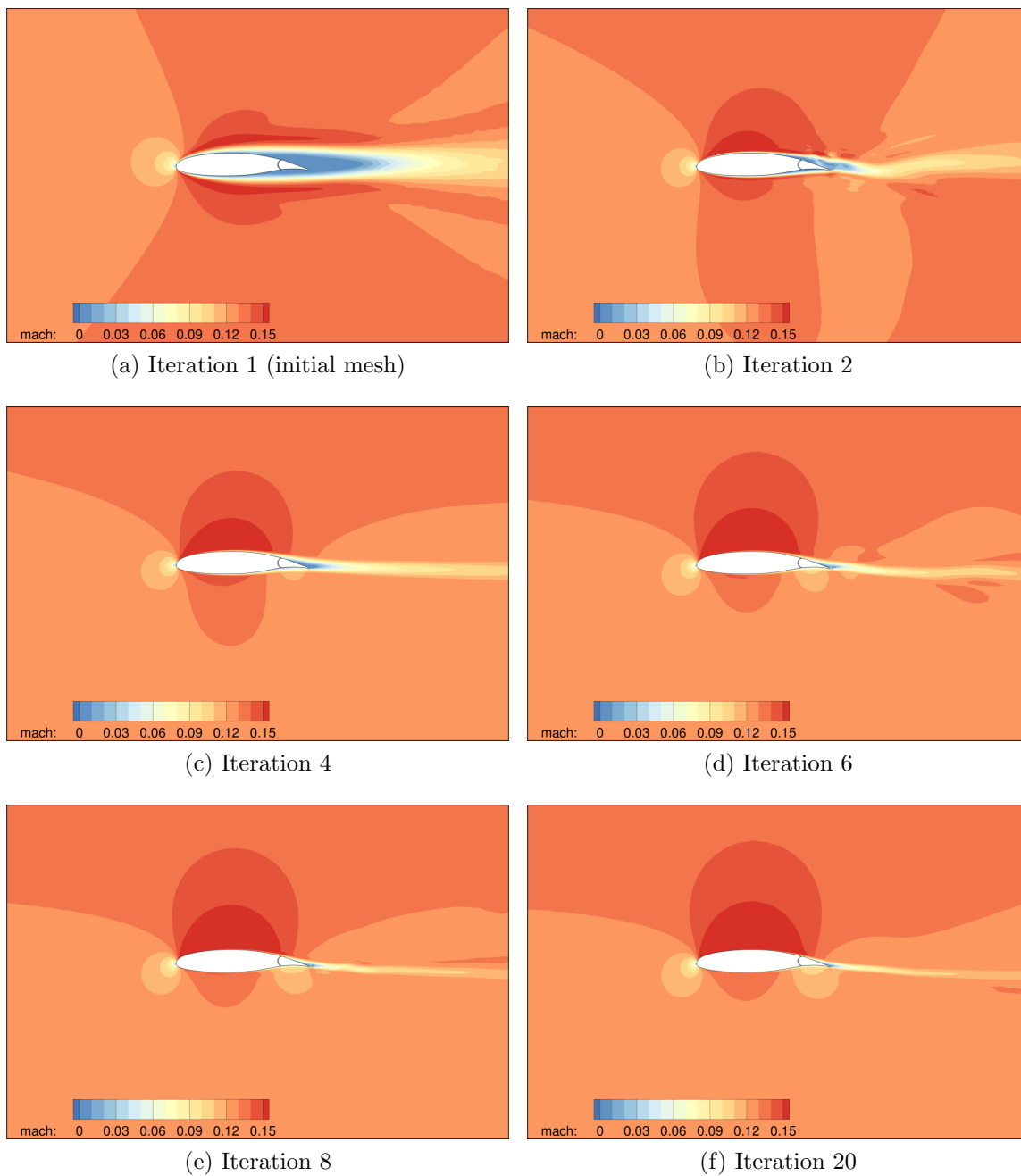


Figure 5.7: GA(W)-1 adjoint-adapted flow field Mach number,  $\alpha = 0^\circ$ ;  $\delta = 5^\circ$

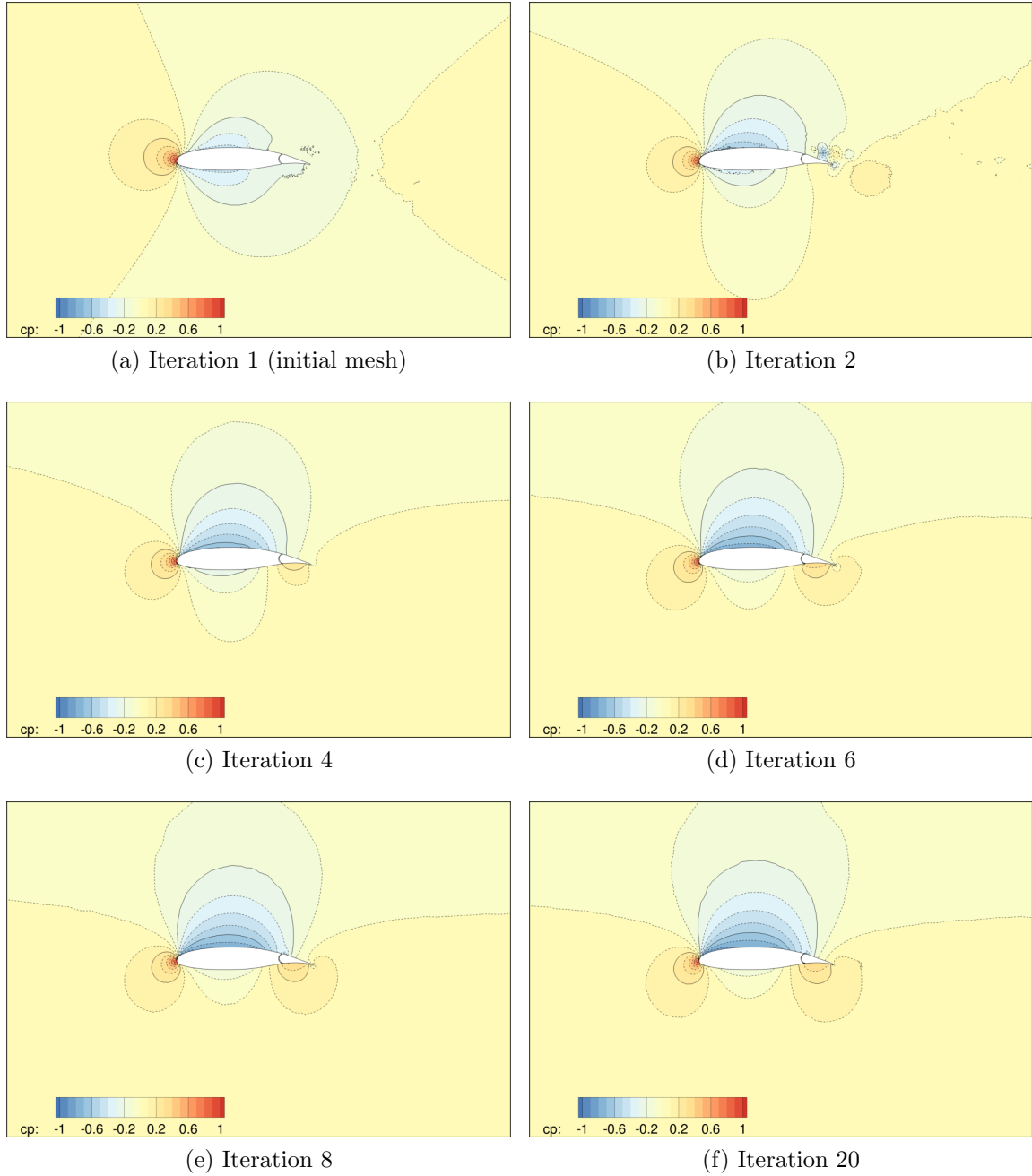


Figure 5.8: GA(W)-1 adjoint-adapted flow field pressure coefficient,  $\alpha = 0^\circ$ ;  $\delta = 5^\circ$

higher value than the global refinement case. Neither steady-state solution agree well with the reference quantity. This is not surprising because the cost function included the hinge moment only, so the mesh adapted based on what was mathematically significant to the hinge moment solution.

The drag coefficient is shown in Figure 5.12. Both solutions converge to a value within 10% of the reference quantity.

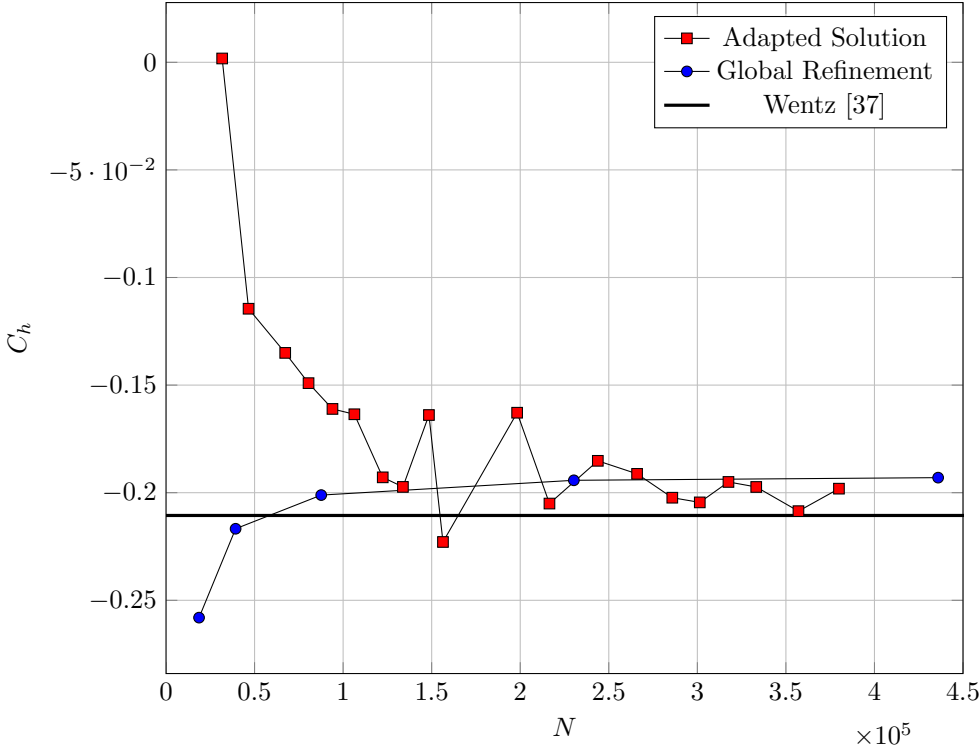


Figure 5.9: GA(W)-1 hinge moment coefficient versus number of grid nodes

In each of the results, the global refinement case gives a different result than the adjoint-based adaptation. This is simply a result of refining the mesh in different areas. The global refinement increases the mesh resolution in all areas by a common factor. The adapted mesh gives more refinement where the adjoint solver determines is most critical for the given output. This is clearly seen in the boundary layer, the wake, and the region leading to the stagnation point on the airfoil leading edge. In general, the adapted mesh contains more elements in important regions than does the global mesh with the same number of grid

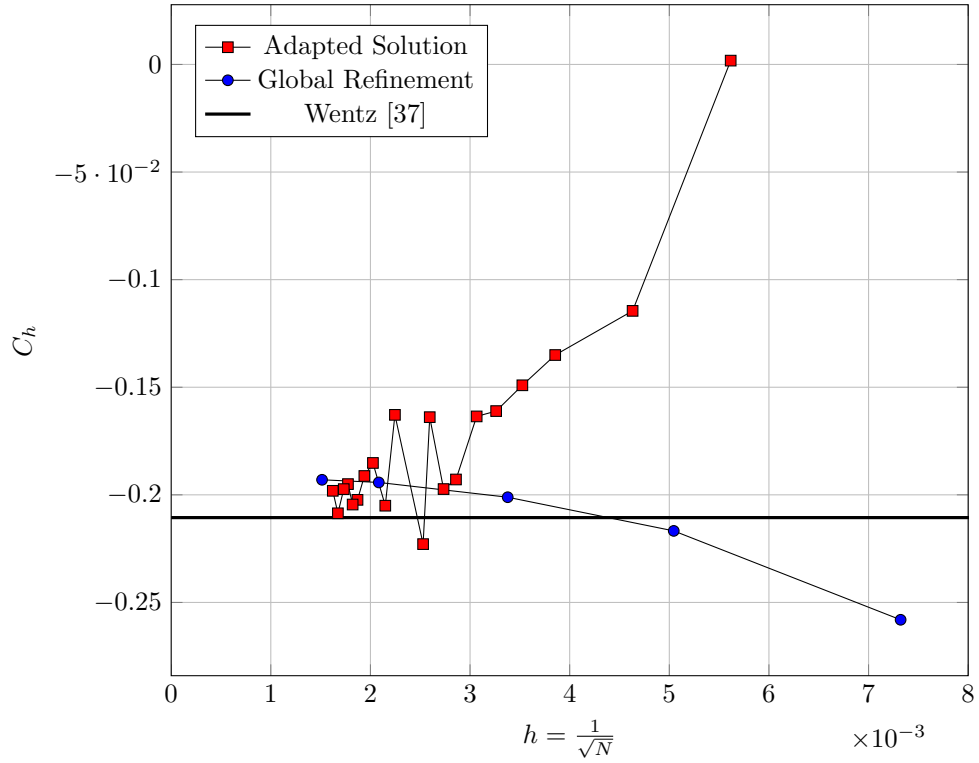


Figure 5.10: GA(W)-1 hinge moment coefficient versus spacing parameter

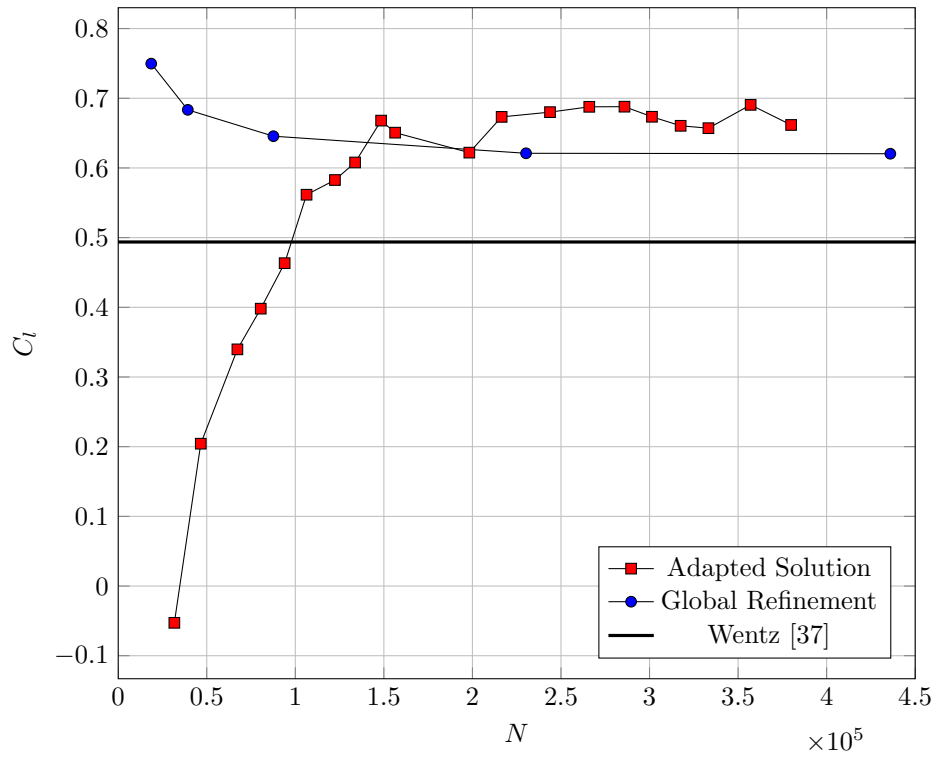


Figure 5.11: GA(W)-1 lift coefficient versus number of grid nodes

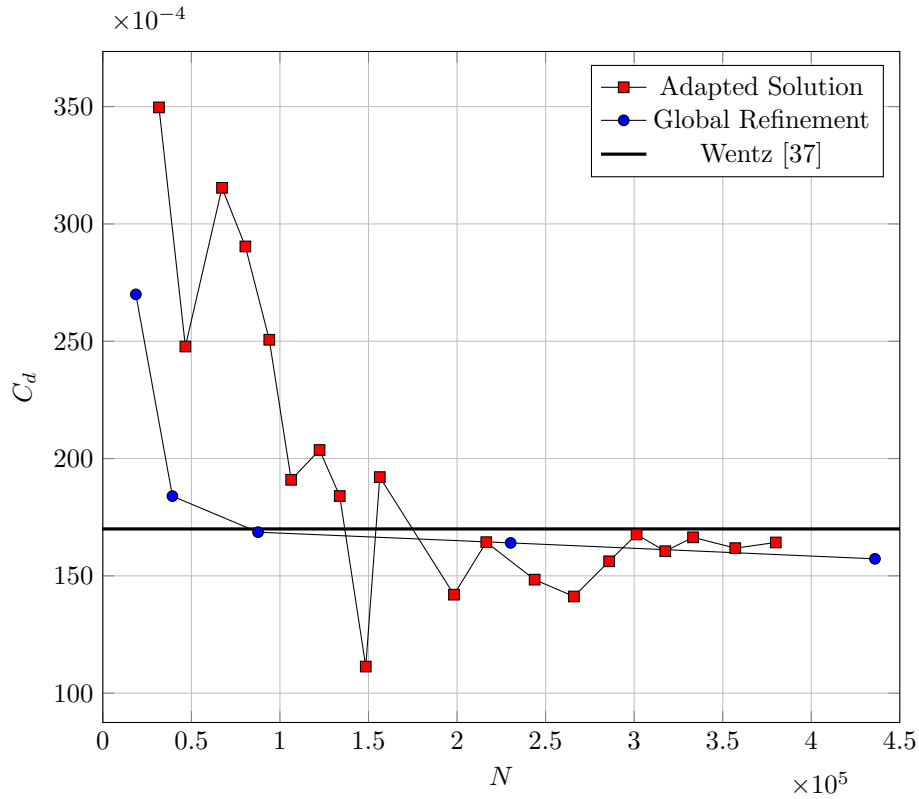


Figure 5.12: GA(W)-1 drag coefficient versus number of grid nodes

points, simply because the adaptation targets those key areas.

The adjoint-based mesh adaptation shows promise for reducing the amount of guesswork in CFD solutions. However, it is more costly than global refinement for a 2D subsonic case. The unsteady adjoint solution becomes a necessity due to the unsteadiness that is common in control surface flows. This further increases the cost of the solution. Depending on the configuration and flight conditions, the increase in computation time may be justified. This is particularly true in transonic and supersonic configurations where complex shock-boundary interactions are present.

## CHAPTER 6

### COST BENEFIT ANALYSIS

Much of the research taking place in the CFD community focuses on improving flow solvers, whether by increasing the fidelity of the solver or by improving its speed. Whereas solvers are often compared for accuracy and performance, rarely is a complete cost-benefit analysis performed to determine the extent to which such improvements benefit an organization. Businesses must rely not only on the speed and accuracy of the software, but also on the human component of cost associated with finding a solution, the capital investment for the equipment, and operational costs associated with the equipment use. For these reasons, this study includes a cost analysis for various solution techniques.

#### 6.1 CFD Cost Estimates

The cost of a CFD solution is dependent upon several factors. There are also costs associated with operating the computer equipment. Software licensing is a major operational cost for an enterprise using CFD. At a minimum, a CAD program is required for creating complex geometries, a mesh generation program is required to create the mesh, and a CFD solver is required to obtain a solution, and a data analysis package is required for visualization and post-processing of results. A typical CAD program such as CATIA V5 costs \$20,000 per seat. A license of a mesh generation software such as Pointwise costs \$5000 plus \$1000 per year. Some flow solvers can be obtained for no monetary cost, but a cost often exists in the form of a lack of support or features.

The operational cost is not limited to software licensing fees. Supercomputer time is also costly. The cost of operating a supercomputer is dominated by energy consumption.

Clusters must also be maintained and upgraded as hardware quickly becomes obsolete. Of course, this does not account for the initial capital investment for an on-site system. Leased CPU time costs approximately \$0.10 per CPU-hour [46, 47], which is representative of the total cluster operational cost, assuming the organization keeps the cluster operating near capacity at all times and upgrades the compute nodes regularly.

Finally, significant human involvement is required for CFD solutions. A CAD model suitable for mesh generation must be made. A mesh is then created for the geometry. The CFD solver must be properly configured, and in many cases, human interaction is required to ensure the solver is running properly. A complete data analysis is completed to extract useful information from the solver output. The human time commitment is compounded for each different configuration, of which any real application will have many.

These costs are evaluated for each of the solution methods presented in this thesis. For the purposes of this study, it is assumed that a CAD model must be generated regardless of the method used, so the cost are factored into the cost of neither the CFD solution nor the wind tunnel solution. Likewise, post-processing of results is assumed to require a similar amount of time, with exception of flow visualization. Furthermore, it is assumed that custom scripts that automate simple routine tasks are available for the engineer as is the case in most organizations. The assumptions used to determine the cost of a CFD solution are given below:

1. Cost of 1 CPU-hour = \$0.01
2. Software costs are minimal when spread over an entire program
3. Engineer costs are not considered

### **6.1.1 GA(W)-1 Reference Case**

Mesh generation for the GA(W)-1 case presented in this thesis was accomplished in just over 2 hours for all deflection angles, including the global mesh refinements. The majority of this time was spent adjusting spacing parameters during the spline-fitting process. About

10 minutes were spent on modifying existing bash scripts that wrap AFLR2 to give multiple deflection angles. The actual mesh generation process required about 2 minutes per configuration for the finest mesh in the study.

The fine-mesh steady-state cases ran on average for 241 CPU-hours, for a total of 13,014 CPU-hours. At \$0.10 per CPU-hour, this amounts to a cost estimate of \$1,301, or \$24.10 per condition. The time-accurate simulations required 782 CPU-hours on average to reach either steady-state or periodic solution, which amounts to an estimate of \$78.20 per condition. Had all 54 test points been tested, this would amount to 42,228 CPU-hours or an estimated \$4,223 for the complete set of runs. Finally, the adjoint-based adaptation case required a total of 799.2 CPU-hours, which has an estimated cost of \$79.92. A complete set of 54 runs would require 43,157 CPU-hours, which would cost about \$4,316.

Submitting and managing the jobs on the supercomputer required about 1 man-hour for all steady-state solutions and 5 man-hours for the time-accurate solutions. The time-accurate solution requires significantly more human interaction to determine whether sufficient subiterations are being used. The solution must also be monitored to see when the periodic behavior emerges, so that the solution may be stopped and optionally restarted to output the flow field snapshots. The adjoint-based adaptation requires even more human interaction than the time-accurate solution, although the exact amount is difficult to quantify.

Table 6.1: Comparison of cost estimates for various solution methods for predicting hinge moments on a GA(W)-1 airfoil

Quantity	Steady-State	Time-Accurate	Adaptive Steady-State
Cores per Condition	48	48	40
Hours per Condition	5.02	16.29	19.98
CPU-Hours per Condition	241	782	799
Estimated Cost per Condition	\$24.10	\$78.20	\$79.92

A summary of the cost of GA(W)-1 test cases is shown in 6.1. The steady-state adaptive solution costs 3.3 times the steady-state solution with a globally-refined mesh. The previous chapter shows that both solutions give comparable results. It is clear that for a low-speed 2D configuration, a globally-refined mesh should be preferred over an adaptive solution.

A time-accurate solution can be obtained for about the same cost of an adaptive steady-state solution. Given the significant improvement in solution accuracy of the time-accurate solution over the steady-state solution, this is a significantly better value. However, in a test case where shock waves are expected, the adjoint-based adaptation will have significant value.

### 6.1.2 NACA 0012 Swept Wing

Unlike the 2D test case, mesh generation for a the NACA 0012 swept wing requires a significant amount of time. It is estimated that one entire week was spent on constructing meshes for all configurations.

The steady-state solutions were run on 176 cores for an average of 10.33 hours. This gives 1,818 CPU-hours, or an estimated \$182 per condition. For all 36 conditions in this study, that amounts to \$6,544. The time-accurate solution is expected to be significantly more expensive than the steady-state solution.

Table 6.2: Cost estimate for predicting hinge moments on an NACA 0012 swept wing

Quantity	Steady-State
Cores per Condition	176
Hours per Condition	10.33
CPU-Hours per Condition	1,817.9
Estimated Cost per Condition	\$181.79

### 6.1.3 Full Aircraft Model

Johnson [19] provides information about CFD solution on a full transonic aircraft model using CFD. The mesh contained 25 million grid points, and each condition was run on 56 cores. Each solution was obtained within 11 hours. This gives an estimate of 616 CPU-hours.

The full aircraft mesh is too coarse to accurately determine hinge moment coefficients based on the results found in this study. However, the case is a useful reference to demonstrate the cost effectiveness of CFD solutions in general. Given the same \$0.10 per CPU-hour cost as used in the above estimates, each condition would cost \$61.60. These values are shown

in Table 6.3.

Table 6.3: Cost estimate for a CFD solution on a full aircraft configuration

Quantity	Value
cores per Condition	56
Hours per Condition	11
CPU-Hours per Condition	616
Estimated Cost per Condition	\$61.60

## 6.2 Wind Tunnel Cost Estimates

For a wind tunnel test, a precise physical model must be manufactured. Engineers are also needed to prepare the model for testing, run the wind tunnel experiments, and analyze the data. The wind tunnel itself also has costs associated with energy consumption and maintenance. The use of an educational facility such as Texas A&M’s Oran W. Nicks Low Speed Wind Tunnel or the University of Washington Kirsten Wind Tunnel is about \$500 per hour of tunnel occupancy, plus additional cost for any overtime, equipment, labor, and other incidentals, according to the tunnel websites [48, 49]. Using a commercial wind tunnel facility such as the San Diego Low-Speed Wind Tunnel costs on the order of \$800-850 per hour [50].

Wind-tunnel models are typically expensive. A full aircraft configuration can cost hundreds of thousands of dollars [51].

Setup costs are computed as (hourly tunnel fee)  $\times$  (setup time in hours). The cost per configuration is computed as (minutes of run time per condition)  $\times$  (tunnel fee per minute). The cost of a configuration change is calculated as (hourly tunnel fee)  $\times$  (number of configurations - 1). Model costs are assumptions based on knowledge of the model complexity in reference cases and anecdotal references. For the purposes of these cost estimates, engineer costs have been neglected.

Real cost information about the wind-tunnel tests are unavailable, so assumptions have been made to enable a cost estimate. The assumptions and cost estimates for the GA(W)-1

Table 6.4: Wind tunnel assumptions and cost estimates

Quantity	GA(W)-1	NACA 0012 Wing	Full Aircraft
Conditions per Configuration	6	9	8*
Configurations	9	4	56*
Hourly Tunnel Fee	\$850	\$850	\$1000
Setup Time	8 hr.*	8 hr.*	16 hr.*
Setup Cost	\$6,800	\$6,800	
Model Cost	\$7,500*	\$75,000*	\$200,000*
Run Time per Condition	1 min.*	1 min.*	1 min.*
Run Cost per Configuration	\$85.00	\$127.50	\$133.33
Configuration Change Time	30 min.*	60 min.*	240 min.*
Configuration Change Costs	\$3,400	\$2,550	\$220,000
Total Cost Estimate	\$18,465	\$84,860	\$443,467

\*Assumed value

airfoil, NACA 0012 swept wing, and an assumed full aircraft configuration are listed in 6.4. The full aircraft estimates are based on the assumption that 8 angles of attack will be tested for 56 different configurations. These configurations could be various combinations of aileron and spoiler deflections, for example.

### 6.3 Discussion

The primary motivation behind using CFD is the potential for cost savings. Kraft [17] explains that the overwhelming majority of the cost savings do not come from reducing the expenditure on wind tunnel tests, but rather by reducing the overall cycle time in the development of an aircraft. CFD has a much faster cycle time than wind-tunnel testing due to the limited availability of wind-tunnel facilities and time required to construct the models.

Table 6.5: Comparison of cost estimates of CFD solutions and wind-tunnel testing

Case Study	CFD*	Wind Tunnel
GA(W)-1 (steady-state)	\$1,301	
GA(W)-1 (time-accurate)	\$4,223	\$18,465
GA(W)-1 (adaptive steady-state)	\$4,316	
NACA 0012 swept wing	\$6,544	\$84,860
Full Aircraft	\$27,597	\$443,467

\*Using the same number of conditions as the wind-tunnel estimate

## CHAPTER 7

### CONCLUSIONS AND FUTURE WORK

#### 7.1 Conclusions

Though the test cases in this study are geometrically simple, many insights have been gained during the numerical studies. A number of meaningful conclusions can be drawn from the work presented in this thesis.

1. Empirical relations can be used to predict  $C_{h_\delta}$  for a narrow range of conditions. When combined with some known value of  $C_{h_0}$ , a crude estimate of hinge moment coefficient can be made.
2. XFOIL can accurately predict control surface hinge moments only for 2D configurations with small deflection angles and for small angles of attack. The speed of XFOIL makes it a useful tool during conceptual design for testing many different configurations in a short amount of time.
3. A steady-state Navier-Stokes solution is capable of accurately predicting control surface hinge moments in the presence of small, non-shedding regions of flow separations.
4. A time-accurate Navier-Stokes simulation is required for accurate prediction of control surface hinge moments when separated flow with vortex shedding is present. A time-accurate solution also provides a time history of the hinge moments rather than a single average value. This is important when considering the structure and mechanical devices required to support and actuate control surfaces.

5. The spatial resolution required for accurate hinge moment prediction is much finer than expected. As an example, Kraft [17] provides the CFD grid point count for a couple of full aircraft models with between 18 and 30 million grid points. This is comparable to the number of points in the NACA 0012 swept horizontal stabilizer case presented in this study. Fewer grid points are insufficient to accurately capture the control surface hinge moments.
6. The time step required to capture the unsteady behavior is smaller than expected. The unsteady behavior tends to decay to a steady-state solution if the time step is too large.
7. The initial condition of a time-accurate solution dramatically affects the number of iterations required for the long-term periodic behavior to develop. Restarting from a steady-state solution requires many more iterations for the periodic behavior to emerge. The most reliable method found to excite the unsteady behavior is to initialize the flow with the freestream velocity.
8. The final periodic behavior of a time-accurate solution depends slightly on the initial condition. The effect is small, but it does affect the time-averaged values. The exact relationship between initial condition and the final periodic behavior in this study is unknown.
9. Adjoint-based mesh adaptation can be used to automatically refine a CFD mesh to solve control surface hinge moments. The resulting hinge moment prediction is comparable to the steady-state solution with a fine mesh.
10. The cost of an adaptive, steady-state, subsonic 2D case is not justified in terms of solution accuracy. A time-accurate solution can be computed using a globally-refined mesh with much greater accuracy for approximately the same cost as an adaptive solution. For transonic and supersonic cases, the adaptive solution will have the additional ben-

effort of refining the mesh near shocks, which is generally difficult to accomplish through manual grid refinement.

11. CFD is a cost-effective method of predicting control surface hinge moments. Wind-tunnel tests are more expensive than a CFD solution for the same conditions, and CFD generally offers a shorter development cycle because wind-tunnel availability is scarce. In a program that spends \$1-3 million per day, the cost savings by shortening the development cycle is much more significant than a reduction in a single expenditure.

## 7.2 Future Work

The results from this thesis lead naturally to a number of future projects. Much has been learned from the cases in this study, and there are yet more insights to be gained from more detailed studies.

1. A study investigating reported discrepancies that often exist between CFD, wind-tunnel, and flight test measurements of control surface hinge moments is of great interest. Even matching Reynolds number, all three results have been known to differ significantly. The exact cause of the differences has not been quantified. Among the potential causes to investigate are model simplifications and geometry imperfections.
2. A time-accurate solution coupled with an unsteady adjoint-based adaptive mesh case is a topic of some interest. The time-accurate solution offers the most precise prediction of hinge moments, and it is often difficult to know where to manually refine a mesh while keeping the computational efficiency of a mesh. The unsteady adjoint solver has the potential to reduce the workload required by an engineer, and quantitatively improves mesh quality where dictated by the solution.
3. A full spatial and temporal resolution study on a time-accurate 3D test case is needed. The NACA 0012 swept horizontal stabilizer case provides many experimental data

points for a range of Mach numbers, including several transonic cases. Further investigation using this test case should include the use of adjoint-based mesh adaptation. The wake roll-up that occurs on any lifting body is difficult to model with manual mesh generation. The availability of transonic experimental data gives a unique opportunity to validate hinge moment predictions in high-speed flight conditions.

4. An application of inverse design using adjoint-based methods to optimize control surface geometry is also of interest. Hinge moment balancing devices can take many forms, and the performance of the devices can be difficult to predict. Aircraft weight savings can be had if an aerodynamic balance can be designed to counteract hinge moments.

## REFERENCES

- [1] Michael Wilson. *Harrier*. *Flight International*, page 732, November 1967.
- [2] Ira H. Abbott, Albert E. von Doenhoff, and Louis S. Stivers, Jr. *Summary of Airfoil Data*. Report No. 824, National Advisory Committee for Aeronautics, 1945.
- [3] Paul F. Borchers, James A. Franklin, and Jay W. Fletcher. *Flight Research at Ames, 1940-1997*. NASA Ames Research Center, Moffett Field, California, 1998.
- [4] George E. Cooper and Jr. Robert P. Harper. *The Use of Pilot Rating in the Evaluation of Aircraft Handling Qualities*. Technical Note TN D-5153, NASA, November 1966.
- [5] Marvin R. Barber, Charles K. Jones, Thomas R. Sisk, and Fred W. Haise. *An Evaluation of the Handling Qualities of Seven General-Aviation Aircraft*. Technical Note TN D-3726, NASA, November 1966.
- [6] Wolf Czaia. *Project 262*. NeunundzwanzigSechs Verlag, 2007.
- [7] Jeff Rich, Mike Dorris, and Alan Tolle. *NTSB Factual Report - Aviation*. NTSB Report LAX02LA283, September 2002.
- [8] Phil Powell and Bob Maynard. *NTSB Factual Report - Aviation*. NTSB Report ATL04LA126, June 2004.
- [9] Gregory A. Feith. *NTSB Factual Report - Aviation*. NTSB Report DCA95MA001, October 1994.
- [10] Gregory A. Feith. *NTSB Factual Report - Aviation*. NTSB Report DCA93IA027, March 1993.
- [11] John D. Anderson. *Fundamentals of Aerodynamics*. McGraw-Hill, 4th edition, 2007.

- [12] Richard J. Re. *Stability and Control Characteristics, Including Aileron Hinge Moments, of a Model of a Supercritical-Wing Research Airplane*. Technical Memorandum X-2929, NASA, May 1974.
- [13] Irving L. Ashkenas, Henry R. Jex, and Duane T. McRuer. *Pilot-Induced Oscillations: Their Cause and Analysis*. Norair Report NOR-64-143, Northrop, June 1964. Prepared by Systems Technology, Inc. Report STI TR-239-2.
- [14] Arvo A. Luoma. *A Transonic Wind-Tunnel Investigation of the Trim and Dynamic Response Characteristics of the Horizontal Tail of a 1/7-Scale Model of the Complete Tail of the Grumman XF10F-1 Airplane*. Research Memorandum RM SL53D28, NACA, April 1953.
- [15] W. Letko and W. B. Kemp. *Wind-Tunnel Tests of Ailerons at Various Speeds III - Ailerons of 0.20 Airfoil Chord and True Contour with 0.35-Aileron-Chord Frise Balance on the NACA 23012 Airfoil*. Wartime Report L-325, NACA, September 1943.
- [16] Harry Greenberg and Leonard Sternfield. *A Theoretical Investigation of Longitudinal Stability of Airplanes with Free Controls Including Effect of Friction in Control System*. Report No. 791, NACA, 1944.
- [17] Edward M. Kraft. *After 40 Years Why Hasn't the Computer Replaced the Wind Tunnel?* *ITEA Journal*, 31:329–346, September 2010.
- [18] J. B. Vos, A. Rizzi, D. Darracq, and E. H. Hirschel. *Navier-Stokes Solvers in European Aircraft Design*. *Progress in Aerospace Sciences*, 38:601–697, 2002.
- [19] Forrester T. Johnson, Edward n. Tinoco, and N. Jong Yu. *Thirty Years of Development and Application of CFD at Boeing Commercial Airplanes, Seattle*. *Computers & Fluids*, (34):1115–1151, June 2004.
- [20] Guillaume Fillola, Marie-Claire Le Pape, and Marc Montagnac. *Numerical Simulations Around Wing Control Surfaces*. In *24th International Congress of the Aeronautical Sciences*. ICAS, 2004.
- [21] K. A. Makarov and A. A. Pavlenko. *Numerical Investigation of an Aileron Hinge Moments and Effectiveness on a High Lift Wing Airfoil*. In *29th Congress of the International Council of the Aeronautical Sciences*. Central Aerohydrodynamic Institute named after prof. N. E. Zhukovsky (TsAGI), ICAS, September 2014.

- [22] Robert M. Crane. *Computation of Hinge-Moment Characteristics of Horizontal Tails from Section Data*. Wartime Report A-11, NACA, April 1945.
- [23] Jack N. Nielsen, George E. Kaatari, and William C. Drake. *Comparison Between Prediction and Experiment for All-Movable Wing and Body Combinations at Supersonic Speeds - Lift, Pitching Moment, and Hinge Moment*. Research Memorandum RM A52D29, NACA, August 1952.
- [24] Jack N. Nielsen and Frederick K. Goodwin. *Preliminary Method for Estimating Hinge Moments of All-Movable Controls*. Technical Report NEAR TR 268, Office of Naval Research, March 1982. Prepared by Nielsen Engineering and Research, Inc.
- [25] Robert S. Swanson and Clarence L. Gillis. *Limitations of Lifting-Line Theory for Estimation of Aileron Hinge-Moment Characteristics*. Confidential Bulletin CB 3L02, NACA, December 1943.
- [26] R. D. Finck et al. *USAF Stability and Control Datcom*. Report AFWAL-TR-83-3048, Flight Control Division, Air Force Flight Dynamics Laboratory, Wright-Patterson Air Force Base, Dayton, Ohio, April 1978.
- [27] Boyd Perry. *Control-Surface Hinge-Moment Calculations for a High-Aspect-Ratio Supercritical Wing*. Technical Memorandum 78664, NASA, September 1978.
- [28] M. Grismer, D. Kinsey, and D. Grismer. *Hinge Moment Predictions using CFD*. In *18th AIAA Applied Aerodynamics Conference*, number 2000-4325, August 2000.
- [29] Mark Drela. *XFOIL: An Analysis and Design for Low Reynolds Number Airfoils*. In *Low Reynolds Number Aerodynamics*, volume 54 of *Lecture Notes in Engineering*. Springer-Verlag, 1989.
- [30] Mark Drela and Michael B. Giles. *Viscous-Inviscid Analysis of Transonic and Low Reynolds Number Airfoils*. *AIAA Journal*, 25(10), October 1987.
- [31] Robert T. Biedron et al. *FUN3D Manual: 12.7*. Technical Memorandum TM-2015-218761, NASA, May 2015.
- [32] George Karypis and Vipin Kumar. *A Fast and Highly Quality Multilevel Scheme for Partitioning Irregular Graphs*. *SIAM Journal on Scientific Computing*, 20(1):359–392, 1999.

- [33] Jamshid A. Samareh. *Novel Multidisciplinary Shape Parameterization Approach*. *AIAA Journal of Aircraft*, 38(6):1015–1024, December 2001.
- [34] Jamshid A. Samareh. *Aerodynamic Shape Optimization Based on Free-Form Deformation*. 2004. AIAA Paper 2004-4630.
- [35] P. R. Spalart and S. R. Allmaras. *A one-Equation Turbulence Model for Aerodynamic Flows*. In *30th Aerospace Sciences Meeting & Exhibit*. AIAA, January 1992.
- [36] Robert J. McGhee and William D. Beasley. *Low-speed Aerodynamic Characteristics of a 17-percent-thick Airfoil Section Designed for General Aviation Applications*. Technical Note TN D-7428, NASA, December 1973.
- [37] W. H. Wentz, Jr., H. C. Seetharam, and K. A. Fisco. *Force and Pressure Tests of the GA(W)-1 Airfoil with a 20% Aileron and Pressure Tests with a 30% Fowler Flap*. Contractor Report CR-2833, NASA, June 1977.
- [38] Robert J. McGhee, William D. Beasley, and Richard T. Whitcomb. *NASA Low- and Medium-Speed Airfoil Development*. Technical Memorandum TM-78709, NASA, March 1979.
- [39] Harold S. Johnson and Robert F. Thompson. *Investigation at High Subsonic Speeds of a 45° Sweptback Horizontal Tail with Plain and Horn-Balanced Control Surfaces*. Research Memorandum RM L50B13, NACA, March 1950.
- [40] David A. Venditti. *Grid Adaptation for Functional Outputs of Compressible Flow Simulations*. Ph.d., Massachusetts Institute of Technology, 2002.
- [41] David A. Venditti and David L. Darmofal. *Anisotropic Grid Adaptation for Functional Outputs: Application to Two-Dimensional Viscous Flows*. *Journal of Computational Physics*, 187:22–46, 2003.
- [42] E. M. Lee-Rausch, M. A. Park, W. T. Jones, D. P. Hammond, and E. J. Nielsen. *Application of Parallel Adjoint-Based Error Estimation and Anisotropic Grid Adaptation for Three-Dimensional Aerospace Configurations*. In *23rd AIAA Applied Aerodynamics Conference*. AIAA 2005-4842, June 2005.
- [43] M. A. Park. *Three-Dimensional Turbulent RANS Adjoint-Based Error Correction*. 2003. AIAA-2003-3849.

- [44] E. J. Neilsen and W. L. Kleb. *Efficient Construction of Discrete Adjoint Operators on Unstructured Grids by Using Complex Variables*. 2005. AIAA-2005-0324.
- [45] David Maulick, Abraham Ortiz, Joshua Richards, Griffin Uthe, Alex West, and Charles O’Neill. *Martian Atmospheric Entry Maneuverability by Aeroshell Deformation and Payload Shift of Hypersonic Inflatable Aerodynamic Decelerators*. In *Region II Student Conference*, Huntsville, AL, April 2016. AIAA.
- [46] Edward Walker. *The Real Cost of a CPU Hour*. *Computer*, 42(4):35–41, April 2009.
- [47] *Sabalcore HPC On-Demand Pricing*. <http://www.sabalcore.com/services/pricing/>, 2015 (accessed January 10, 2016).
- [48] *Oran W. Nicks Low Speed Wind Tunnel Pricing, Terms, and Conditions*. <http://wind.tamu.edu/price.htm>, 2014 (accessed January 4, 2016).
- [49] *University of Washington Aeronautical Laboratory Rates for the Kirsten Wind Tunnel*. <http://www.uwal.org/customer/rateguide.htm>, 2015 (accessed January 4, 2016).
- [50] Aaron Hersch. *Wind Tunnel Killer?* [http://triathlon.competitor.com/2013/03/gear-tech/wind-tunnel-killer\\_71740](http://triathlon.competitor.com/2013/03/gear-tech/wind-tunnel-killer_71740), March 2015 (accessed June 07, 2016).
- [51] Gary B. Cosentino. *Computational Fluid Dynamics Analysis Success Stories of X-plane Design to Flight Test*. Technical Memorandum TM-2008-214636, NASA, May 2008.

**APPENDIX A**

**SAMPLE DATCOM HINGE MOMENT CALCULATIONS FOR THE  
GA(W)-1 AIRFOIL**

The GA(W)-1 reference quantities required for the Datcom calculations are given in Table 3.1.

Table A.1: GA(W)-1 reference quantities.

Property	Value
$t/c$	0.17
$c_f/c$	0.2
Re	$2.2 \times 10^6$
M	0.13

The trailing edge angle tangents are first calculated using the formulas

$$\tan\left(\frac{\Phi_{TE}}{2}\right) = \frac{\bar{y}_{99} - \bar{y}_{TE}}{0.01} \quad (\text{A.1})$$

$$\tan\left(\frac{\Phi'_{TE}}{2}\right) = \frac{\bar{y}_{90} - \bar{y}_{99}}{0.09} \quad (\text{A.2})$$

$$\tan\left(\frac{\Phi''_{TE}}{2}\right) = \frac{\bar{y}_{95} - \bar{y}_{99}}{0.04} \quad (\text{A.3})$$

where  $\bar{y}$  is the average y-coordinate at the location indicated by the subscript. The trailing edge coordinates required for the calculations are provided in Table A.2.

From figure 6.1.3.1-11b in the Datcom,  $(C_{h_\alpha})_{\text{theory}} = -0.35$  per radian. Interpolating figure 4.1.1.2-8a in the Datcom gives

$$\frac{C_{l_\alpha}}{(C_{l_\alpha})_{\text{theory}}} = 0.80411$$

Table A.2: GA(W)-1 trailing edge coordinates required for Datcom calculations

$x/c$	$y/c$	
	top	bottom
0.90	0.02639	-0.00352
0.95	0.01287	-0.00257
0.99	0.00197	-0.00628
1	-0.00074	-0.00783

Interpolation is done by plotting the ratio versus  $\log_{10}(\text{Re})$  using a linear interpolation scheme.

From figure 4.1.1.2-8b in the Datcom,  $(C_{l_\alpha})_{\text{theory}} = 7.15$  per radian.

Figure 6.1.3.1-11a in the Datcom gives

$$\frac{C_{h_\alpha}}{(C_{h_\alpha})_{\text{theory}}} = 0.41$$

From this, the first estimate of the hinge moment coefficient can be calculated as

$$C'_{h_\alpha} = (C_{h_\alpha})_{\text{theory}} \left( \frac{C_{h_\alpha}}{(C_{h_\alpha})_{\text{theory}}} \right) = -0.1435$$

To account for thickness distribution, a correction is made.

$$C''_{h_\alpha} = C'_{h_\alpha} + 2(C_{l_\alpha})_{\text{theory}} \left( 1 - \frac{C_{l_\alpha}}{(C_{l_\alpha})_{\text{theory}}} \right) \left( \tan \left( \frac{\Phi''_{TE}}{2} \right) - \frac{t}{c} \right) = -0.3680$$

No overhanging balance is present in the reference case, so no balance correction is required.

$C_{h_\alpha}$  is then corrected for Mach number using the Prandtl-Glauert correction.

$$C_{h_\alpha} = \frac{C''_{h_\alpha}}{\sqrt{1 - M^2}}$$

This gives a final  $C_{h_\alpha} = -0.3711$  per radian, or -0.006477 per degree.

A similar process is used to predict  $C_{h_\delta}$ . Figure 6.1.3.2-12a in the Datcom gives

$$\frac{C_{h_\delta}}{(C_{h_\delta})_{\text{theory}}} = 0.835$$

From figure 6.1.3.2-12b in the Datcom,  $(C_{h_\delta})_{\text{theory}} = -0.68$  per radian. Combined with the previously calculated ratio, this gives  $C'_{h_\delta} = -0.5678$  per radian.

From figure 6.1.1.1-39a in the Datcom,  $(C_{l_\delta})_{\text{theory}} = 3.75$  per radian.

Figure 6.1.1.1-39b gives

$$\frac{C_{l_\delta}}{(C_{l_\delta})_{\text{theory}}} = 0.66$$

Corrected for thickness distribution,

$$C''_{h_\delta} = C'_{h_\delta} + 2(C_{l_\delta})_{\text{theory}} \left(1 - \frac{C_{l_\delta}}{(C_{l_\delta})_{\text{theory}}}\right) \left(\tan\left(\frac{\Phi''_{TE}}{2}\right) - \frac{t}{c}\right) = -0.7721$$

Again, no overhanging balance is present, so no balance correction is needed.

The value is then corrected for Mach number using the Prandtl-Glauert correction as before.

$$C_{h_\delta} = \frac{C''_{h_\delta}}{\sqrt{1 - M^2}}$$

The final value for  $C_{h_\delta}$  is -0.7787 per radian, or -0.01359 per degree.

## APPENDIX B

### CALCULATING HINGE MOMENTS FROM FUN3D OUTPUT

FUN3D outputs forces and moments about a user-specified reference location for each boundary patch using a reference area and a reference length in the x- and y-directions. If multiple components exist, such as control surfaces, it is necessary to recompute the moments about a different location and using different reference lengths and areas. The following shows the calculations used to compute hinge moments about a point other than that specified in the FUN3D input.

The forces and moments on a complete geometry are typically nondimensionalized using the chord, span, and reference area of the entire wing. Moments are nondimensionalized by a coefficient of moment,

$$C_{m_i} = \frac{M_i}{q_\infty S L_i} \quad (\text{B.1})$$

where  $q_\infty$  is the freestream dynamic pressure,  $S$  is the reference area, and  $L_i$  is the reference length used for nondimensionalization in the  $i^{\text{th}}$  direction. The forces are similarly nondimensionalized:

$$C_i = \frac{F_i}{q_\infty S} \quad (\text{B.2})$$

Here,  $C_i$  represents the force coefficient in the  $i^{\text{th}}$  direction ( $C_x$ ,  $C_y$ , and  $C_z$ ). Equations B.1 and B.2 can be rearranged to:

$$\frac{M_i}{q_\infty} = C_{m_i} S L_i \quad (\text{B.3})$$

$$\frac{F_i}{q_\infty} = C_i S \quad (\text{B.4})$$

The dimensional quantities are used for the moment repositioning and rotation calculations. In practice, the dynamic pressure term is carried through the calculations with the forces and moments.

The dimensional force and moment vectors are assembled using the following:

$$\vec{\mathbf{M}} = \begin{bmatrix} M_x \\ M_y \\ M_z \end{bmatrix} \quad (\text{B.5})$$

$$\vec{\mathbf{F}} = \begin{bmatrix} F_x \\ F_y \\ F_z \end{bmatrix} \quad (\text{B.6})$$

If a resultant force vector  $\vec{\mathbf{F}}$  acts on an airfoil, and the moment about point A is  $\vec{\mathbf{M}}^A$ , then the moment about a point B is

$$\vec{\mathbf{M}}^B = \vec{\mathbf{M}}^A + \vec{\mathbf{F}} \times \vec{\mathbf{r}} \quad (\text{B.7})$$

where  $\vec{\mathbf{r}}$  is the position vector between points A and B. To find the hinge moment about an axis defined by the point B and the unit vector  $\hat{\mathbf{b}}$ , simply take a dot product:

$$H = \vec{\mathbf{M}}^B \cdot \hat{\mathbf{b}} \quad (\text{B.8})$$

The hinge moment is then simply the sum:

$$H = \sum_{i=1}^3 M_i^B b_i \quad (\text{B.9})$$

Finally, the hinge moment is nondimensionalized using the hinge moment coefficient:

$$C_h = \frac{H}{q_\infty S_f c_f} \quad (\text{B.10})$$

## APPENDIX C

### XFOIL\_HINGEMOMENT SOURCE CODE

This script wraps XFOIL to compute hinge moments. In the code below, lines 16-47 are the XFOIL commands that are automatically executed by the script at run-time. Line 15 is the system command call that begins executing XFOIL. The entire XFOIL call is part of the `call_xfoil()` function that begins on line 7.

Listing C.1: `xfoil_ch_sweeps`

```
1  #!/bin/bash
2
3  set -o nounset
4  set -o errexit
5
6  #####
7  call_xfoil () {
8      delta=$1
9      alpha=$2
10     npts=340
11     iter=1000
12     polarfile="polar.txt"
13     dumpfile="dump.txt"
14
15     xfoil > ${xfoiloutput} << EOF
16     load ${input_file}
17     gdes
18     flap
19     ${hinge_x}
20     ${hinge_y}
```

```
21  ${delta}
22  exec
23
24  ppar
25  n
26  ${npts}
27
28
29  oper
30  re ${re}
31  m ${mach}
32  visc
33  iter ${iter}
34  pacc
35
36
37  a
38  ${alpha}
39  pwrt
40  ${polarfile}
41  dump
42  ${dumpfile}
43  fnew ${hinge_x} ${hinge_y}
44  fmom
45
46  quit
47  EOF
48  }
49
50  printUsage() {
51      echo "Usage: $1" [options]
52      echo
53      echo "Valid options:"
```

```

54     echo "  -a      : specify alphas, separated by commas"
55     echo "  -d      : specify deltas, separated by commas"
56     echo "  -chf     : specify hinge moment output file"
57     echo "  -chall   : include non-converged hinge moments"
58     echo "  -clf     : specify lift output file"
59     echo "  -cdf     : specify drag output file"
60     echo "  -cdpf    : specify pressure drag output file"
61     echo "  -cmf     : specify moment output file"
62     echo "  -h|-help : print this help message"
63     echo "  -hxy     : specify hinge x and y locations"
64     echo "  -i       : specify input filename"
65     echo "  -m       : specify Mach number"
66     echo "  -o       : specify output file"
67     echo "  -re      : specify Reynolds number"
68 }
69 #####
70
71 output_file="/dev/stdout"
72 ch_file="ch.dat"
73 cl_file="cl.dat"
74 cd_file="cd.dat"
75 cdp_file="cdp.dat"
76 cm_file="cm.dat"
77
78 aflag=0
79 dflag=0
80 hflag=0
81 iflag=0
82 mflag=0
83 reflag=0
84 challflag=0
85
86 xfoiloutput="output_xfoil.txt"

```

```
87
88 while test $# -gt 0; do
89     case $1 in
90         -a) IFS=', ' read -a alphas <<< $2
91             aflag=1
92             shift
93             ;;
94         -chf) ch_file=$2
95             shift
96             ;;
97         -chall) challflag=1
98             ;;
99         -clf) cl_file=$2
100            shift
101            ;;
102        -cdf) cd_file=$2
103            shift
104            ;;
105        -cdpf) cdp_file=$2
106            shift
107            ;;
108        -cmf) cm_file=$2
109            shift
110            ;;
111        -d) IFS=', ' read -a deltas <<< $2
112            dflag=1
113            shift
114            ;;
115        -h) printUsage $0
116            exit
117            ;;
118        --help) printUsage $0
119            exit
```

```
120         ;;
121     -help) printUsage $0
122         exit
123         ;;
124     -hxy) hinge_x=$2
125         hinge_y=$3
126         hflag=1
127         shift
128         shift
129         ;;
130     -i) input_file=$2
131         iflag=1
132         shift
133         ;;
134     -m) mach=$2
135         mflag=1
136         shift
137         ;;
138     -o) output_file=$2
139         shift
140         ;;
141     -re) re=$2
142         reflag=1
143         shift
144         ;;
145     *) echo "unrecognized option"
146         printUsage $0
147         exit
148         ;;
149     esac
150     shift
151 done
152
```

```

153 if (( iflag == 0 )); then
154     read -p "Airfoil Input Filename: " input_file
155 fi
156 if (( aflag == 0 )); then
157     read -p "Enter alphas, separated by spaces: " -a alphas
158 fi
159 if (( dflag == 0 )) ; then
160     read -p "Enter deltas, separated by spaces: " -a deltas
161 fi
162 if (( hflag == 0 )); then
163     read -p "Hinge X location: " hinge_x
164     read -p "Hinge Y location: " hinge_y
165 fi
166 if (( mflag == 0 )); then
167     read -p "Mach Number: " mach
168 fi
169 if (( reflag == 0 )); then
170     read -p "Reynolds Number: " re
171 fi
172
173 echo "delta alpha CH CL CD CDp CM" > ${output_file}
174 echo "delta ${alphas[*]}" > ${ch_file}
175 echo "delta ${alphas[*]}" > ${cl_file}
176 echo "delta ${alphas[*]}" > ${cd_file}
177 echo "delta ${alphas[*]}" > ${cdp_file}
178 echo "delta ${alphas[*]}" > ${cm_file}
179 chs=()
180 cls=()
181 cds=()
182 cdps=()
183 cms=()
184 for delta in ${deltas[*]}; do
185     i=0

```

```

186   for alpha in ${alphas[*]}; do
187       call_xfoil ${delta} ${alpha}
188       CH="$(grep 'Hinge' ${xfoiloutput})"
189       CH=${CH%% x*}
190       CH=${CH###*= }
191       CH=$(echo "-1.0/(1.0-${hinge_x})/(1.0-${hinge_x}) * ${CH}" | bc)
192       read junk CL CD CDp CM junk <<< "$(tail -n 1 polar.txt)"
193       if [ "${CL}" == "-----" ]; then
194           if (( challflag == 0 )); then
195               CH="NaN"
196               fi
197               CL="NaN"
198               CD="NaN"
199               CDp="NaN"
200               CM="NaN"
201           fi
202           echo "${delta} ${alpha} ${CH} ${CL} ${CD} ${CDp} ${CM}" >> ${
                output_file}
203           chs[$i]=$CH
204           cls[$i]=$CL
205           cds[$i]=$CD
206           cdps[$i]=$CDp
207           cms[$i]=$CM
208           i=$(( i + 1 ))
209       done
210       echo "${delta} ${chs[*]}" >> ${ch_file}
211       echo "${delta} ${cls[*]}" >> ${cl_file}
212       echo "${delta} ${cds[*]}" >> ${cd_file}
213       echo "${delta} ${cdps[*]}" >> ${cdp_file}
214       echo "${delta} ${cms[*]}" >> ${cm_file}
215 done

```

## APPENDIX D

### XFOIL\_CH\_SWEEPS SOURCE CODE

This script wraps the `xfoil_hingement` script to perform an alpha and delta sweep.

Listing D.1: `xfoil_ch_sweeps`

```
1  #!/bin/bash
2
3  set -o nounset
4  set -o errexit
5
6  input_file="gaw1.points"
7  output_file="output_refined.txt"
8  hinge_x="0.8"
9  hinge_y="0.01852"
10 mach="0.13"
11 re="2.2e6"
12
13 alphas="-8,0,8,12,16,20"
14
15 delta_min=-40
16 delta_max=40
17 delta_step=5
18
19 deltas=""
20 delta=${delta_min}
21 while [ $(echo "$delta <= $delta_max" | bc) -eq 1 ]; do
22     deltas="$deltas,$delta"
23     delta=$(echo "$delta + $delta_step" | bc )
```

```
24 done
25 deltas=${deltas#,,}
26
27 ./xfoil_hingemoment \
28     -a ${alphas} \
29     -d ${deltas} \
30     -hxy ${hinge_x} ${hinge_y} \
31     -m ${mach} \
32     -re ${re} \
33     -i ${input_file} \
34     -o ${output_file}
```